Track and vertex reconstruction in the ATLAS inner detector

Track and vertex reconstruction in the ATLAS inner detector

ACADEMISCH PROEFSCHRIFT

ter verkrijging van de graad van doctor
aan de Universiteit van Amsterdam
op gezag van de Rector Magnificus
prof. dr. D.C. van den Boom
ten overstaan van een door het college voor promoties ingestelde
commissie, in het openbaar te verdedigen in de Agnietenkapel
op maandag 12 oktober 2009, te 14:00 uur

door

Maaike Limper

geboren te Eemnes

Promotor: prof. dr. S.C.M. Bentvelsen
Copromotor: dr. A.P. Colijn

Faculteit der Natuurwetenschappen, Wiskunde en Informatica

ISBN: 978-90-9024572-0

Cover by Maaike Limper

Contents

Introduction

As the inflatron rolls down the potential well,
all sorts of interesting things happen,
like life, love and the pursuit of happiness.

Leonard Susskind

What is the world around us made of? As early as 400 B.C., Greek philosophers proposed that matter is made of indivisible building blocks called *atomos*, meaning “indivisible” in Greek.

The search for the building blocks of matter remained a philosophical question until the first scientific studies in the 19th century posed the idea of different types of atoms, referred to as *elements*. These different types of atoms were found to be the building blocks of molecules and currently 118 different types atoms are described in the periodic table of elements. Atoms however are not indivisible building blocks but are composed of three main subatomic particles: the proton, neutron and electron.

The proton and neutron are located in the nucleus of the atom, forming the dense core of the atom. The proton has a positive charge, the electron a negative charge and the neutron is electrically neutral. Electrons surround the nucleus and are described to occupy regions referred to as electron shells, where each shell represents a distinct energy level. Electrons can be shared between the shells of two different atoms creating an *electron bond* that bind atoms together to form molecules.

The electron has, to our knowledge, no substructure and can thus be considered an elementary particle. The protons and neutrons, however, are not elementary particles but are composed of two types of quarks, the *up* and the *down* quark. During the 20th century the measurements of various particle physics experiments established the *Standard Model* of particle physics which describes all the known elementary particles as illustrated by figure 1. The electron is one of three types of leptons found in particle physics experiments, and similarly another two families of quarks have been observed.

Elementary particles can be grouped in two types: *fermions* (quarks and leptons), with a half-integer value of the quantum mechanical property called ‘spin’, and *bosons* with an integer value of spin. Fermions form the matter in

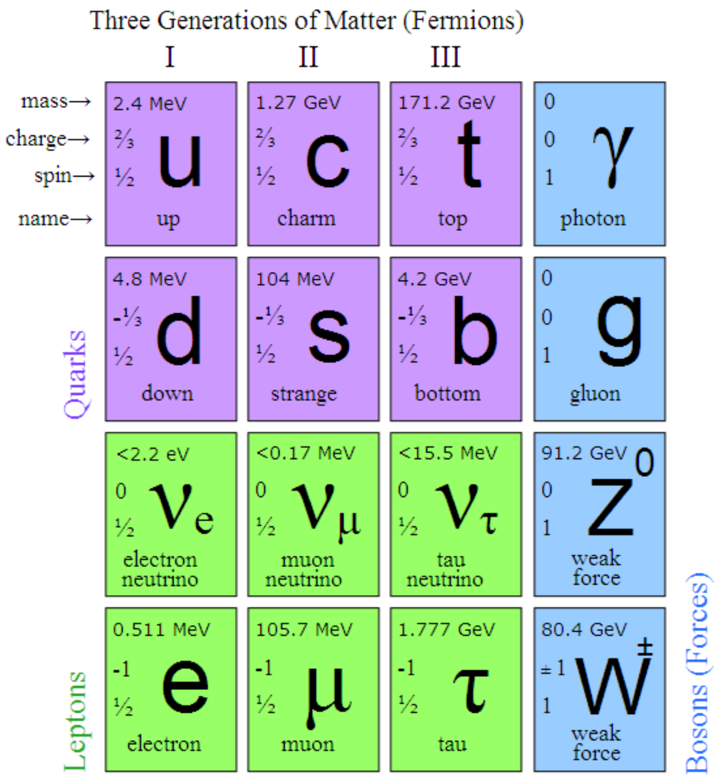

Figure 1: Elementary particles as described in Standard Model of particles physics. All fermions have a corresponding anti-particle, with opposite charge.

our world while bosons represent *force-carriers*. The electro-magnetic force is mediated by the exchange of photons, the strong force is mediated by gluons and the weak force (which causes radioactive β-decay of nuclei) is mediated by the $W^{\pm}$ and Z bosons. The gravitational force is not included in the Standard Model.

The $W^{\pm}$ and Z bosons are massive while the photon is massless; a result of the *breaking of the electro-weak symmetry*. The Standard Models postulates the existence of another gauge boson, the Higgs boson, which couples to the massive particles and describes the mechanism of symmetry breaking. In the Higgs mechanism, the masses of bosons and fermions emerge as the coupling of particles with the Higgs field.

The Higgs boson is the only particle of the Standard Model that has not yet been observed. The current experimental knowledge estimates the Higgs boson mass[1] to be within 114.4 and 185 GeV. The lower bound for this prediction is a result of direct searches for the Higgs boson at LEP [1], while the upper limit is set by the 95% confidence level from a fit to the measurements of the

[1] In this thesis 'natural units' are used; chosen to make $c,\hbar=1$, so that the mass of a particle is expressed in units of GeV.

electroweak observables

Identifying the mechanism of electroweak symmetry breaking will be one of the main goals of the Large Hadron Collider (LHC) at CERN. The LHC represents the next major step in the high-energy frontier of particle physics, with an unprecedented center of mass energy of 14 TeV and design luminosity of $10^{34}\mathrm{cm}^{-2}\mathrm{s}^{-1}$. The high design luminosity is required because of the small cross-sections expected for Higgs-boson production and decay and for possible physics processes beyond the standard model. The high center of mass energy of the LHC allows the discovery of particles with masses at the TeV scale.

The design of the ATLAS experiment at the LHC was guided by the need to provide sensitivity to a wide spectrum of possible physics signatures, including those of the Higgs boson. To exploit the full potential of the various sub-detectors in the ATLAS experiment the first LHC collision events will be used to calibrate and align the detector using well known physics processes. The ATLAS experiment uses silicon detectors with an intrinsic precision of $\approx$ 20 microns to reach the required precision of particles trajectories and decay vertices reconstructed with the detector. Uncertainty on the location of the silicon strip detectors after construction is of the order of hundreds of microns, requiring alignment of the detector using large sets of tracks.

This thesis focuses on the construction and commissioning of the forward silicon strip detector that was built at the Nikhef institute in Amsterdam, and the precise reconstruction of charged particle trajectories and vertices using measurements of the ATLAS inner detector. A tool for kinematically constraining a vertex-fit was developed which is demonstrated to help solve weak mode misalignments using $J/\psi \rightarrow \mu^+\mu^-$ as a benchmark channel.

The out-line of this thesis is as follows.
Chapter 1 of this thesis discusses the production of prompt J/ψ's in the LHC collisions which provide an important benchmark channel for calibration and alignment of the ATLAS detector. Chapter 2 gives a brief introduction of the LHC and the ATLAS experiment at CERN, discussing the various ATLAS sub-detectors. Chapter 3 discusses the requirements, lay-out and detector modules of the forward silicon strip detector, the Semi-Conductor Tracker (SCT) end-cap. Chapter 4 discusses the optical read-out system used by the silicon detector in ATLAS, focusing on the performance of the optical components of the SCT endcap. Chapter 5 discusses the various tests and results done of the functionality of the detector modules of the SCT endcap. Chapter 6 discusses the use of the measurements in the ATLAS inner detector to reconstruct precise trajectories and vertices from charged particles, focusing on a method for kinematically constraining a vertex fit. The last chapter discusses the alignment of the ATLAS inner detector, and investigates so-called 'weak mode' misalignments using mass constrained fit in $J/\psi \rightarrow \mu^+\mu^-$ events, to optimize the precision performance of ATLAS.

Chapter 1

J/ψ physics at LHC

The J/ψ particle represents a bound state of a charm and anti-charm quark pair. The J/ψ decay to two muons provides a striking signature for measuring the J/ψ in particle collider events. Understanding the details of prompt J/ψ production at 14 TeV proton-proton collisions is a challenging task and good testbed for various predictions of the theory of Quantum Chromo Dynamics. The J/ψ is among the decay products of heavier particle states (such as particles containing beauty quarks) and serves as a good signature for studying B-physics related processes. Another reason to study $J/\psi \rightarrow \mu^+\mu^-$ events, is that they can be used for alignment of the detector, as will be demonstrated later in this thesis.

This chapter provides some information on the current knowledge of the J/ψ particle properties and discusses the production of heavy quarks at proton-proton collisions. The expected cross-section for $J/\psi \rightarrow \mu^+\mu^-$ events at LHC within the phase-space reached by the ATLAS experiment is discussed.

1.1 The J/ψ particle

In 1974 about half of the number of elementary particles currently described in the Standard Model were not yet discovered and the basic constituents of nature were described by three quarks and four leptons. On November 10, 1974, two separate groups, one at BNL[1] studying collisions of accelerated protons on a beryllium target [2] and another at SLAC[2] studying electron positron collisions [3], simultaneously announced the discovery of a new particle with a mass at around 3095 MeV and a narrow width. BNL called the new particle J and SLAC named it ψ, so it became known in literature as the J/ψ particle. Figure 1.1 illustrates the simultaneous J/ψ discovery in the two experiments using plots from the original papers.

[1]Brookhaven National Laboratory, U.S.A.
[2]Stanford Linear Accelerator Center, U.S.A.

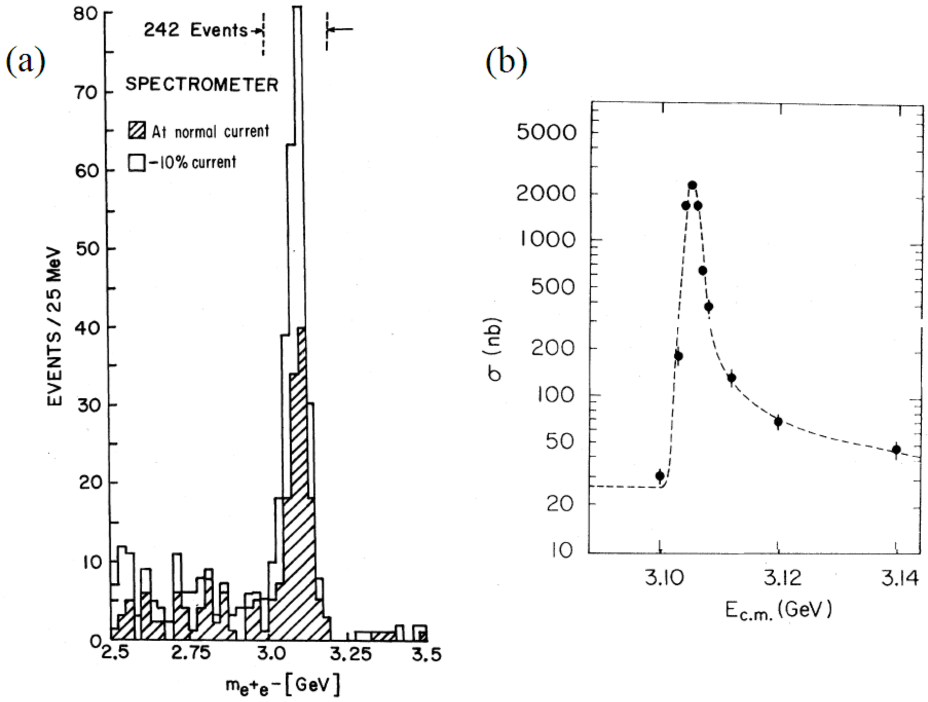

Figure 1.1: The discovery of the J/ψ: (a) The J discovery in e^+e^- final state at BNL [2] (b) The ψ discovery in multi-hadron final states at SLAC [3].

Soon after the J/ψ discovery the experiment at SLAC discovered another vector meson ψ' at 3695 MeV followed by the discovery through radiative transitions of three more states, whose masses were between those of the ψ' and J/ψ. Within about one year after its discovery it was clear that the J/ψ is the first excited state of the charmonium, the bound state of a charm and anti-charm quark pair, with the other states being other excited charmonium states. These discoveries confirmed the hypothesis of the existence of a fourth quark, the charm quark.

The charmonium appears in various resonance states with different quantum numbers[3]. The J/ψ and some of the other charmonium states are listed in table 1.1 together with the current knowledge of their mass and width. The lowest mass charmonium, η_c, is a spin-0 particle which can not directly couple to a photon (spin-1) and as consequence the η_c has no leptonic decay channels.

Figure 1.2 shows the Feynman diagrams for the main J/ψ decay modes. The J/ψ decays about 30% of the time electromagnetically resulting in the production of hadrons or charged leptons. The other 70% of the J/ψ decays proceed via the strong force resulting in various hadronic final states. In most particle decays the strong force would dominate the electromagnetic force, but

[3]Spectroscopic notation: $n^{2s+1}L_j$, where n is the principle quantum number, s is the spin, L the orbital quantum number and J the angular momentum.

Spectroscopic notation	Particle name	Mass (MeV)	Width (MeV)
1^1S_0	η_c	2980.3±1.2	17.3±2.6
1^3S_1	J/ψ	3096.916±0.011	0.0910±0.0032
1^1P_1	h_c	3525.93±0.27	<1.1
1^3P_0	χ_{c0}	3414.75±0.31	10.2±0.9
1^3P_1	χ_{c1}	3510.66±0.07	0.91±0.13
1^3P_2	χ_{c2}	3556.20±0.09	2.11±0.16
2^1S_0	η_c'	3637±4.	<55.
2^3S_1	ψ'	3686.09±0.04	0.281±0.017

Table 1.1: Charmonium states as listed by the Particle Data Group [4].

the strong J/ψ decay is supressed for several reasons. First, the J/ψ mass is less than the masses of the D-mesons that separately contain charm quarks, so the decay into D-mesons is not possible. Secondly, at least three gluons are required to conserve colour and spin[4].

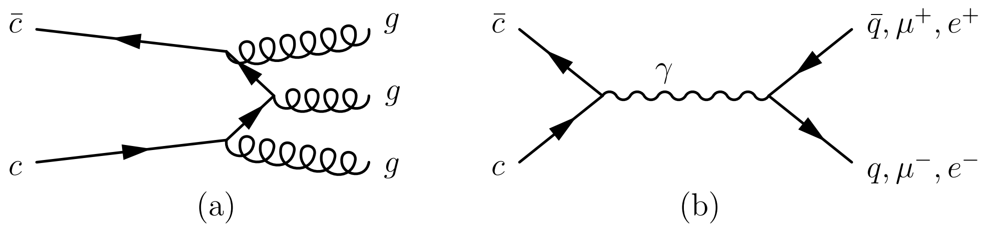

Figure 1.2: Feynman diagrams for J/ψ decay modes showing (a) strong-force mediated decay via three gluons and (b) electro-magnetic decay via a virtual photon.

The world average of the measured J/ψ decay fractions is summarized in table 1.2. The J/ψ's narrow resonance combined with its possible decay to a $\mu^+\mu^-$ pair create a striking signature to observe the J/ψ in any particle physics experiment.

[4]Decays of states such as η_c are mediated via two gluons, resulting in the much wider width of the η_c compared to the J/ψ.

J/ψ **decay fraction**	
Mode	Fractions
$J/\psi \rightarrow\rightarrow hadrons$	87.7±0.5%
$J/\psi \rightarrow e^+e^-$	5.94±0.06%
$J/\psi \rightarrow \mu^+\mu^-$	5.93±0.06%

Table 1.2: J/ψ decay fraction as listed by the Particle Data Group [4].

1.2 Prompt J/ψ production at proton-proton collisions

The J/ψ particle at LHC is produced by the interactions between the partons (quarks and gluons) inside the colliding protons. Quarks and gluons interact via the strong force as is described in the theory Quantum Chromo Dynamics (QCD). Predictions of cross-sections at LHC rely on the use of Monte Carlo event generators. All events in this thesis are simulated using the Pythia event generator [5].

1.2.1 Event generation

The collision of protons at high energy can be seen as a collision between the partons inside the proton. Due to the quantum field description of the strong interaction inside a proton, gluons are continuously exchanged and quarks and anti-quarks are continuously created and annihilated. As a result, the proton contains not only the three valence quarks (u,u,d) but also gluons and a 'sea' of quarks and anti-quarks.

The density of quarks and gluons inside the proton is described by the "parton distribution functions" (PDF). These PDFs $f(x)$ describe the probability to find a parton with flavor f with a momentum fraction x of the total proton momentum. PDFs are obtained by means of a global fit to experimental data, typically from experiments studying proton-electron collisions. The production cross section in a proton-proton collision can factorized as follows:

$$\sigma_{pp\rightarrow X} = \sum_{i,j} \int_0^1 \int_0^1 dx_1 dx_2 f_i(x_1) f_j(x_2) \hat{\sigma}_{i,j\rightarrow X} \tag{1.1}$$

where i, j denote the different partons in the proton and $\hat{\sigma}_{i,j\rightarrow X}$ represents the production cross-sections with the initial state partons i, j.

The hard parton scattering cross section $\hat{\sigma}_{i,j\rightarrow X}$ can be computed within the framework of perturbative QCD. Pythia implements calculations made at lowest order in the coupling constant in terms of transitions probabilities into various final states. Higher orders are approximated by a parton shower process in which the particles before and after the interaction radiate gluons and photons, or quark anti-quark pairs. This process continues until the parton energy reaches the hadronisation scale (at around 1 GeV) where the colored partons combine to form hadrons. Hadron formation in Pythia is based on the Lund string model [6], which is a phenomenological model within which the long-range confinement forces are allowed to distribute the energies and flavors of a parton configuration among a collection of primary hadrons, which subsequently may decay further.

1.2.2 Prediction of the J/ψ cross-section

At very high energies the strong coupling α_s becomes small, allowing accurate predictions using perturbative QCD [7]. The creation of a $c\bar{c}$ pair involves the interaction of quarks and gluons with relatively high momenta and can be calculated in perturbation theory. However, the subsequent transition from the $c\bar{c}$ pair to a J/ψ particle is a non-perturbative process that involves radiation of low momenta gluons and can not be calculated directly.

The framework of non-relativistic QCD [8] separates the perturbative and non-perturbative processes such that the J/ψ formation is factorized into universal non-perturbative parameters. This way a prediction for the cross-section for J/ψ production at LHC can be calculated from the following expression [9]:

$$\begin{aligned} d\sigma(pp \rightarrow J/\psi + X) &= \sum_{i,j} \int \int dx_1 dx_2 f_i(x_1) f_j(x_2) \\ &\quad \times \sum_n d\hat{\sigma}(i + j \rightarrow c\bar{c}[n] + X) \langle \mathcal{O}^{J/\psi}[n] \rangle \end{aligned} \quad (1.2)$$

where the term $\hat{\sigma}(i+j \rightarrow c\bar{c}[n]+X)$ is the cross section for producing a $c\bar{c}$ in a state n, described by perturbative QCD, and $\langle \mathcal{O}^{J/\psi}[n] \rangle$ are the corresponding non-perturbative elements that describe the probability for a state n to form a J/ψ particle. Gluon fusion processes give the highest contribution to the cross-section due to the large gluon densities of the high-momentum protons.

J/ψ production was originally described in the Color Singlet Model (CSM) [10] where the $c\bar{c}$ pair is assumed to be produced endowed with quantum numbers of the state it eventually involves into. The leading order process in the Color Singlet Model, $g + g \rightarrow c\bar{c}[1^3S_1]$, is illustrated in figure 1.3. The radiation of one gluon is necessary to conserve the spin in the process.

The first tests of the color-singlet model were performed by the CDF experiment [11] that studied proton-anti-proton collisions with a center of mass energy of 1.8 TeV. The resulting measured prompt J/ψ cross-section at CDF turned out to be an order of magnitude larger than the leading order color-singlet prediction.

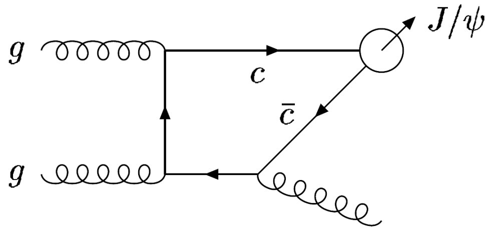

Figure 1.3: Feynman diagram of the leading order color-singlet subprocess for J/ψ production following gluon fusion of the initial state partons.

The Color Octet Model (COM) [12] attempts to provide a solution to this problem by assuming that heavy quark pairs produced in the hard process do not necessarily need to be produced with the quantum numbers of the J/ψ, but can evolve into the particular charmonium state through radiation of soft gluons and photons later on during hadronisation.

Figure 1.4 shows two examples of the Feynman diagrams for J/ψ production in hadron-hadron collisions of leading order color octet contributions[5]. Example (a) includes η_c production from ${}^3P_j$ color singlet states and ${}^1S_1$ and ${}^3P_j$ octet states that can produce J/ψ and χ_c particles through the radiation of soft gluons. The process in example (b) is predicted to produce almost only octet ${}^3S_1$ states and is unlikely to include any radiative χ_c decays.

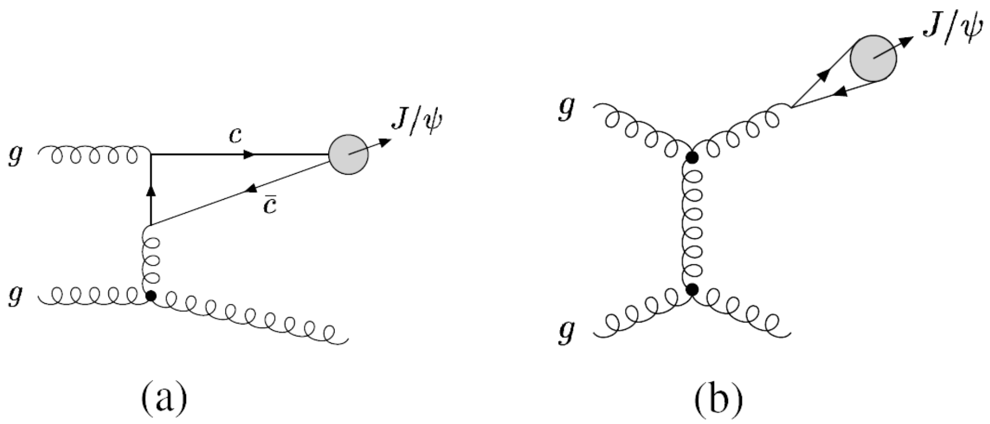

Figure 1.4: Examples of color-octet contributions to J/ψ production in proton-proton collisions: (a) t-channel contribution and (b) gluon fragmentation

The CDF results on J/ψ production are described by including the leading color-octet contributions, and adjusting the corresponding non-perturbative parameters to fit the data. This way the color-octet model provides a good

[5]The gray area in the Feynman diagrams in figure 1.4 represent the possible ways the $c\bar{c}$ state can produce a J/ψ.

description of the measured cross-section of the J/ψ at the CDF experiment as shown in figure 1.5.

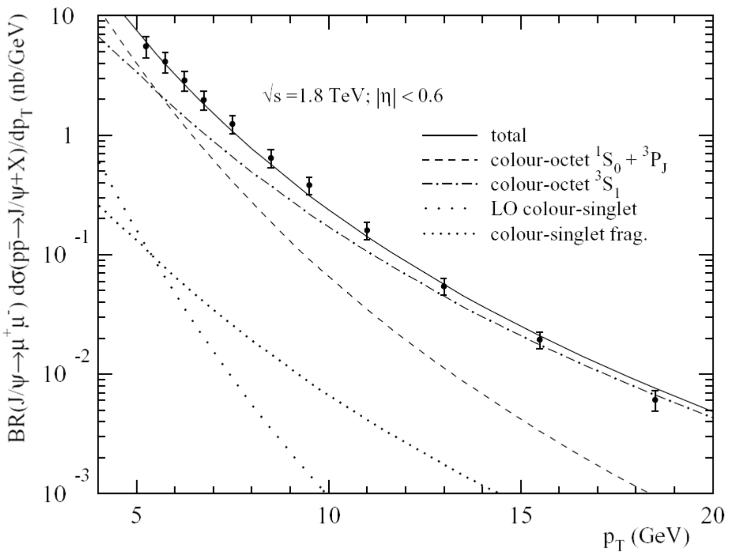

Figure 1.5: Differential cross-section of J/ψ production measured at CDF, with predictions from the color-singlet and color-octet mechanisms [9].

The analysis of the CDF data cross-section alone, although very encouraging, does not provide a conclusive test of NRQCD factorization because free parameters have to be introduced in the fit. However, if factorization holds, the non-perturbative matrix elements are universal and can be used to make predictions for various processes and observables. Measurements of the J/ψ production at LHC will provide more detailed checks of this model. The color-octet model currently provides the best description of J/ψ production at hadron-colliders and so it will be used to provide a benchmark for cross-section predictions at LHC. Given the substantial uncertainty in the determination of the non-perturbative matrix elements from present data, cross-section prediction made with the color-octet model should be regarded as order-of-magnitude estimates.

It should be noted that the CDF results in figure 1.5 represent the prompt J/ψ production after contributions from both B-decays and radiative χ_c decays have been removed[6]. For the studies done in this thesis we will consider 'prompt' J/ψ production to include the contributions of radiative χ_c decays. The production of J/ψ's through the decay of B-hadrons is considered separate from 'prompt' J/ψ production.

[6] χ_c states contribute to J/ψ production through $\chi_c \rightarrow J/\psi + \gamma$

1.2.3 Kinematics of $J/\psi \rightarrow \mu^+\mu^-$ events in ATLAS

To study the kinematics of J/ψ decays as they will be measured in ATLAS, generated $J/\psi \rightarrow \mu^+\mu^-$ events were produced with Pythia using the $CTEQ5L$ [13] parton distribution functions. Prediction of J/ψ production in Pythia incorporates the Color Octet Mechanism, with model parameters fixed through a combination of theoretical and experimental constraints [14]. Figure 1.6 shows the distribution of prompt $J/\psi \rightarrow \mu^+\mu^-$ events generated with Pythia as function of the J/ψ momentum, showing the contributions from the different production mechanisms.

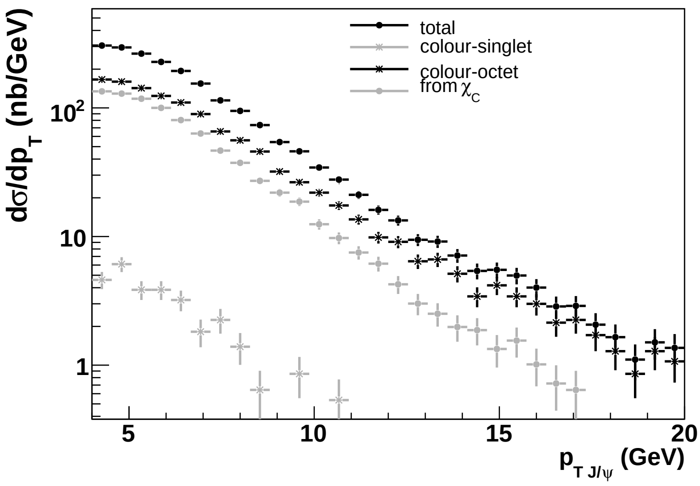

Figure 1.6: Distribution of prompt $J/\psi \rightarrow \mu^+\mu^-$ events generated with Pythia as function of the J/ψ momentum, showing the contributions from the different production mechanisms.

Figure 1.7 illustrates the transverse momentum and pseudo-rapidity distributions of the muons from prompt J/ψ decay. The two muons have an average transverse momentum of 2.8 GeV and are produced over a large range of pseudo-rapidity η. The distribution of the events over the phase-space of the muons is shown in figure 1.8. The transverse momentum and η of the muons are clearly correlated, which is the logical result of the invariant mass of the two muons being equal to the J/ψ value.

In general the ATLAS detector is unable to select and identify muons with a p_T less than 4 GeV which directly influences the range of the transverse momentum of the J/ψ that is accessible. In addition, the ATLAS experiment was designed to measure charged particle trajectories with a pseudo-rapidity η up to 2.5, which further limits the available phase-space for which $J/\psi \rightarrow \mu^+\mu^-$ events can be detected.

The J/ψ events that are recorded in ATLAS depend on the selection re-

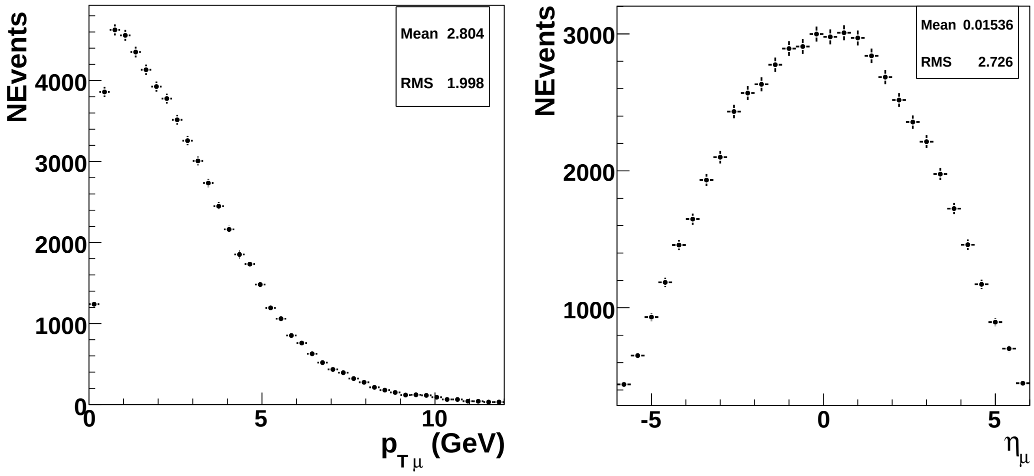

Figure 1.7: Distribution of $J/\psi \rightarrow \mu^+\mu^-$ events as a function of the transverse momenta (left) and the pseudo-rapidity η of the muons (right).

quirements. Figure 1.9 illustrates the p_T of the measured J/ψ's with various requirements on the p_T of the J/ψ's. It can be seen that the number of $J/\psi \rightarrow \mu^+\mu^-$ events that can be detected in ATLAS strongly depends on the minimum p_T requirements on the tracks.

The distribution of the opening angle of the two muons, described by the variable $\Delta R = \sqrt{\Delta\phi^2 + \Delta\eta^2}$, is shown in figure 1.10. It can be seen that requirements on the transverse momentum results in the reduction of the maxi-

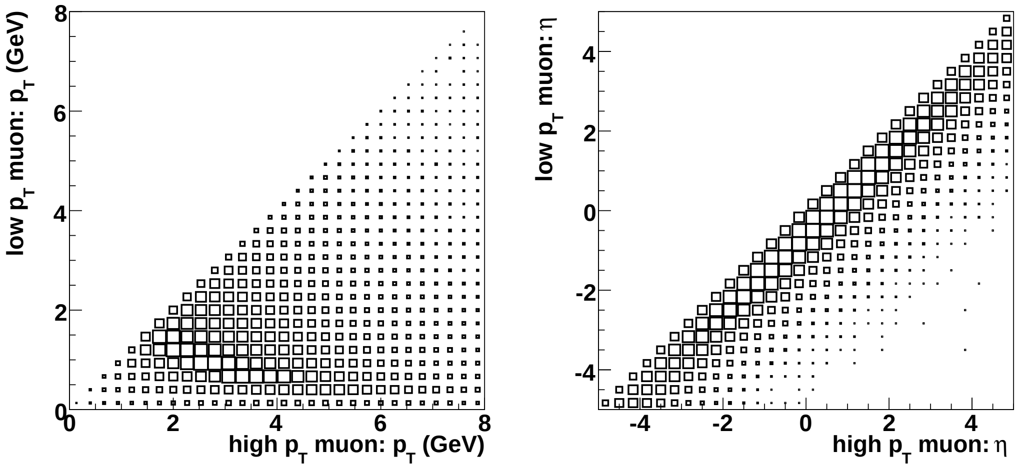

Figure 1.8: Distribution of $J/\psi \rightarrow \mu^+\mu^-$ events versus the transverse momenta (left) and versus the pseudo-rapidity η of the high and low p_T muon (right).

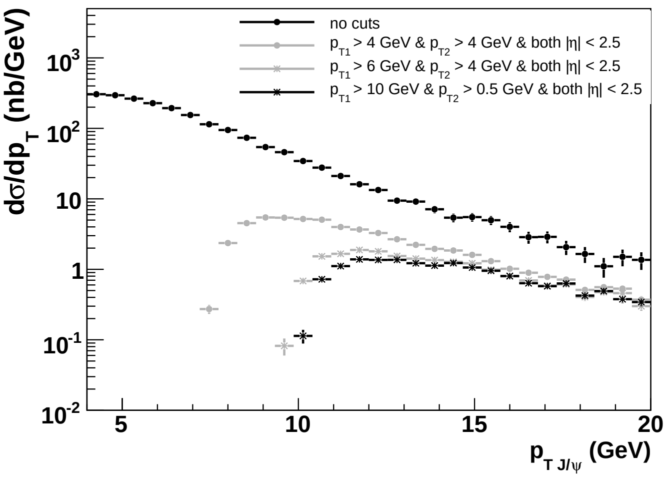

Figure 1.9: Distribution of $J/\psi \to \mu^+\mu^-$ events as function of the J/ψ momentum, with and without cuts on the transverse momentum p_T and pseudo-rapidity η.

mum opening angle between the two muons.

With cuts on the transverse momenta of the muons of 6 and 4 GeV and pseudo-rapidity cuts on both muons of $|\eta| < 2.5$, the predicted cross-section from Pythia of prompt $J/\psi \to \mu^+\mu^-$ events is 23 nb [15]. At the design luminosity of the LHC of $10^{-34}\text{cm}^{-2}\text{s}^{-1}$ this corresponds to a rate of 230 events per second.

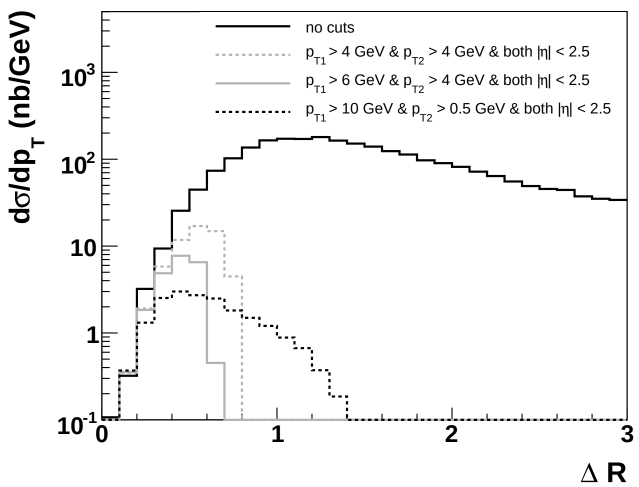

Figure 1.10: Distribution of ΔR separation of the two muons from J/ψ decay with and without cuts on the transverse momentum p_T and pseudo-rapidity η.

1.3 J/ψ production from B-decays

Production of $c\bar{c}$ pairs at the hard parton collision is not the only source of J/ψ production at LHC. The J/ψ is among the decay products of the particles containing bottom quarks and serve as an important signature for studying various B-physics processes. The perturbative QCD cross section for $b\bar{b}$ production can be calculated in a similar way as for $c\bar{c}$ production and the next-to-leading order prediction of the total $b\bar{b}$ cross section at $\sqrt{s}$=14 TeV proton-proton collisions is around 0.5 mb [14].

Produced b and $\bar{b}$ quarks hadronise forming B-hadrons as listed in table 1.3. B-hadrons are characterized by their relative long lifetimes, so that with a precise track detector it is possible to measure the decay-vertex of these particles as a separate vertex relative to the primary vertex of the proton-proton collision. A fraction of 1.2% of the B-hadron decays will produce a J/ψ. In the case where a J/ψ decaying to two muons was among the b-hadron decay products, the decay-vertex can be detected as the intersection point of two muon trajectories with an invariant mass equal to the J/ψ mass.

B-hadron	Mass (MeV)	Lifetime (ps)	Fraction
B^+ ($\bar{b}u$)	5279.0±0.5	1.638±0.011	39.9±1.1 %
B^0 ($\bar{b}d$)	5279.4±0.5	1.530±0.009	39.9±1.1 %
B^0_s ($\bar{b}s$)	5367.5±1.8	1.466±0.059	11.0±1.2 %
$B-baryon$ ($\bar{u}\bar{b}\bar{d}$) ($\Lambda_b, \Xi_b, \Sigma_b, \Omega_b$)	5624.±9.(Λ_b)	1.209±0.049	9.2±1.9 %

Table 1.3: *B-hadrons produced in the hadronisation of a $\bar{b}$-quark [4]. Identical numbers apply for the anti b-hadrons produced in the hadronisation of b-quark.*

The Pythia event generator was used to generate events of $pp \rightarrow b\bar{b} \rightarrow X + (J/\psi \rightarrow \mu^+\mu^-)$. The generator cuts were set such that the transverse momenta of the muons was required to be >6 GeV for one muon and > 4 GeV for the second muon with pseudo-rapidity cuts on both muons of $|\eta| < 2.5$.

The predicted cross-section from Pythia of $b\bar{b}$ pairs producing a $J/\psi \rightarrow \mu^+\mu^-$ with these requirements is 11.1 nb [16]. This means that in this selection region approximately 30% of the $J/\psi \rightarrow \mu^+\mu^-$ events are expected to originate from $b\bar{b}$ pair production.

Figure 1.11 shows the distance between the proton-proton interaction that produced the b-quarks and the position where the J/ψ-decay took place, in the plane perpendicular to the beam-axis. For prompt $J/\psi \rightarrow \mu^+\mu^-$ events this distance is equal to zero, so the measurement of the decay distance helps to differentiate between prompt J/ψ's and J/ψ's produced in B-hadron decays.

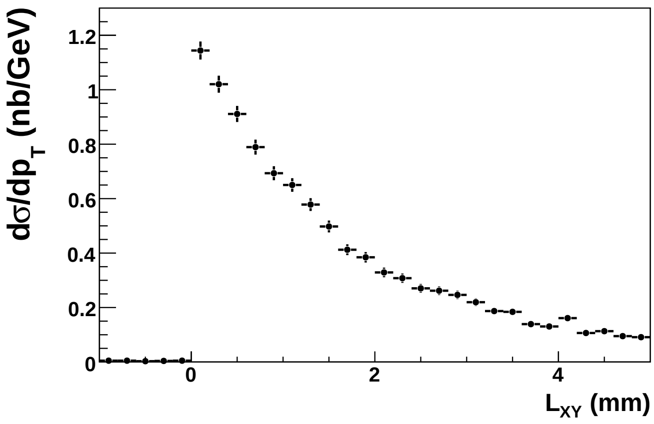

Figure 1.11: Transverse decay-length distribution of $b\bar{b} \to X + (J/\psi \to \mu^+\mu^-)$ events as predicted by Pythia using the generator cuts described in the text.

1.4 Other di-muon final states

Various other particles beside the *J/ψ* can result in di-muon final states . The ground state of bottonium Υ, the bound state of a b and an anti-b quark, can also decay to two muons, providing a similar striking signature as for the *J/ψ* but at a mass of 9.460±0.26 GeV.

Several other processes may lead to the production of two muons in one event in ATLAS, creating background events that have to be taken into account when studying di-muon decay signatures. The expected sources of background for di-muon events are [15]:

- Continuum of muon pairs from $b\bar{b}$ events
- Continuum of muon pairs from $c\bar{c}$ events
- Di-muon production via the Drell-Yan process [17]
- Decays in flight of $\pi^{\pm}$ and $K^{\pm}$ mesons

Figure 1.12 shows the contributions of the various di-muon backgrounds expected in the measurement of *J/ψ* and Υ in the ATLAS experiment [15].

For Drell-Yan muons or muons coming from $c\bar{c}$, the transverse momentum spectrum of the muon falls very steeply and the probability of producing an invariant mass within the trigger acceptance is well below the level from $b\bar{b}$ events. Muons from decays in flight also have a steeply falling muon momentum spectrum, and in addition require random coincidences with muons from other sources in the *J/ψ* invariant mass range. The most important background contributions for events with di-muon signatures is expected to come from

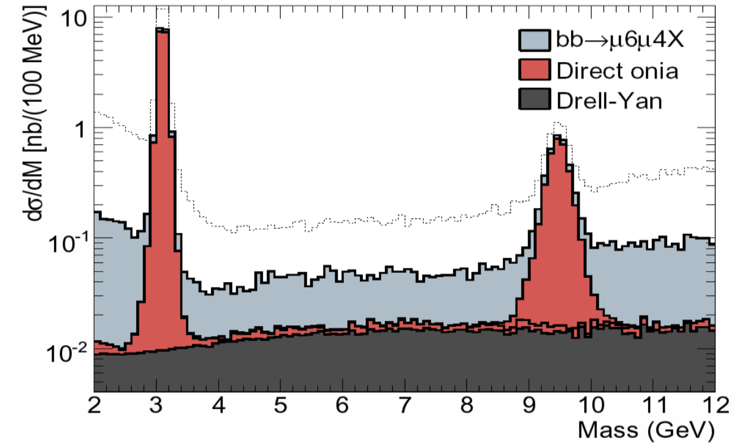

Figure 1.12: Invariant mass of di-muons from various sources as expected to be reconstructed in the ATLAS experiment when triggering on two muons with minimum p_T of 6 and 4 GeV, after optimization of cuts on the decay-time [15]. The dotted line shows the result without cuts on the decay-time.

muons from $b\bar{b}$ events, as these events can produce muons with relatively high transverse momentum.

The $b\bar{b}$ events are also the main background for another important process with a di-muon signature: $Z \rightarrow \mu^+\mu^-$. The decay of the Z-boson into two muons has a clear signature at an invariant mass of around 91 GeV, and a cross-section of ≈ 2 nb at LHC [15]. The expected invariant mass distribution for the measurement of $Z \rightarrow \mu^+\mu^-$ events in ATLAS is illustrated in figure 1.13.

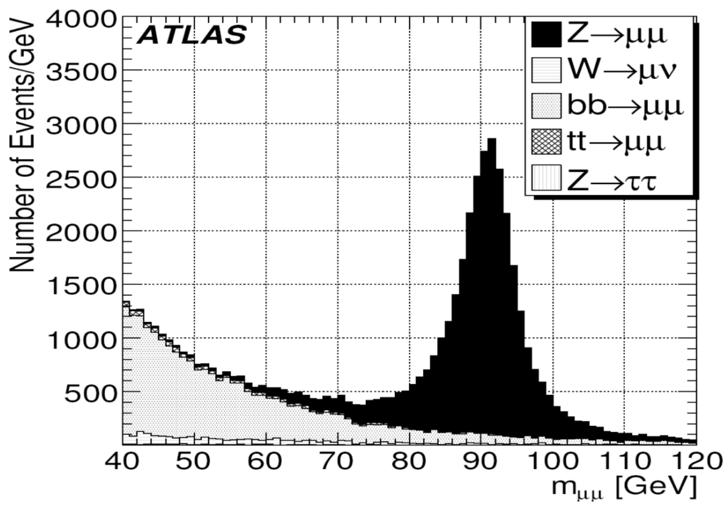

Figure 1.13: Di-muon invariant mass distribution in the $Z \rightarrow \mu\mu$ channel, for signal and background, as expected to be reconstructed in ATLAS, for 50 pb^{-1} [15].

Chapter 2

LHC and the ATLAS experiment

The Large Hadron Collider is a proton-proton collider designed to operate with a center of mass energy up to 14 TeV. ATLAS is one of four detectors designed to observe the proton-proton collisions. This chapter gives a brief description of the LHC followed by a description of the ATLAS experiment explaining the different detector systems, the magnetic field and the trigger system.

2.1 Large Hadron Collider

The Large Hadron Collider (LHC) [18] is a proton-proton collider built at the European center for high-energy physics (CERN). The LHC is a circular proton-proton (*pp*) collider with a circumference of 26.7 km designed to accelerate two counter-rotating proton beams to an energy of 7 TeV. The LHC design parameters are summarized in table 2.1.

Parameter	**Value**	**Unit**
LHC circumference	26.66	km
Beam energy	7	TeV
Dipole field	8.3	T
Protons per bunch	1.15×10^{11}	
Bunches per beam	2808	
Bunch crossing frequency	40	MHz
Nominal luminosity	1×10^{34}	$cm^{-2}s^{-1}$

Table 2.1: The design parameters of the LHC accelerator.

Figure 2.1 shows the geographical location of the LHC and the position of four experiments that have been built around the points where the beams collide. At the LHC design luminosity of $10^{34}\text{cm}^{-2}\text{s}^{-1}$, on average about 27 interactions will occur per bunch crossing, leaving the experiments to disentangle the pile-up of different hard interaction processes. A high luminosity is needed since many interesting processes at the LHC energy have very small cross sections of the order of 1 pb or less (1 pb=10^{-36}cm^2).

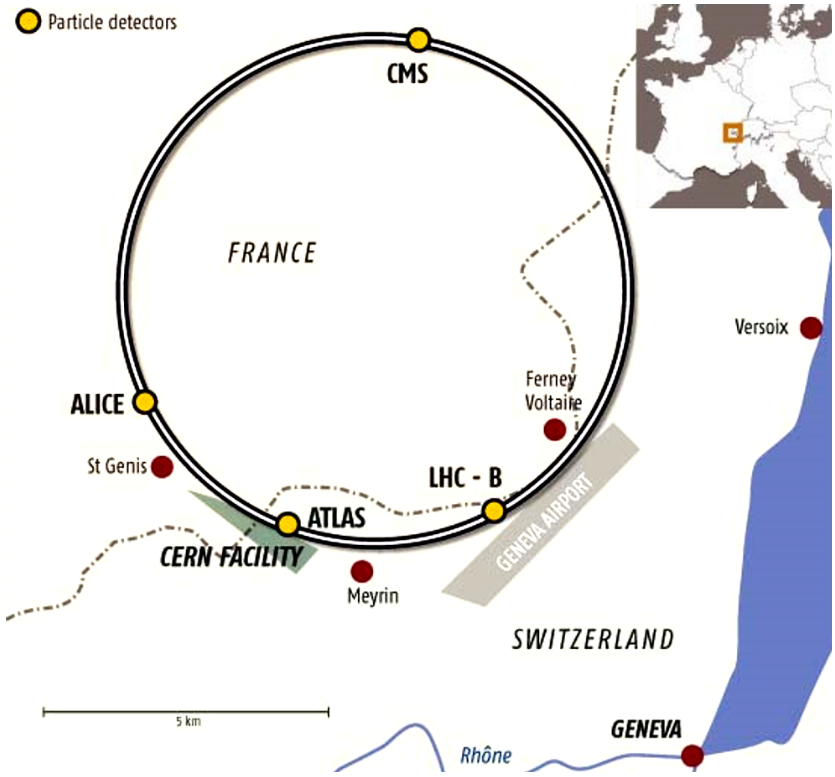

Figure 2.1: Geographical location of the 26.7 km long LHC tunnel indicating the four particle detector experiments placed along the accelerator ring.

On 10 September 2008, proton beams were successfully circulated in the LHC ring for the first time. On 19 September 2008, the operations were halted due to a serious fault between two superconducting bending magnets [19]. At the time of writing, the LHC is scheduled to be operational again in October 2009.

2.2 The ATLAS experiment

The ATLAS experiment [16] is a detector designed to exploit the full physics potential of LHC. The ATLAS detector has an approximate cylindrical symmetry, composed of a central *barrel* where the detection elements form cylindrical layers around the beam pipe, and two *endcaps* where the detector elements are organized in wheels. Figure 2.2 gives an overview of the ATLAS detector.

The main design criteria of the ATLAS detector are:

- Very good electromagnetic calorimetry for electron and photon identification and measurement, complemented by full-coverage hadronic calorimetry for accurate jet and missing transverse energy measurements;
- High-precision muon momentum measurements, with the capability to guarantee accurate measurements at the highest luminosity using the external muon spectrometer alone;
- Efficient tracking at high-luminosity for momentum measurement of high p_T leptons, electron and photon identification, τ-lepton and heavy-flavor identification;
- Large acceptance in pseudo-rapidity with almost full azimuthal angle coverage everywhere;
- Triggering and measurements of particles at low-p_T thresholds, providing high efficiencies for most physics processes at LHC.

2.2.1 The ATLAS coordinate system

The origin of the coordinate system is defined as the center of the ATLAS detector, which coincides with the nominal interaction point. The z-axis is oriented parallel to the beam line in anti-clockwise direction, the x-axis is pointing in the direction of the center of the LHC ring and the y-axis is perpendicular to the x-axis and z-axis and points upwards.

The symmetry of the detector makes cylindrical coordinates useful. The azimuthal angle ϕ is the angle in the XY-plane originating from the x-axis and it increases clockwise when looking down the positive z-direction. The polar angle θ is defined as the angle with the positive z-axis. Instead of polar angle θ, the pseudo-rapidity $\eta = -\log \tan \theta/2$ is often used, as the particle multiplicity is approximately constant as function of η.

2.2.2 Inner Detector

The lay-out of the ATLAS inner detector is illustrated in figure 2.3. The inner detector consists of three sub-detectors: the pixel detector, the Semi-Conductor Tracker (SCT) and the Transition Radiation Tracker (TRT). The acceptance of the inner detector is limited to $|\eta| < 2.5$ due the increasing amount of radiation damage induced in the detector at higher values of $|\eta|$.

Since the inner detector uses a solenoid magnet, in which charged particles are mostly deflected in the XY-plane, the inner detector is designed to have the

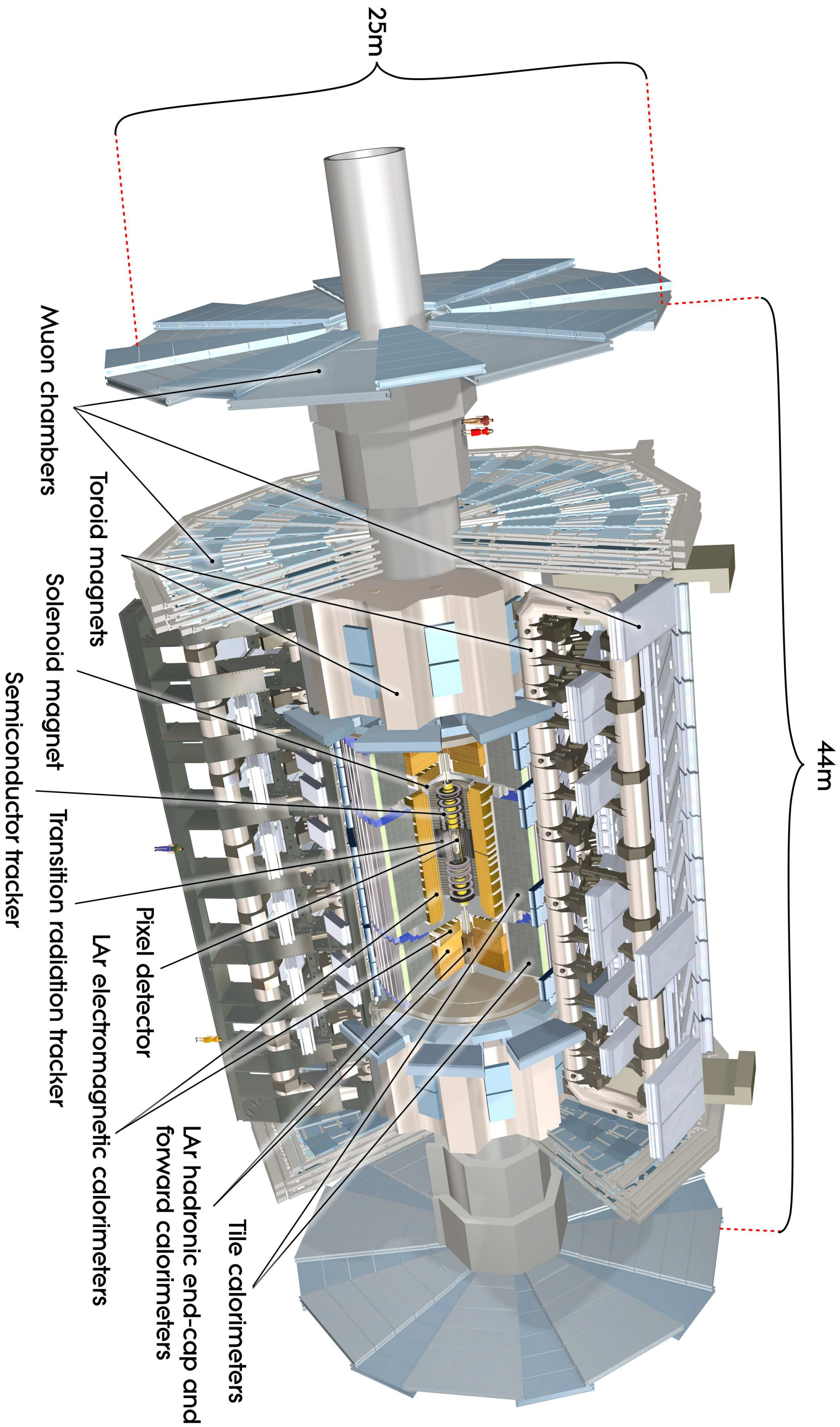

Figure 2.2: Cut-away view of the ATLAS detector with indications to its various subsystems.

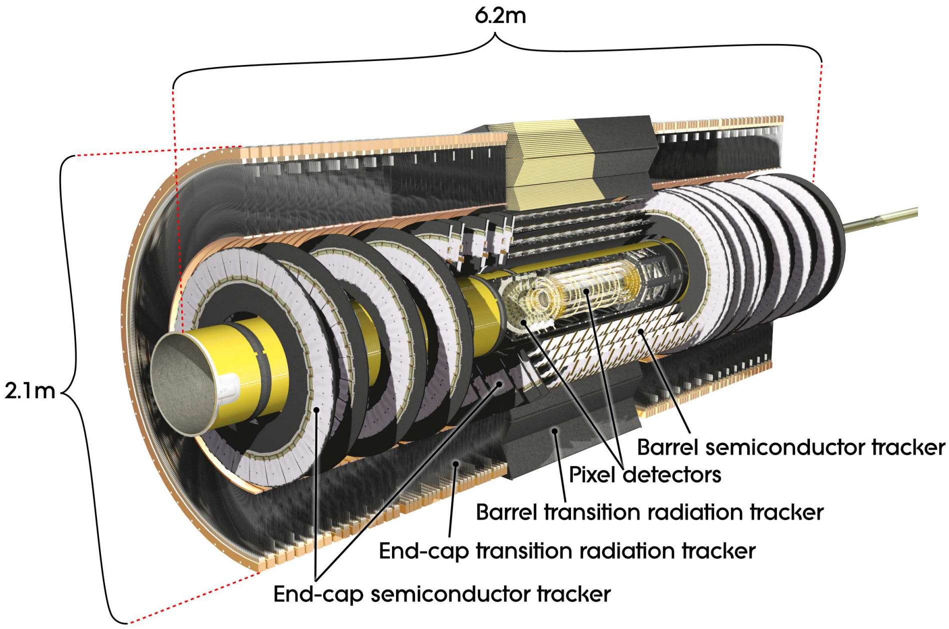

Figure 2.3: Cut-away view of the ATLAS inner detector.

highest precision in the transverse plane. The momentum resolution typically achieved with the inner detector is $\Delta p_T/p_T = 0.04\% \times p_T \oplus 2\%$ (p_T in GeV) and the impact parameter resolution is 15 μm in the transverse plane. The detector requires excellent tracking software and a precise knowledge of the detector positions in the order of a few μm to achieve the required resolution. To prevent a decrease in efficiency due to energy loss of the tracks in the detector, the total detector material had to be as low as possible while maintaining sufficient rigidity. The inner detector design is such that a particle originating from the interaction point crosses at least three pixel layers, four SCT strip layers and typically 30 TRT straws, giving on average 37 measurements in total to reconstruct the trajectory of a charged particle.

The solenoid magnet

The inner detector is housed in a superconducting solenoid magnet that generates a field of around 2 Tesla. The magnet has a diameter of 2.5 meters and is 5.3 meters long. It is shorter than the inner detector itself, which makes the field inhomogeneous in the forward region. Figure 2.4 shows the z- and R-components of the magnetic field (B_z and B_R) as a function of z and R. The z-component of the field drops from 2 T to 1 T, while the R-component reaches up to 0.6 T in the forward region. The inhomogeneity of the magnetic field in the end-caps enforces the use of a field map based on measurements of the field at various positions in the inner detector.

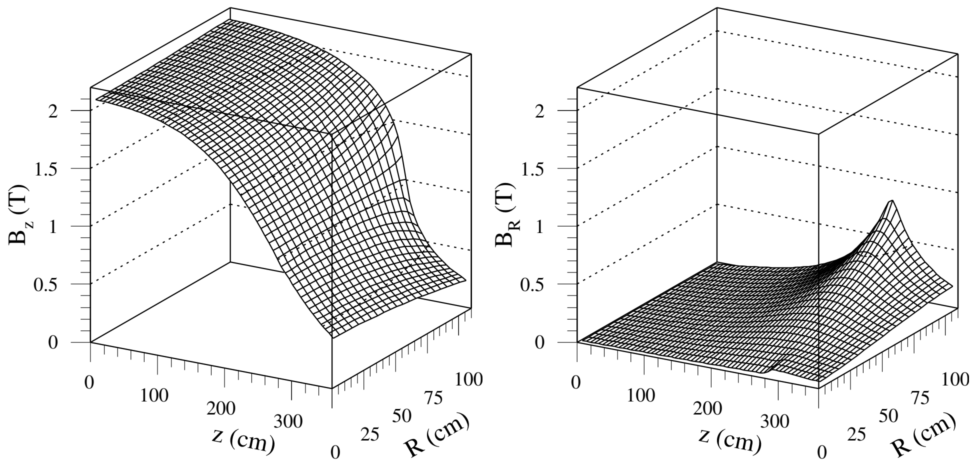

Figure 2.4: z-and R-components of the magnetic field in the solenoid, as a function of the position in the magnetic field.

The pixel detector

The pixel detector is closest to the interaction point, where the particle density is highest and therefore a highly granular detector is required. The pixel detector is made up of three cylindrical layers in the barrel, and three disks in each of the forward regions. The distances of the three barrel layers to the beam-line are 5.05, 8.85 and 12.25 cm respectively. The layers and disks are equipped with silicon sensors that are segmented into small rectangles, the *pixels*. The size of most pixels is $50\times400\,\mu\text{m}^2$ and a total of 80 million pixels are used. The pixel detector uses a charge depleted layer of silicon to measure the charge deposition caused by the ionization of a charged particle transversing the pixel. The principle of detecting charged particles using silicon detectors will be explained in detail in section 3.2. The pixel detector records the *time-over-threshold* of the signal, which gives a measure of the amount of charge deposited in a single pixel. The charge distribution over adjacent pixels determines the hit position. The pixel modules have a resolution of 12 μm in the R-ϕ coordinate, and 110 μm in the z coordinate.

The Semi-Conductor Tracker

The SCT is situated around the pixel detector. Here the particle density is low enough to use silicon strips, instead of pixels, to help reduce the number of readout-channels. The SCT detector modules are equipped with two silicon strip layers with a strip pitch of 80 μm. A small stereo angle between the strips in different layers is used to obtain a position measurement along the strip length. The barrel part of the SCT consists of four layers of detector modules at $|\eta|$ <1.4, while the SCT end-caps are each composed of nine disks equipped with detector modules in the region 1.4< $|\eta|$ <2.5. A detailed explanation of the SCT end-cap and the design of the SCT modules is given in chapter 3. Unlike the pixel modules, the readout of the SCT modules is binary, i.e. it registers only if a strip was hit or not, limiting the single strip resolution of the SCT to about 23 μm.

The Transition Radiation Tracker

The TRT is situated around the SCT and was designed to provide a relatively large number of measurements ($\sim$30). The TRT is composed of straws with a diameter of 4 mm that have a wire in the center and are filled with a gas mixture containing Xenon. The gas becomes ionized by the passage of a charged particle and the time that is takes the charge clusters to drift to the wire is measured. This drift time is converted into the distance at which the track passed from the wire, the drift radius. The resolution on the measured TRT drift radii is about 170 μm. In the barrel the TRT straws are oriented parallel, while in the end-cap the TRT straws are pointing to the beam axis. The space between the straws is filled up by a radiator material where transition radiation photons (X-rays) are produced when an electron crosses the boundary between two media. X-rays can be absorbed by the TRT gas, leading to the production of a large amount of charge. The TRT read-out discriminates against two thresholds, a low one for ionization and high one for X-ray absorption, thus making electron identification with the TRT possible. For energies larger than 1 GeV, the TRT has an electron identification efficiency of 90%.

Material budget

Particles that traverse the inner detector will interact with the material (sensors, cables, support structures etc.) causing them to lose energy and deviate from their trajectory. Since the inner detector is required to make precise reconstruction of the trajectories of particles as they are produced at the interaction point, material in the inner detector had to be minimized. Figure 2.5 shows the amount of material expressed in number of radiation lengths[1] as function of $|\eta|$ contributed by the different sub-detectors and the various services required to operate the detector. A more detailed discussion of the material budget of the forward SCT detector is given in chapter 3.

2.2.3 Calorimeter

The ATLAS calorimeter system consists of an electromagnetic calorimeter to measure and identify electrons and photons, and a hadronic calorimeter to

[1] One radiation length X_0 is defined as the distance over which a high-energy electron on average loses all but $1/e$ of its energy by Bremsstrahlung.

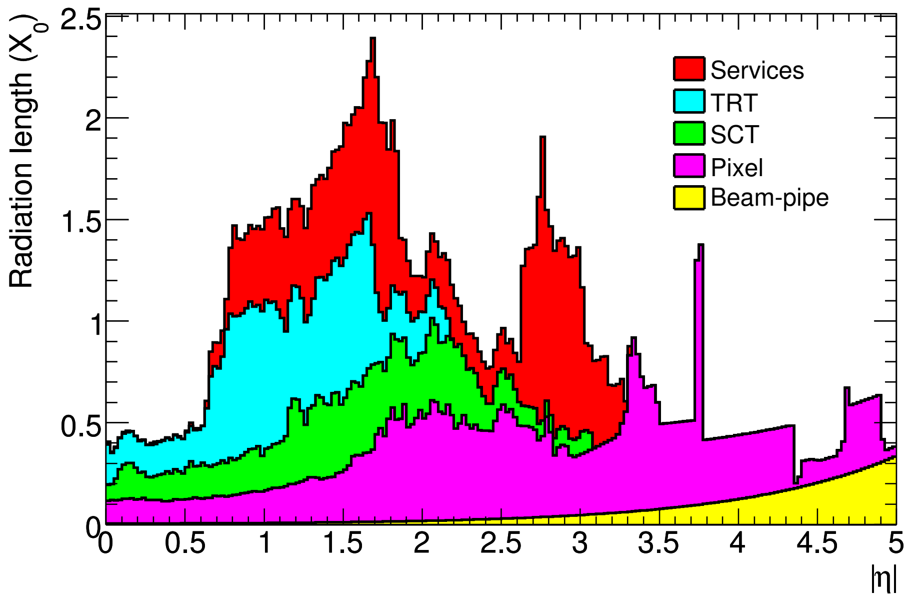

Figure 2.5: Material in the inner detectors in term of radiation length X_0 (averaged over ϕ) as function of $|\eta|$ [16].

measure the energy of both charged and neutral hadrons. The very forward region is covered by a radiation hard calorimeter with a courser granularity. This high η-coverage helps to improve the detection of missing transverse energy in the event, which is an important signature of the production of high energy neutrinos or possibly super-symmetric particles. The lay-out of the ATLAS calorimeter system is illustrated in figure 2.6.

The electromagnetic calorimeter

The electromagnetic calorimeter is a sampling calorimeter that uses lead as absorber material and liquid argon as sampling material. The absorber plates are placed in an accordion geometry providing complete ϕ-coverage without azimuthal cracks. The most inner section has a fine granularity in the η-direction, which enhances the γ/π_0 and e/π separation and also provides a precision η-measurement.

The electromagnetic calorimeter is composed of a barrel and two end-caps to cover the rapidity range up to $|\eta| < 3.2$. The total thickness of the electromagnetic calorimeter is more than 24 radiation lengths in the barrel and more than 26 radiation lengths in the end-caps. The liquid-argon electromagnetic calorimeter has an energy resolution of $\Delta E/E = 11.5\%/\sqrt{E} \oplus 0.5\%$, and a resolution of the polar direction of a particle shower of $\Delta\theta = 50$ mrad$/\sqrt{E}$ (E in GeV).

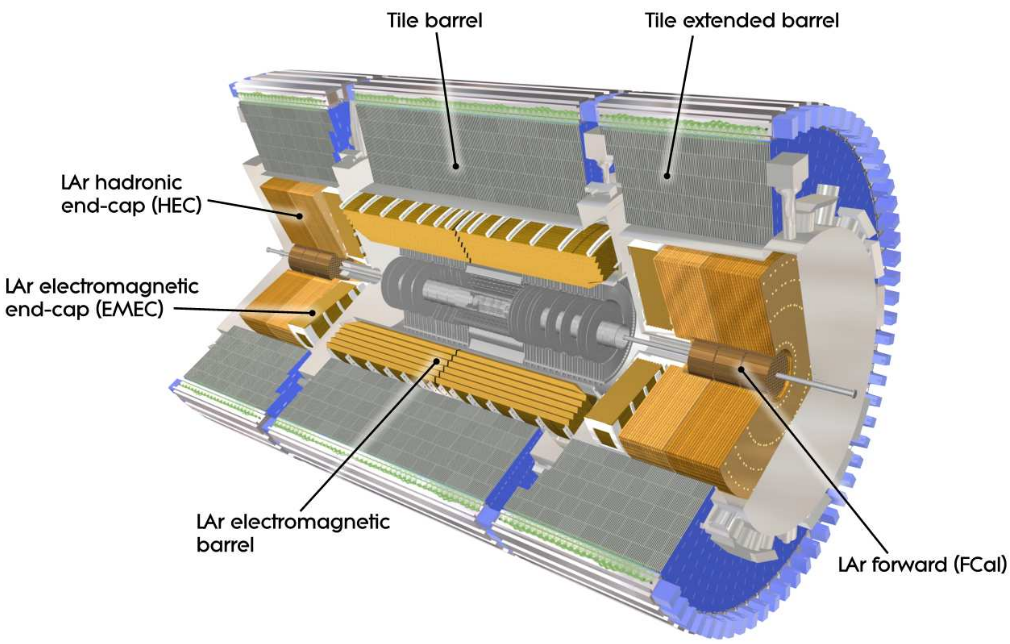

Figure 2.6: Illustration of the ATLAS calorimeters surrounding the inner detector.

The hadronic calorimeter

The hadronic calorimeter surrounds the electromagnetic calorimeter. The barrel hadronic calorimeter, $|\eta|$ <1.6, uses iron absorber tiles interleaved with scintillators to measure the passage of charged particles from the induced fluorescence light. The tiles are placed perpendicular to the colliding beams and are staggered in depth. The average jet energy resolution is $\Delta E/E = 50\%/\sqrt{E} \oplus 3\%$ (E in GeV), with a segmentation of $\Delta\eta \times \Delta\phi = 0.1 \times 0.1$.

The end-cap hadronic calorimeter receives a much higher radiation-dose than the barrel and therefore uses the intrinsically radiation-hard liquid argon technology. The hadronic end-cap uses copper absorbers in a parallel-plate geometry.

The thickness of the hadronic calorimeters is more than 10λ, where λ is the hadron interaction length (the mean free path of a hadron between two interactions). This thickness is sufficient to reduce the number of punch-through hadrons to be smaller than the number of muons produced in the proton collisions.

The forward calorimeter

The forward calorimeter uses liquid argon technology with copper and tungsten as absorber materials to cover the region, $3.1 < |\eta|$ <4.9, where radiation levels are especially high. The forward calorimeter is split longitudinally into an electromagnetic compartment, and two hadronic compartments. To avoid that neutrons are backscattered into inner detector volume, the forward calorimeter is placed 1.2 meter further away from the interaction point, compared to the electromagnetic end-cap calorimeter.

2.2.4 Muon Spectrometer

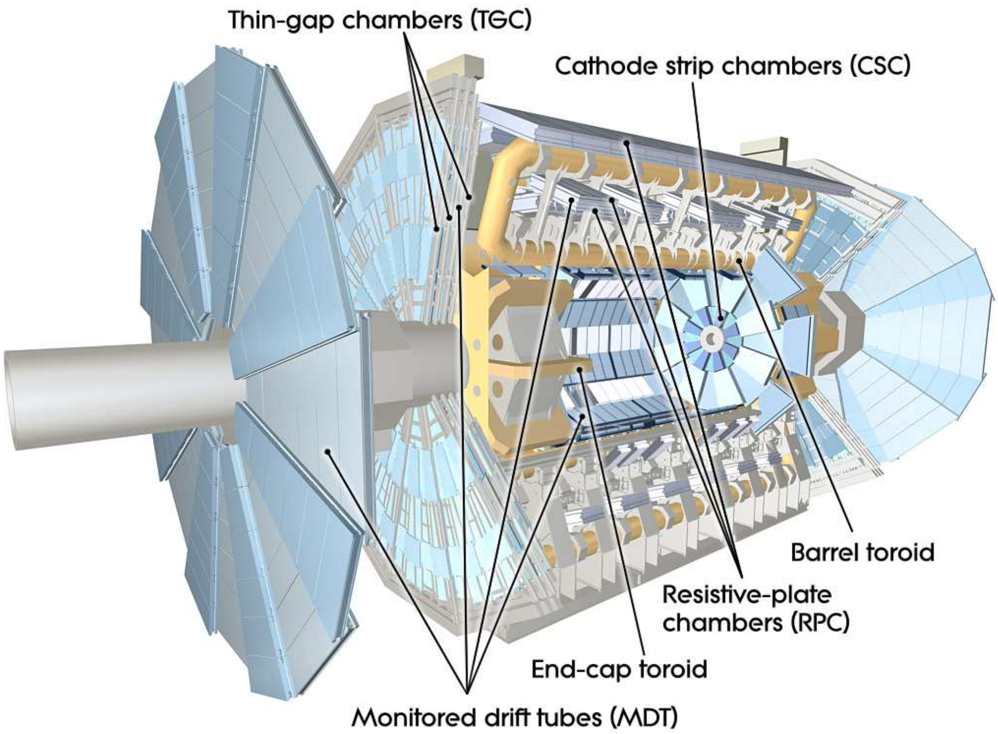

Figure 2.7: Illustration of the ATLAS muon spectrometer. The entire system is approximately 44 meters long and 22 meters high.

The muon spectrometer (see figure 2.7) covers the outer most layers of the ATLAS detector. The large lever arm over which the sagitta of the tracks can be measured makes the muon spectrometer especially suited for measuring muons with high momenta of $\mathcal{O}(100$ GeV). High-p_T muons are a signature of many interesting physics events, therefore the muon trigger and reconstruction is very important. The driving performance goal is a stand-alone transverse momentum resolution of approximately 10% for 1 TeV tracks, which translates into a sagitta along the z-axis of about 500 μm, to be measured with a resolution of $\approx 50\ \mu m$. Muon momenta down to a few GeV (≈ 4 GeV, due to energy loss in the calorimeters) may be measured by the spectrometer alone. Figure 2.8 shows the expected p_T resolution of track reconstruction in the muon spectrometer and in the inner detector as a function of p_T as obtained using simulated muon events in ATLAS. It can be seen that for muons with p_T >40 GeV the momentum resolution obtained with the muon spectrometer is better than the resolution obtained by the inner detector. For lower p_T muons the inner detector measurements will determine the momentum resolution, but measurements from the muon spectrometer are still required to identify the inner detector tracks as muons.

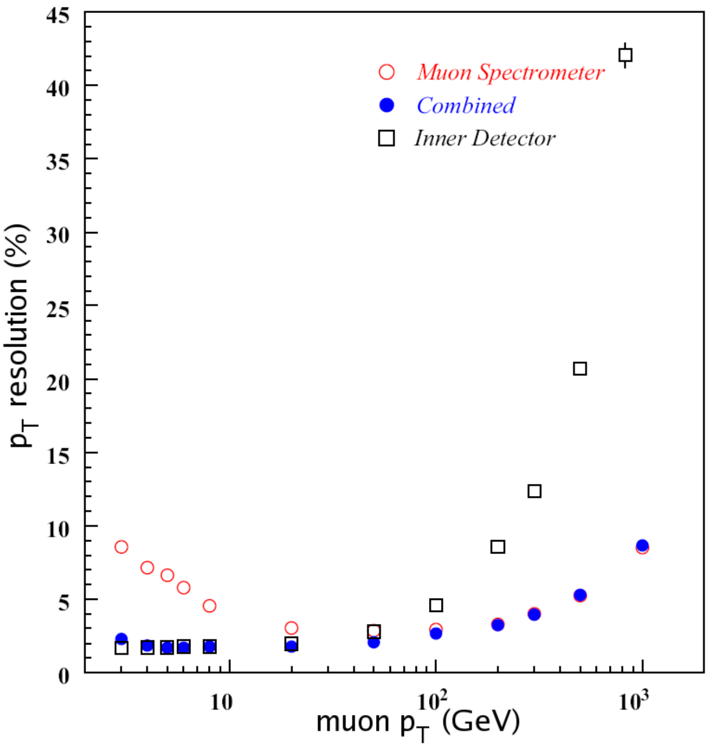

Figure 2.8: p_T resolution of track reconstruction in the muon spectrometer and in the inner detector as a function of p_T as obtained using simulated muon events in ATLAS [20].

The magnet system in the muon spectrometer of ATLAS provides an approximately toroidal field and is completely independent from the inner detector. The magnet system has an average field strength of 0.5 T, and a bending power that varies from 3 Tm in the barrel to more than 6 Tm in the end-caps. During ATLAS running a large number of Hall sensors will measure the local field ensuring a knowledge of the bending power with a precision better than 0.3%.

The muon system uses Monitored Drift Tube (MDT) chambers and Cathode Strip Chambers (CSCs) to make precision measurement in η (to measure the bending in the toroidal field). For triggering purposes, fast (but lower resolution) η-measurements are provided by the Thin Gap Chambers (TGCs) and Resistive Plate Chambers (RPCs). The TGCs and RPCs also provide a second coordinate measurement.

The MDT chambers

The MDT chambers consist of aluminum tubes of 30 mm diameter and a central wire. A muon that crosses a tube frees electrons by ionization, which will drift to the wire. The distance between the muon track and the wire is determined by measuring the drift time of the first cluster that reaches the wire. The resolution on the drift distance is around 80 μm. MDT chambers are used both in the barrel and end-caps of the muon system. In the barrel region, 0.$<|\eta|<$1.05, MDT chambers are situated in three layers at radii of 5, 7.5 and 10 m from the beam axis. In the end-cap region the chambers are divided over three wheels located a Z-positions of 7.5, 13 and $\sim$20 m. The MDT endcap wheels cover the region 1.05$<|\eta|<$2.7, except in the innermost layer, where the MDT chambers are only used up to $|\eta|<$2.0.

The Cathode Strip Chambers

The CSCs are used in the inner-most endcap ring, closest to the beam-pipe, in the region $2<|\eta|<2.7$. They have a high spatial resolution and a very small electron drift time of less than 30 ns (compared to the MDT drift time of up to 700 ns) which allows them to operate in the high background of the forward region. The CSC chambers are multi-wire proportional chambers with a cathode strip readout. The precision coordinate is determined from the charge distribution measured on the cathode strips. The second coordinate is read out using strips which are parallel to the anode wires (orthogonal to the cathode strips). The spatial resolution on the precision coordinate is around 60 μm and for the second coordinate the resolution is around 5 mm.

The Resistive Plate Chambers

RPC detectors are placed in every MDT barrel layer. The basic detector unit employs a thin gap formed by two plates filled with a gas mixture in which ionization charge is produced by the passage of a charged particle. The chambers are operated with a electric field so that the ionization charge is collected at the plates. The plates are covered with two orthogonal read-out strips. The η strips are parallel to the MDT wires (and help provide a fast p_T estimate used in the trigger) and the ϕ strips are orthogonal to the MDT wires and provide a position measurement along the MDT wire. The spatial resolution of the RPC is around 10 mm for both strips.

The thin-gap chambers

The TGCs provide the trigger signal and second coordinate measurement in the end-cap region. The TGCs are designed in a way similar to multi-wire proportional chambers, using an array of wire anodes and cathode strips. The thin gap in combination with the gas choice guarantees a short drift time (typically less than 25 ns). Signals from the anode wires, arranged parallel to the MDT wires, provide measurements for a fast p_T estimate used in the trigger. The cathode strips are arranged orthogonal to the wires and provide the position measurement along the MDT wire. The spatial resolution of the TGC is around 2-7 mm for both measurements.

2.3 ATLAS trigger system

The bunch crossing rate in LHC is 40 MHz, and each bunch crossing several MB of data is stored in the on-detector pipelines. This means the amount of data measured in ATLAS is far too large to allow every event to be written to storage. To reduce the total data flow without losing interesting physics events ATLAS uses a trigger system organized in three levels, as is illustrated in figure 2.9. Each step refines the previous decision by using a larger fraction of the data and more advanced algorithms. The level-2 trigger and the event filter use fast software algorithms to produce trigger information, while the level-1 trigger is implemented in the form of dedicated electronics.

Level 1 trigger

The level 1 trigger is a hardware based trigger that is designed to reduce the 40 MHz bunch crossing rate to an event rate of about 75 kHz. The level 1 trigger uses information from the calorimeter (with reduced granularity) and the RPC and TGCs in the muon system. The trigger electronics are designed to look for high-p_T muons, electrons, photons, jets and τ-leptons decaying into hadrons, as well as large missing transverse energies. The level 1 trigger has a latency of 2 μs. During this time the information of all detector channels is buffered to await the trigger decision.

Level 2 trigger

The level 2 trigger is a software trigger which uses the output of the level 1 and the full event information to further reduce the data rate to 1 kHz. The level 2 trigger uses information from the precision chambers to improve the momentum estimate. At this stage there is also the possibility to use information from tracks reconstructed in the inner detector. The LVL2 trigger has an event dependent latency varying from 1 ms up to 10 ms for events with high track multiplicity.

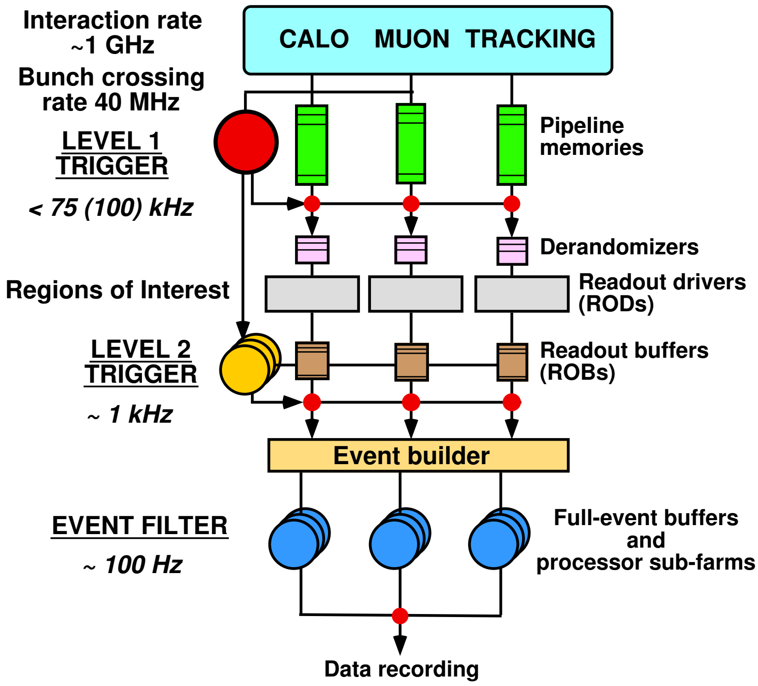

Figure 2.9: The ATLAS trigger scheme, indicating the various stages in which the data is processed and the event rates at the different trigger levels.

Event filter

The event filter further reduces the data stream by using information of more complex reconstruction algorithms such as Bremsstrahlung recovery for electrons and vertex finding. The event filter runs on a computer farm situated at CERN. The maximum output of the event filter is 100 Hz which corresponds to a data rate of 100 MB/s. All events that pass the event filter are written to mass storage and are available for further analysis with the ATLAS offline software.

Trigger menu and data streams

A flexible trigger menu is used in ATLAS to allow different types of data to be selected for further analysis. For example, a possible item on the trigger menu could be to require 1 muon with a p_T greater than 6 GeV (in the level 1 trigger) and a second muon with p_T >4 GeV (in the level 2 trigger). The possible trigger items are limited by the maximum output of the event filter. For example, at the design luminosity of the LHC a single muon trigger of p_T >4 GeV would take up the full output of the event filter. Items on the trigger menu thus have to be optimized based on the expected rates of the physics events that one wants to record.

It is planned to have five to ten physics streams. The ATLAS experiment has adopted the inclusive streaming model, i.e. an event passing the criteria of multiple trigger items may be directed to several streams. This makes the system simpler at the analysis stage since all events passing the same trigger are contained in the same stream. However, this results in duplicating event data, so the overlap between streams must be kept as low as possible. In addition to physics streams, there are two special types of streams. One is the express stream which will be used for prompt reconstruction with a short delay after the data-taking. The primary purpose of the express stream is monitoring and debugging before the bulk reconstruction, therefore events in the express stream consist of a sample of high-purity signal events from the physics streams. The other type of stream is the calibration stream which contains events triggered by calibration triggers used to collect a large data sample for detector calibrations. Events which caused errors during on-line running, e.g. time-outs, crashes etc. are sent to the debug stream to be investigated further.

Chapter 3

The Semi-Conductor Tracker Endcap

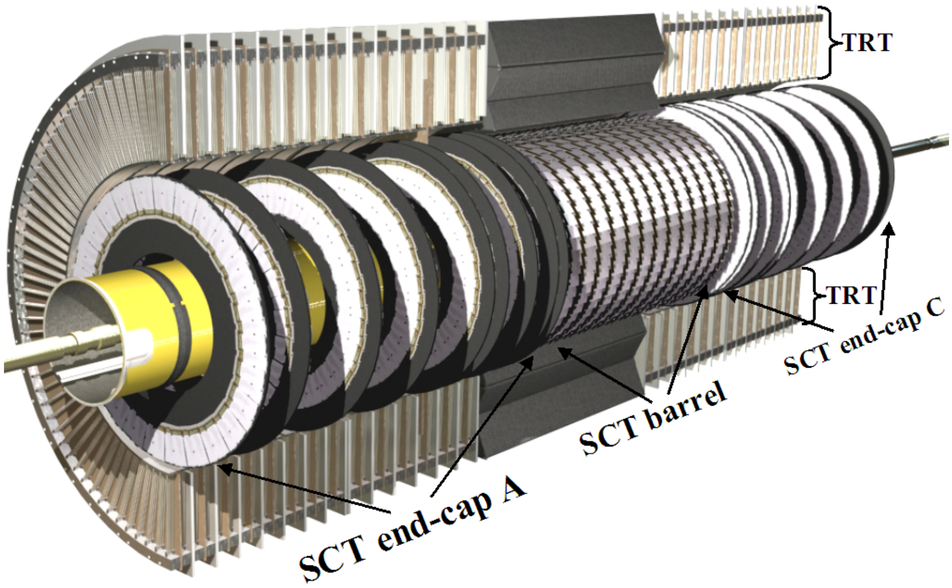

Figure 3.1: A 3D model of the ATLAS inner detector, showing the positions of the SCT barrel and end-caps.

The Semi-Conductor Tracker (SCT) is part of the ATLAS inner detector. The SCT provides high precision space-points used to reconstruct trajectories of charged particles. The SCT consists of silicon micro-strip detectors [21][22], a technology which has been used to construct precise tracking detectors in previous particle physics experiments [23].

In the central region of the detector the silicon micro-strip detectors are distributed over four concentric layers, that together form the SCT “barrel”. In each forward region the silicon micro-strip detectors are divided over nine disks, that together form one SCT "end-cap". Figure 3.1 shows the inner detector lay-out with indication to the SCT barrel and end-cap positions.

The SCT end-caps measure charged particles in the region 1.1-1.4 $< |\eta| <$ 2.5 and carry 1976 silicon strip detectors in total, accounting for nearly half of all the 4088 silicon strip detector in the ATLAS SCT.

The SCT end-cap on the 'A'-side of the ATLAS experiment was assembled and tested at the Nikhef institute in Amsterdam. The main assembly of the SCT end-cap at Nikhef took place during 2005 and 2006. The completed end-cap arrived at CERN in April 2006, where it was re-tested and integrated with the TRT end-cap before being put to its final place in the ATLAS detector in May 2007.

This chapter describes the detector requirements for the SCT end-cap, the operation principle of the silicon strip sensors, the SCT end-cap detector modules, and the various components in the end-cap required to support and operate the SCT modules.

3.1 Detector requirements

One of the challenges in building the ATLAS SCT end-cap is applying the same high precision mechanical techniques, used successfully in the building of previous silicon micro-strip based tracking devices, on a scale that is an order of magnitude larger than before. Another challenge comes from the LHC operating environment. The SCT is required to maintain an adequate detection performance after receiving an integrated radiation dose equivalent to a flux of $\sim 2 \times 10^{14}$ 1-MeV-neutrons/cm^2 [1], which is a factor 10-20 higher as seen by previous silicon detectors in hadron-collider experiments. Radiation hardness proved to be the biggest challenge in the design, and a period of over 15 years was used to develop the required radiation-hard technologies.
The main design requirements for the SCT end-cap follow from:

- **Number of space-points**

  The SCT and the pixel detector were designed with the requirement to measure a total of seven space-points along the track in order to accurately reconstruct track helices in three dimensions.

  The SCT end-cap is required to measure four space-points on the tracks in the region 1.1-1.4 $< |\eta| < 2.5$, another three space-points are measured by the pixel detectors.

- **High resolution**

[1] Estimated for 10 years of LHC running and multiplied by a factor 1.5 to take into account the uncertainties in the cross section and particle multiplicities at LHC energies [24].

The inner detector measures the curvature of tracks in the bending plane to determine the momentum of the particles. One of the inner detector requirements is to measure the p_T with precision better than 30% for tracks with p_T up to 500 GeV, which requires a resolution of ∼20 μm in the bending plane [24]. To allow separation of multiple primary vertices within a single bunch crossing, a resolution of ∼1 mm in the non-bending plane is required. The resolution in the non-bending plane is also required to resolve ambiguities in the pattern recognition, which is most difficult in events with high track multiplicity.

- **Noise occupancy and hit efficiency**

  In order for the pattern recognition to work properly, the noise occupancy per strip is required to be less than $5{\cdot}10^{-4}$, also after receiving the full irradiation dose. To satisfy this requirement, the threshold above which the signal is interpreted as a hit, needs to be at least 3.3 times higher than the average noise on the strip.

  For a typical value of the input noise on the silicon strips of ∼ 1500 electrons, the operating threshold is required to be >0.8 fC (4950 electrons).

  The hit efficiency is required to be >99%. This results in an upper limit for the threshold setting at which the signals are discriminated (of ∼1.3 fC) and the number of defective read-out channels in the detector must be kept below 1%.

- **Physics hit occupancy**

  The pattern recognition performance is degraded as the hit occupancies in the silicon strips increases. Since the SCT uses binary readout of the strips, the only way to resolve two tracks is to see them as two strips with at least one 'empty' (no hit) strip in between.

  Hit occupancies are required to be of the order of 1% or below, even within high P_T jets and at the high interaction rate at the full LHC luminosity, to reduce the chance of multiple hits in the same strip or a neighbouring strip.

  Satisfying the hit occupancy requirement while minimizing the number of channels was the main reason for limiting the strip pitch to around 80 μm. This strip pitch is also more than sufficient for satisfying the resolution requirements.

- **Material budget**

  Particles that traverse the inner detector will interact with the material in the detector. This leads to the deviation of charge particle trajectories through multiple Coulomb scattering and, in the case of electrons, highly fluctuating energy losses due to Bremsstrahlung.

The amount of multiple Coulomb scattering can be parametrized by the angle θ_{scat}, which is defined as the width of the Gaussian approximation for the projected scattering angle distribution. This angle is given by [25]:

$$\theta_{scat} = \frac{13.6\mathrm{MeV}}{\beta cp} z \sqrt{x/X_0} \left[1 + 0.038 \ln\left(x/X_0\right)\right], \tag{3.1}$$

where p is the momentum, βc is the velocity and z is the charge number of the incident particle, and x/X_0 is the thickness of the scattering medium measured in radiation length, X_0.

From equation 3.1 it is clear that the number of radiation lengths seen by a particle traversing the detector has to be minimized in order to prevent the loss of tracking resolution due to multiple scattering. The radiation length of a material is defined as the mean distance over which a high-energy electron loses all but $1/e$ of its energy by Bremsstrahlung. For most relevant materials X_0 is approximated by a phenomenological fit with reasonable accuracy (<3%) by [4]:

$$X_0 = \frac{7164 \cdot A}{Z(Z+1)\rho \ln\left(287/\sqrt{Z}\right)} \mathrm{g \cdot cm^{-2}}, \tag{3.2}$$

where Z is the atomic number of the material, A the atomic weight and ρ is the density.

To optimize the tracking performance of the SCT, it is important to minimize the total number of radiation lengths seen by particle traversing the detector. Equation 3.2 shows that the use of elements with a low atomic number Z and low density ρ are preferred.

In the original design of the inner detector [24], the SCT was designed to have a maximum amount of material corresponding to 10% of a radiation length.

- **Radiation hardness**

  In order for the SCT end-cap to survive during the lifetime of the ATLAS experiment, the front-end electronics were designed to work while receiving a large amount of radiation [26]. The silicon sensors are severely affected by radiation damage, as is explained in detail in section 3.2.4, which leads to the requirement to keep the silicon cooled.

3.2 Silicon strip detectors

This section describes how the SCT end-cap modules use silicon strip detectors to measure the position of the passage of a charged particle. The effects of radiation damage on the silicon sensor are discussed at the end of the section.

3.2.1 Ionization and creation of electron-hole pairs

Moderately relativistic charged particles other than electrons lose energy in matter primarily by ionization and atomic excitation. Electron-hole pairs are created from the ionizing energy losses. The mean rate of energy loss can be approximated using the Bethe-Bloch equation [4]:

$$-\frac{dE}{dx} = Kz^2\frac{Z}{A}\frac{1}{\beta^2}\left[\frac{1}{2}\ln\frac{2m_ec^2\beta^2\gamma^2T_{max}}{I^2} - \beta^2 - \frac{\delta(\beta\gamma)}{2}\right], \qquad (3.3)$$

where β and γ follow from the velocity of the particle: $\beta=v/c$ and $\gamma=1/\sqrt{1-\beta^2}$, and m_e is the electron mass, equal to 0.510 MeV. T_{max} is the maximum kinematic energy that can be transferred to a free electron in a single collision and depends on the mass and momentum of the incident particle. K is a constant which can be defined as K=0.307 MeVg^{-1}cm^2, so that the energy loss dE/dx is given in units of MeVg^{-1}cm^2. To find the energy loss per unit of thickness, dE/dx needs to be multiplied with the density ρ of the traversed medium.

I is the mean excitation energy of the atoms averaged over all electrons. The mean excitation energy has been estimated for various materials using experimental measurements of the energy loss [27]. The term $\delta(\beta\gamma)$ is due to the 'density effect' [4], which decreases the average energy loss for highly relativistic particles in dense media.
Table 3.1 gives the value of the constants in equation 3.3 for silicon as the scattering medium.

Property	**Value**
Atomic number, Z	14
Atomic weight, A	28.09 g·mol^{-1}
Density, ρ	2.33 g/cm^3
Mean excitation energy, I	174 eV

Table 3.1: Relevant properties of silicon at room temperature.

Particles with a value of $\beta\gamma$ that corresponds to the minimum of the Bethe-Bloch equation, are called Minimum Ionizing Particles (MIPs). For a MIP passing through silicon, the Bethe-Bloch equation predicts an average energy loss of 388 eV/μm.

Energy losses are of a stochastic nature, and the Bethe-Bloch formula predicts the average value of the energy loss distribution. The distribution of energy loss in a thin absorber is described by Landau theory [28]. A Landau distribution has a large tail and peaks well below the value of the average energy loss. For this reason, the most probably energy loss is a more meaningful variable than the average energy loss.

The most probably energy loss per unit thickness Δ_p/x, normalized to the mean rate loss rate by a minimum ionizing particle Δ_E/dx_{min}, is shown in figure 3.2, for silicon layers with various thickness x. The figure shows that the energy losses increase relatively slowly after the minimum, so that most particles with momentum of a few GeV or more can be approximated to behave as MIPs.

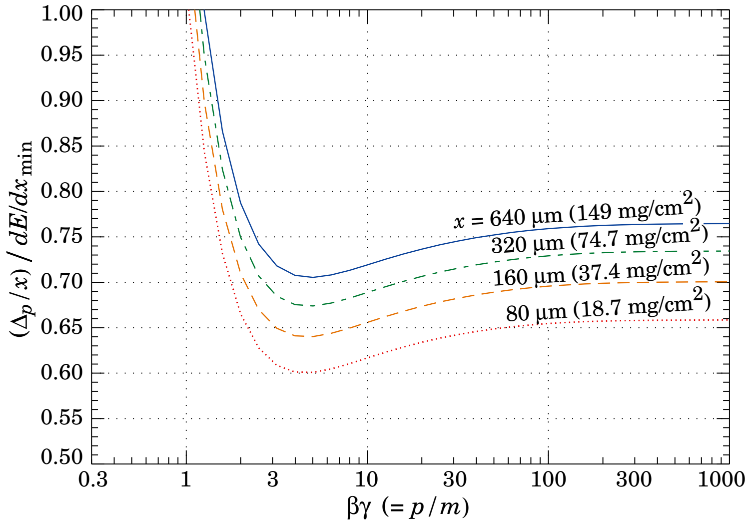

Figure 3.2: Most probably energy loss in silicon, scaled to the mean loss of a minimum ionizing particle, Δ_E/dx_{min}=388 eV/μm [4].

The energy loss is partly absorbed by electrons in the silicon, which move from the valence band to the conduction band. Silicon is a so-called semi-conductor, meaning that its conduction and valence band are separated by a small band-gap (1.12 eV). The electron deficiency that is left in the valence band when an electron moves to the conduction band may be filled by one of the neighboring electrons, resulting in a shift of the deficiency location. This mobile deficiency location can be treated as a positively charged particle and is called a 'hole'. This means that an electron moving from the valence to the conduction band results in an electron-hole pair.

Not all energy loss is used for electrons to cross the band-gap, since some energy loss results in excitations of the silicon lattice. The average energy loss required to create an electron-hole pair is defined by the *ionization potential*, which for silicon is 3.62 eV. The band gap for silicon is relatively low, which renders it possible to make very thin detectors and still produce a reasonable signal. The most probably energy loss for a minimum ionizing particle in an ATLAS silicon sensor (thickness=285 μm) at normal incidence is 75 keV. From this it follows that for minimum ionizing particles, the most probable charge deposition in the ATLAS silicon sensor, is 3.3 fC ($21{\cdot}10^3$ electrons).

3.2.2 The reverse biased p-n junction

The electron-hole pairs created by ionization are measured by the current they induce when they move under the influence of an externally applied electric field. This current needs to be distinguished from the *leakage current* which is induced by thermally created electron-hole pairs and mobile charge carriers created by impurities in the silicon lattice. In order to minimize the leakage current and detect the signal, silicon detectors use reverse biased *p-n junctions* [29].

A p-n junction is formed by placing together n-type and p-type silicon. These different types of silicon are formed by adding impurities to the silicon. Pure silicon consists of a silicon lattice where the four valence electrons of each atom create bonds with neighboring atoms. Adding elements with five valence-electrons creates *n-type* silicon, that contains extra valence or 'donor' electrons. Addition of elements with three valence-electrons creates *p-type* silicon, that contains extra holes or 'acceptors' in the silicon lattice.

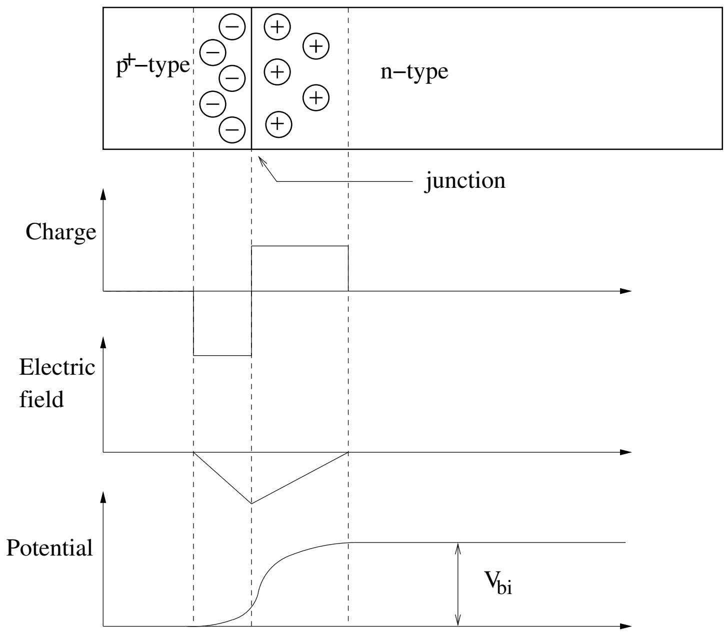

Figure 3.3: The electrical properties of a p-n junction showing the charge, electric field and potential that are induced around the junction.

When p- and n-type silicon are placed together, a p-n junction is formed, with a specific set of electric properties that are illustrated in figure 3.3. Through the junction, electrons from the n-type diffuse to the p-type to fill the holes and vice versa. The absorption of charge carriers in the originally neutral material leads to a build-up of charge, which creates a potential difference, V_{bi}. The charge diffusion between the p- and n-type results in a region depleted of mobile charge carriers, called the *depletion area.* At a certain point the electrical field generated due to the removal of free charge is big enough that it counteracts any further diffusion of electrons and holes.

The p-n junction forms a diode, as the current can flow in only one direction, namely from the p-type to the n-type. The depletion area over the p-n junction can be enlarged by applying an external voltage in the same direction as the potential created by the charge build-up. This external potential opposes current flow and is usually referred to as the *reverse bias voltage.*

The SCT silicon sensor [30] uses an n-type substrate in which the p-type is implanted in the form of strips, to form a position-sensitive detector. Figure 3.4 shows a schematic cross-section of the SCT silicon sensor.

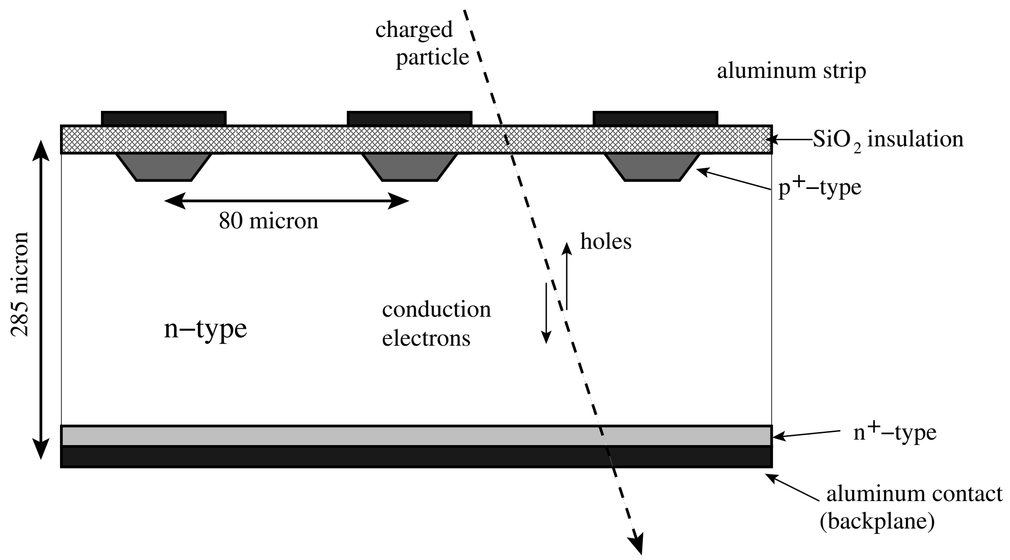

Figure 3.4: Schematic cross-section of an ATLAS silicon sensor.

When electron-hole pairs are formed in the silicon, the holes drift to the strips and the electrons drift to the backplane. The holes (=positive charge) induce a negative charge in the strips, that gives rise to a current. This current is read-out through aluminum strips which are capacitively coupled with the p-type implants via an insulating silicon-oxide layer. The SCT silicon sensor contains a total of 768 read-out strips. A common ground rail is connected to all strips via a resistor to keep the strips at a potential of 0 Volt.

The material in the p-type strips is also denoted as p^+-type, since it has a doping concentration of approximately a factor 100 larger than the n-type. This allows a large thickness of n-type to be depleted using a thin layer of p^+-type. The reverse bias voltage where the full thickness of n-type bulk is depleted, the depletion voltage V_{dep}, is given by: [31]

$$V_{dep} = \frac{qd^2}{2K_s\epsilon_0}\frac{N_D(N_A + N_D)}{N_A} = \frac{qd^2}{2K_s\epsilon_0}|N_{eff}|, \tag{3.4}$$

where d is detector thickness, q is the charge of the electron and $K_s\epsilon_0$ is a material constant (~1 pF/cm for silicon), N_A is the doping concentration of the p-type material and N_D the doping concentration of the n-type material. Typical dopant concentrations in detector applications are of the order of 10^{12} for the n-type material and up to 10^{14} for the p^+ implants. For the silicon sensors used in the ATLAS silicon detector (d=285 μm), full depletion can be obtained with bias voltages of less than 100 V.

Radiation damage in the silicon changes the values of the doping concentrations in the silicon, as will be explained in section 3.2.4. This leads to a change in the effective dopant concentration, N_{eff}, and eventually leads to a much higher voltage required to fully deplete the silicon.

The SCT sensor is designed to be biased with a voltage of up to 500 Volt. The sensors were required to have a maximum leakage current (before irradiation) of 6 μA at V_{bias}=150 Volt and maximum 20 μA at V_{bias}=350 Volt.

Two different manufacturers were responsible for the production of the silicon sensors: Hamamatsu[2] and CiS[3]. Detailed information about the production of the silicon micro-strip sensors can be found in [30].

3.2.3 Resolution

The SCT end-cap modules are wedge-shaped with a constant ϕ-pitch between the strips. This results in a spread on the strip pitch, P, which ranges from 57 μm to 94 μm. ATLAS has opted for binary readout so that each strip provides hit-or-no-hit information and the single strip resolution follows directly from the strip pitch as:

$$\sigma_{strip} \equiv \sqrt{\bar{x^2} - \bar{x}^2} = \sqrt{\frac{1}{P}\int_{\frac{-P}{2}}^{\frac{P}{2}} x^2 dx} = \frac{P}{\sqrt{12}} \approx 16 - 27\ \mu\text{m} \tag{3.5}$$

The SCT detector uses two silicon sensors that are placed back-to-back under a small stereo-angle of 40 mrad. Hits in two overlapping strips are combined to form a 3D *space-point*. The space-point has a resolution perpendicular to the strip axis (σ_x) and a resolution along the strip axis (σ_y) given by:

$$\sigma_x = \frac{\sigma_{strip}}{\sqrt{2}} \approx 11 - 19\ \mu\text{m} \tag{3.6}$$

$$\sigma_y = \frac{\sigma_{strip}}{\sin(40\text{ mrad})} \approx 400 - 675\ \mu\text{m} \tag{3.7}$$

[2]Hamamatsu Photonics Co. Ltd., Japan.
[3]CiS Institut f'ur Mikrosensorik gGmbH, Germany

These resolutions satisfy the requirements for the tracking capabilities of the SCT end-cap as mentioned in section 3.1.

3.2.4 Radiation hardness

The LHC collisions cause an enormous flux of radiation in the ATLAS experiment, which will affect the detector performance. Radiation hardness is especially important to the SCT and other inner detector components, due to their close proximity to the collision point.

In general, radiation damage in silicon [32] leads to a change in various properties of the SCT silicon sensor. Two types of radiation can be distinguished: ionizing radiation, caused by charged particles, and non-ionizing radiation, mainly caused by hadronic particles. The non-ionizing radiation causes dislocation of atoms and nuclear reactions that create impurities in the silicon lattice, while ionizing radiation creates mobile or trapped electron-hole pairs.

The creation of impurities in the silicon lattice means a change in the effective doping, N_{eff}, of the silicon sensors. The depletion voltage, V_{dep} depends on the effective doping concentration, as was shown in formula 3.4.

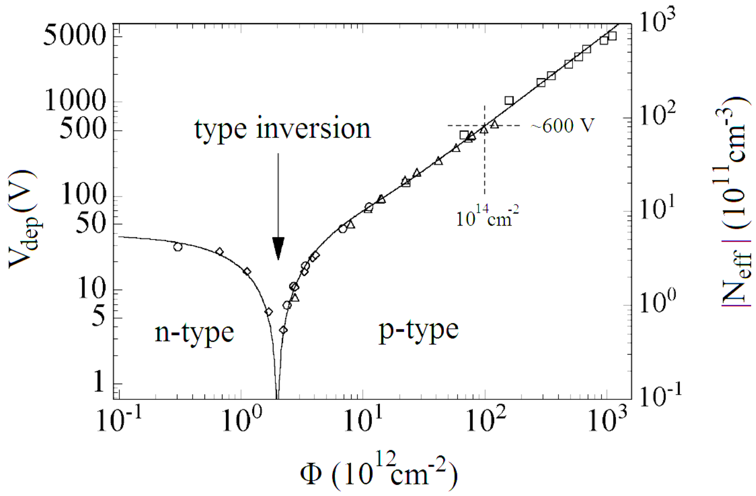

Figure 3.5: Change of the depletion voltage V_{dep} and effective doping concentration N_{eff} in the SCT silicon sensor, as a function of particle fluence [32].

Figure 3.5 shows the expected change of V_{dep} and N_{eff} as a function of the particle fluence Φ, which is expressed in an equivalent radiation flux of 1-MeV neutrons per cm^2. The figure shows that the change in N_{eff} eventually results in *type inversion*, where the n-type becomes an effective p-type. After type-inversion, the diode junction moves from the strip-side to the n^+p-junction on the opposite side of the sensor. The expected radiation dose after 10 years of

LHC running is equivalent to $2{\cdot}10^{14}$ 1-MeV-neutrons/cm^2, corresponding to a expected depletion voltage of 500 Volt.

Apart from changing the depletion voltage, the radiation damage in the silicon also leads to an increase of the noise on the strips and the decrease of the charge collection efficiency. The increase in the noise is caused by the increased shot noise from the extra leakage current as well as by an increasing inter strip capacitance created by the build-up of charge from trapped electron-hole pairs in the oxide layer. At the same time the charge collection efficiency is reduced, as the creation of traps for mobile charge carriers leads to a loss or late arrival of the signal.

Test were done on prototypes of the SCT modules to find the effect of irradiation on the noise occupancy and efficiency [33] for a radiation dose equivalent to 10 years of LHC running. The results of these tests are shown in figure 3.6. Before irradiation the detection efficiency and noise occupancy are within specification over a large range of the operating threshold, between 0.7 to 1.3 fC. After irradiation, only a narrow range around a threshold of 1.2 fC remains to operate the modules within specification.

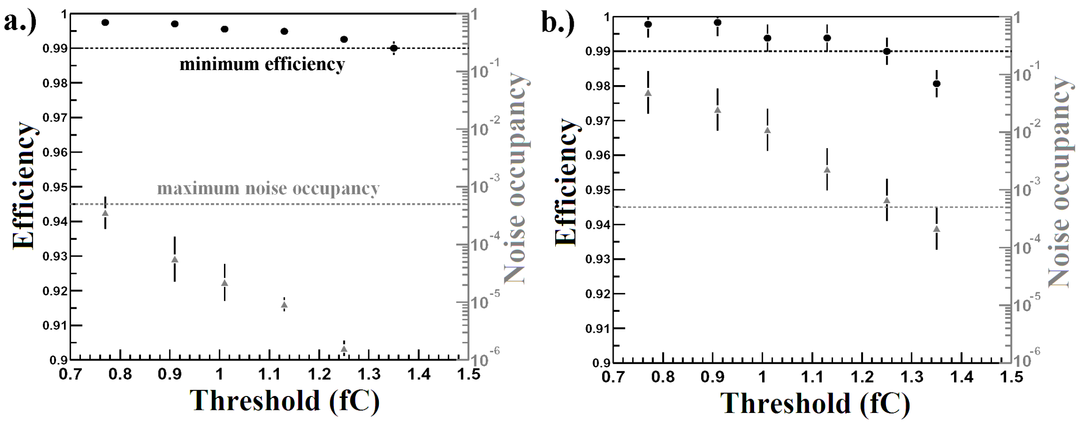

Figure 3.6: Efficiency (circles) and noise occupancy (triangles) as measured on prototype SCT modules [33] (a) before irradiation (b) after irradiation.

After receiving radiation damage, thermal movement of the atoms over time will initially counteract the change of the doping concentration. This process is called *beneficial annealing* and results from dislocated atoms that are thermally vibrated back in to the silicon lattice [34]. At the same time, another (slower) process occurs called *reverse annealing*, which accelerates the change in doping concentration as impurities diffuse further in the silicon lattice.

The time at which the reverse annealing starts to dominate over the beneficial annealing depends on temperature [32], as lower temperatures slows the thermal movements of the atoms. Also with decreasing temperature more and more defects are not able to re-emit a captured charge carrier, so charge carriers are effectively frozen in place and compensate the defects.

Therefore, the SCT detector was designed to have the silicon sensors in the SCT end-cap cooled at -7 °C. At this temperature the modules will remain operational for at least 10 years of LHC running, taking into account that the detector will from time to time be warmed up during short maintenance shutdowns.

3.3 The SCT end-cap module

Each SCT end-cap module is composed of two silicon strips sensors and electronics to read-out the signals on the strips. A total of 988 detector modules are divided over the nine disks in one SCT end-cap to cover the required forward detector volume.

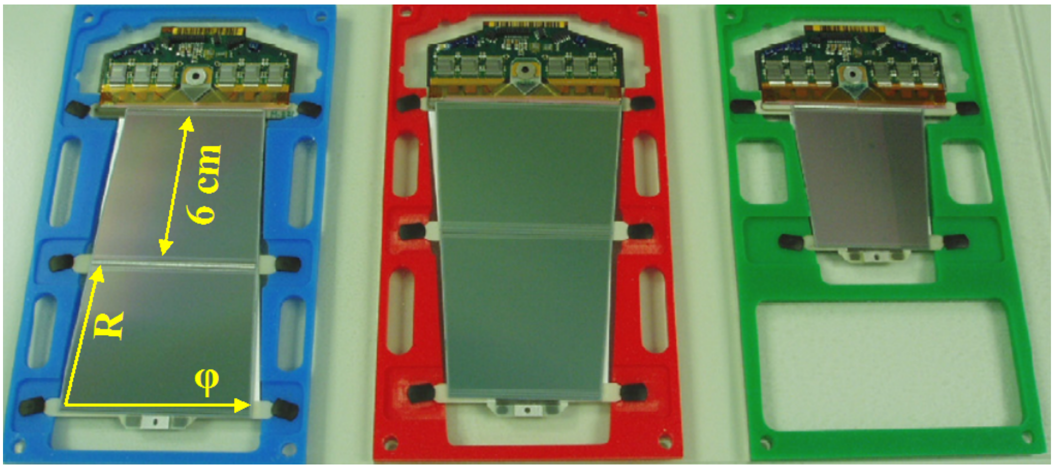

Figure 3.7: Example of three types of end-cap modules. From left to right: Outer, Middle and Inner module.

The SCT end-cap modules are referred to as Inner, Middle and Outer modules, to indicate their relative radial position on the disk. Examples of three out of the four different types of SCT end-cap modules are shown in figure 3.7. The fourth type of module is the so-called Short-Middle, which follows the design of a Middle module with only one pair of silicon sensors[4]. The different SCT end-cap modules vary slightly in shape and size but all the modules follow the same design concept.

[4]The Short-Middle modules was required for the middle ring of disk 8, since at the z-position of this disk a line corresponding to $|\eta| = 2.5$ would cut a standard middle module in half.

3.3.1 Module design

The design of the SCT modules was optimized within the constraints for radiation hardness, high rate capability, low mass and redundancy options [21]. The main components of the module are indicated in figure 3.8.

Each module consists of two silicon sensor surfaces, that are glued back-to-back onto a spine with a relative stereo angle of 40 mrad. The spine gives mechanical support to the module and connects the back planes of the sensors to the bias voltage. The spine is made from Thermal Pyrolytic Graphite, which has a good thermal conductivity to transport heat generated in the sensors to the module cooling system. The aluminum strips on the silicon sensors are wire-bonded to the ABCD read-out chips, that are supported by the front-end electronics 'hybrid'[5].

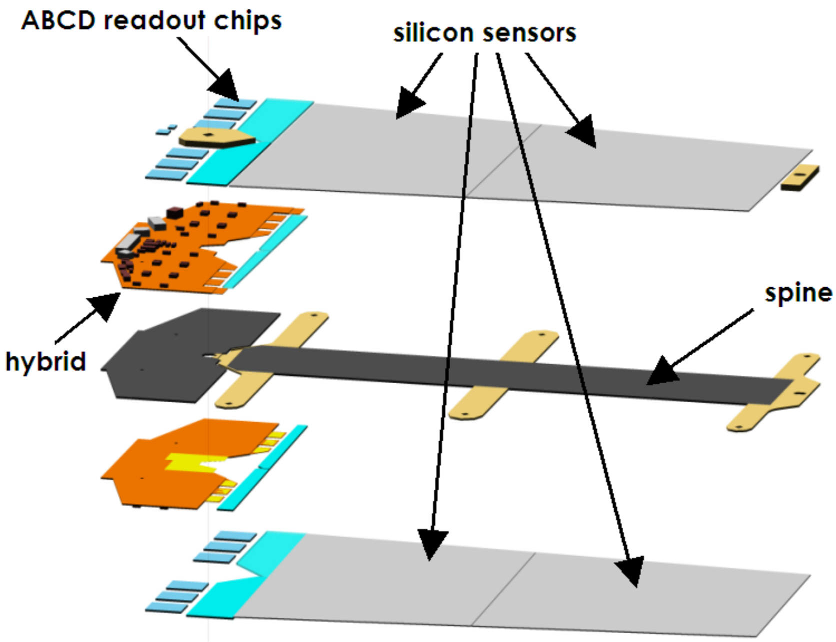

Figure 3.8: Exploded view of an SCT end-cap module showing the different components.

The precision on the silicon sensors position determines the tracking resolution and should be known as precisely as possible. The modules were built with an internal precision of the order of 10 μm, and with a tolerance of 5 μm in the $R\phi$ direction [21]. Two washers made out of glass fiber with a aluminum precision inserts, are glued onto the spine and determine the precision of the mounting position of the sensors on the discs. The alignment software can determine the sensor position with a precision of the order of 1 μm, which re-

[5]Hybrid of mounted chips and integrated circuitry on the base board.

duces the need for very precise placement of the modules. However, the more accurate the position is known in advance, the more readily the alignment procedures will converge on an accurate position.

Five different types of trapezoidal-shaped silicon sensors are used to form the active surfaces of the four types of end-cap modules. The different dimensions of the silicon sensors are shown in Table 3.2. The Outer and Middle modules need a longer silicon strip surface that is created by combining two silicon sensors, with wire-bonds to connect the strips from one sensor to the next.

Sensor type	End-cap module	Length (mm)	R_{center} (mm)	inter-strip angle (μrad)	strip pitch (mm)
W12	Inner	61.060	304.55	207.0	56.9-69.2
W21	Middle	61.085	369.16	207.0	69.9-83.0
W22	(short-)Middle	54.435	429.07	207.0	83.4-94.2
W31	Outer	65.540	470.56	161.5	70.9-81.1
W32	Outer	57.515	532.22	161.5	81.5-90.4

Table 3.2: The different types of end-cap sensors; showing the dimension, distance from the beam (R_{center}) and strip pitch of each sensor type

The total strip length, and thus the dimension of the module, was limited by the capacitive load on the read-out channels. In order to achieve a maximum input noise of 1500 electrons, the capacitive load may not exceed 18 pF, so that the total the length of the strips had to be smaller than 12 cm.

3.3.2 Front-end electronics

The front-end electronics are responsible for processing the silicon strip signals, decoding the incoming clock and command signals, and returning data to the off-detector data acquisition system. These tasks are performed by the three types of ASICs (Application Specific Integrated Circuits) that are present on the electronics hybrid of each module:

- 12 ABCD3TA chips [35] are used on each module to read-out and process the signals measured on the silicon strips. Each chip processes the data of 128 strips to create a binary output signal that is stored in the pipeline, while awaiting the trigger decision.

- The VDC chip [26] provides the driver current for the two laser diodes that return the optical data stream from the module.

- The DORIC4A chip [26] decodes the signal from the light-sensitive diode that receives the clock and command data.

The required components for the opto-electronic conversion of the signal are placed in the opto-plugin which connects to the hybrid of each module. A photograph of the module hybrid is shown in figure 3.9 with indications to the different ASICs and the connectors for the opto-plugin and power tape. The photograph also shows the redundancy link connectors, which allows neighboring module hybrids to be connected via a tape, so that clock and command signals can be passed between those modules.

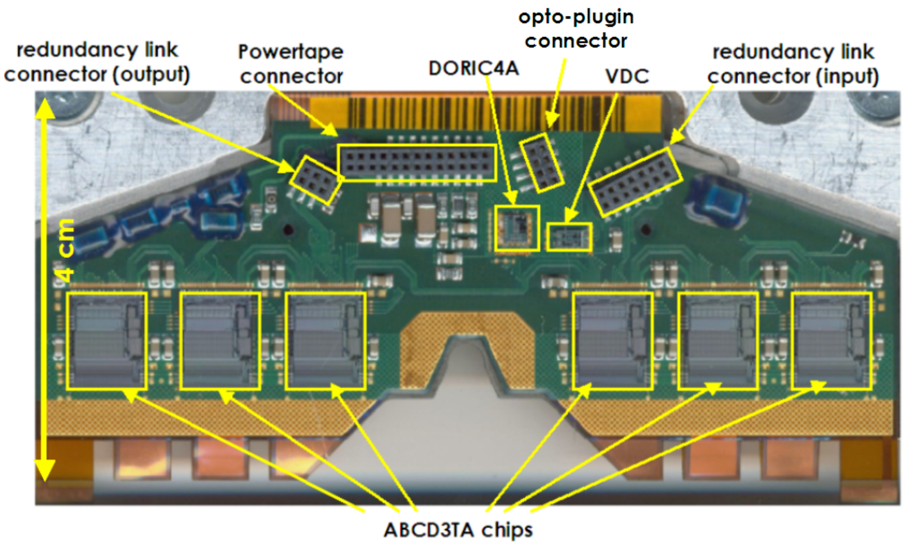

Figure 3.9: Front side of an SCT end-cap module hybrid. Another 6 ABCD3TA chips are placed on the back side of the hybrid.

The hybrid is thermally decoupled from the silicon sensor to prevent the heat generated in the chips from warming up the silicon. The electrical connection between each silicon strip and its corresponding channel on the read-out chips is established through the fan-ins, which are made of isolating glass substrates with metal tracks.

The ABCD3TA readout chip combines digital and analog functionality into a single chip, as is discussed in the following sections.

Analog functionality

The analog functionality of the ABCD chip includes pulse shaping, amplification and discrimination for 128 readout strips. The analog stages for a single channel are indicated in figure 3.10.

The front-end circuit amplifies the signal induced on the strips, integrates the current induced by incoming electron-hole pairs over time and shapes the

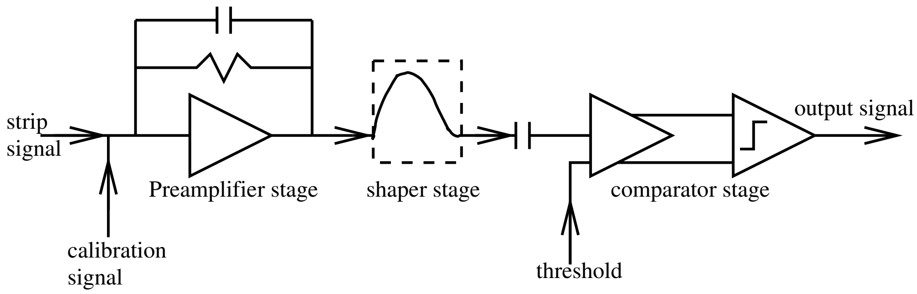

Figure 3.10: Schematic diagram of the analog stages of a single channel as implemented in the ABCD3TA chip.

signal, in order to create a signal with a typical peaking time of 25 ns. The shaped signal then passes through a comparator that discriminates the signal with a given threshold to produce a binary (hit-or-no-hit) signal. The discriminating threshold is set in the chip configuration register by an 8-bit DAC that is the same for all 128 channels. In addition a 4-bit TrimDAC is used to correct differences in the response between the channels in one chip.

The ABCD3TA has an integrated calibration circuit to determine the response of each channel (in mV/fC) by injecting a calibration signal corresponding to a known charge and evaluating the response over a range of thresholds. The calibration circuit is an important tool for studying the module performance, as is discussed in detail in chapter 5.

Digital functionality

After the analog stages, the signal on each strip is represented by a hit or no-hit binary signal. The digital functionality of the ABCD3TA chip controls the storage of the hit pattern in a digital pipeline, while awaiting the read-out command. Figure 3.11 shows a block diagram indicating the functionality of the ABCD3TA chip, including the digital functionality after the analog stages.

The chip can be operated in pulse or edge mode. In edge mode, a hit is only stored if the preceding time bin had no hit, while in pulse mode, a hit is always stored. After this, a mask is applied, which allow channels to be switched on or off, irrespective of the hit in that channel. The mask can be used to switch off noise channels, and is also used in test sequences to feed specific hit patterns into the pipeline.

Including margins for the fiber lengths on top of the 2 μs level 1 trigger latency, a maximum level 1 trigger latency of 3.2 μs is assumed, which requires a 132 cells deep pipeline clocked at 40 MHz. On receipt of a level 1 trigger, the bit corresponding to the triggered bunch crossing, as well as the bits from one time-bin before and after are retrieved from the pipeline and sent to the read-out buffer. A total of 8 events, each event corresponding to a 3-bit hit

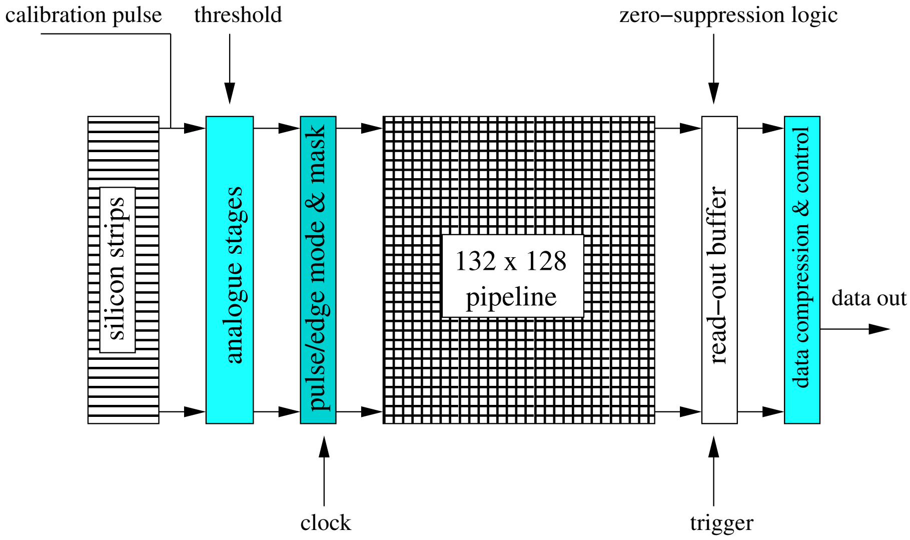

Figure 3.11: Block diagram indicating the functionality of the ABCD3TA chip.

Name	Hit pattern	usage
any-hit	1XX,X1X,XX1	detector timing
level	X1X	data taking
edge	01X	data taking with additional noise rejection
test	XXX	testing

Table 3.3: The four possible modes of the zero-suppression logic. X indicates that the state of the bit can be either 0 or 1.

pattern, can be stored in the read-out buffer. Zero-suppression logic is applied to the 3-bit hit pattern. Table 3.3 shows the four possible modes of the zero-suppression logic. The data is added to the output data stream when the hit pattern matches that of the selected mode.

Data from the 12 chips is routed to the two input lines of the VDC chip. The VDC chip decodes the signal and sends the module data to the read-out system via two optical data links. The chip configuration settings determine how the data on each module is routed. A chip can be configured as Master (M), Slave (S) or End (E). Read-out is controlled by token passing and is initiated by the End chips. On receipt of the token the End chip sends its zero suppressed data to the first Slave chip, which adds its own data to the received data, and passes the data along the second Slave chip, and so on, until the data arrive at the Master chip. When the Master chip receives the data, it adds its own data and sends the data of the entire chain to one of the two input of the

VDC-chip. A typical chip configuration is illustrated by figure 3.12, showing two data chains that each consist of a Master, four Slaves and an End chip.

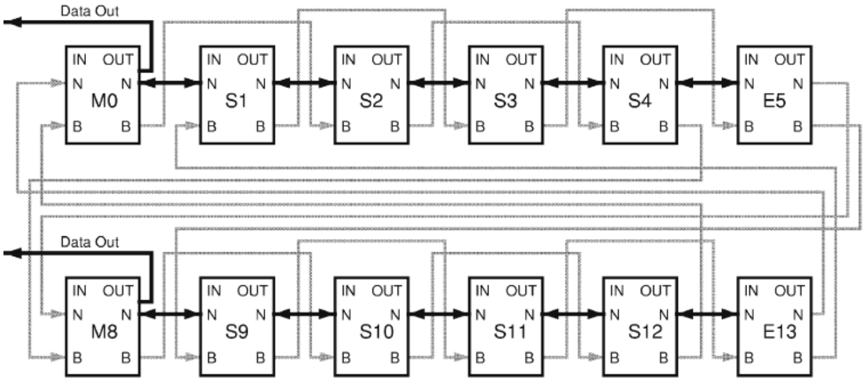

Figure 3.12: Interconnection of the 12 ABCD3TA chips on one SCT module, showing the normal data-paths (black) and alternative data paths (gray).

An alternate data path is available so that a non-functioning chip can be bypassed, effectively removing the chip from the data-chain. Note that only two chips on each module are connected to the two VDC input lines. If one of these two chips is configured as Slave instead of Master, the two separate data chains can be combined into a single one, so all data is send to one optical link. This way, in case of problems with one optical link, the chip configuration settings can be used to send all the data to the other link.

3.4 SCT end-cap lay-out

The SCT end-cap is required to measure four space-points in the forward region up to $|\eta|$=2.5 within the overall active volume constraints of a radius between 275 mm and 560 mm and position along the beam-pipe of 850 mm$<|z|<$2800 mm. This resulted in the choice of a lay-out consisting of nine disks [24], where each disk is covered with up to three rings of detector modules.

Figure 3.13 shows photographs of the front and rear of one disk that contains all three rings of modules, denoted as outers, middles and inners. The outer ring consists of 52 modules, while the middle and the inner rings consist of 40 modules each. The modules are placed such that there is a small overlap between each module and its neighbor. The non-sensitive part of the module, containing the read-out electronics, is occupying part of the disk. In order to obtain an active silicon surface over the full disk, the middle modules are placed on the back of the disk.

To reach the required η coverage not all disks needed to contain the middle and/or inner ring of modules. This is illustrated in figure 3.14 which shows

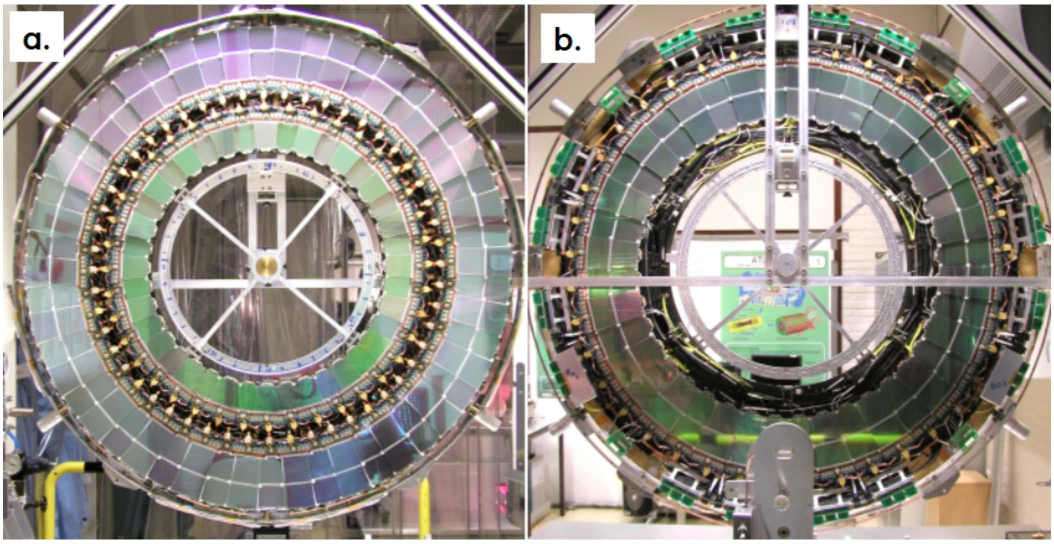

Figure 3.13: Photographs of disk 5 in the module mounting stand at NIKHEF. **a.** The front of the disk showing the Outer and Inner modules. **b.** The back of the disk showing the Middle modules.

a schematic view of one quarter of the detector, showing the positions of the nine disks and the silicon sensor surface of the modules mounted on each disk.

To maximize the coverage in η for disk 9 within the allowed z constraints, disk 9 is rotated around the y-axis so that its outer modules are facing outward relative to the interaction point, while the outer modules on all other disks are facing inward.

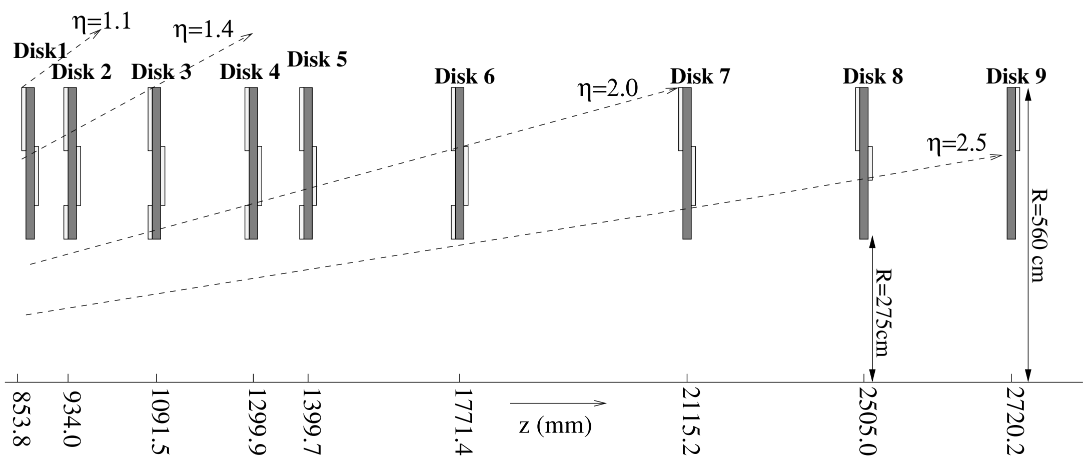

Figure 3.14: Schematic view of the SCT end-cap layout. The distance to the interaction point (Z) and the distance to the beam (R) is indicated.

3.4.1 Support structure

The SCT end-cap support structure consists of a cylindrical structure holding nine disks. The structure is made of carbon-fiber reinforced epoxy which maintains adequate stiffness while minimizing the material in the detector [36]. This material was designed to have dimensional changes of less than 0.025% for temperature changes between −15°C to 20°C.

The nine disks that support the detector modules in one end-cap were designed to have an outer radius of 567.0±0.2 mm, an inner radius of 267.0±0.2 mm and a thickness of 8.7±0.2 mm [36]. Various mounting points and holes have been machined on the disks, to facilitate the routing of the cooling circuits, fibers and power tapes over the disk surface. To ensure that the entire disk is grounded, aluminum-polyimide grounding foils are placed over the disk surface.

The disks are placed inside a cylindrical support structure, in which the disks can be accurately positioned, and which provides a surface for the fibers and power cables to be routed upon. Openings are constructed inside the cylinder to allow connections for the fiber and cables to be made at the disk periphery. The entire cylinder is grounded with a copper-polyimide ground sheet that covers the outside of the cylinder surface. The cylinder itself is supported by the front and rear 'wings', as is depicted in figure 3.15. Mounting points at the end of the wings are used to mount the SCT onto rails located on the inside of the solenoid cryostat.

The cylinder is surrounded by thermal enclosures that are equipped with heating pads to provide an active thermal barrier between the SCT and the TRT. The thermal enclosures also help contain the dry N_2 gas[6] within the SCT end-cap so that it does not contaminate the TRT.

3.5 Module services

Module services provide power, cooling and optical communication to all the SCT modules in the end-cap. The services can be divided in the *disk services* and *cylinder services*. Figure 3.16 shows a photograph illustrating the disk services. These services terminate at the outer radius of each disk at a set of patch-panels where they are connected to the cylinder services.

The cylinder services consist of the power tapes, optical fibers and cooling lines that are routed over the outer surface of the cylinder. The on-cylinder services terminate at the far-end[7] of the SCT end-cap, where a connection is made with the cables and cooling pipes that connect the SCT end-cap with the systems in the services-caverns.

[6] The SCT end-cap is flushed with N_2 gas to keep the dew-point below the temperature on the cooling circuits.

[7] The side of the SCT cylinder located furthest from the interaction point.

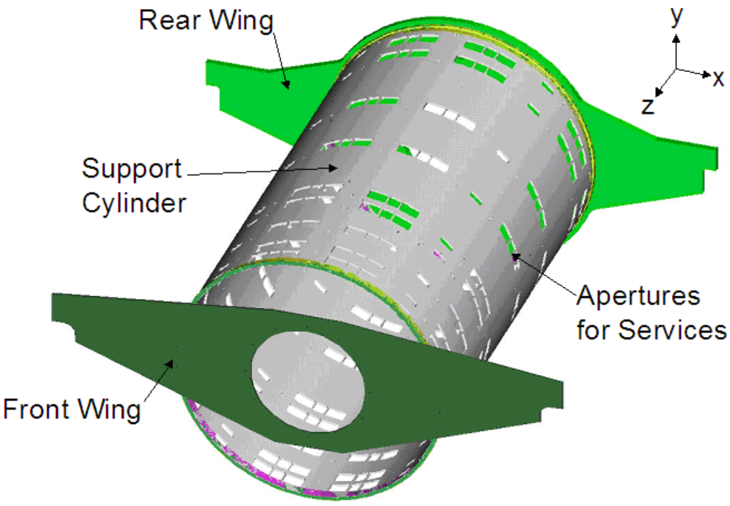

Figure 3.15: A schematic lay-out of the SCT cylinder support structure.

The services inevitably add a significant amount of material to the SCT end-cap. Special care was taken in the design of the services, using thin and low Z material to reduce the number of radiation lengths traversed by particles in the inner detector.

3.5.1 Power tapes

Power tapes connect at the modules and are routed to the edge of the disks where they connect to the power tapes on the cylinder surface. Power tapes on the cylinder connect to the long power cables at the far-end of the end-cap that are connected to power supplies in the ATLAS services caverns. Each power cable carries the power of an individual module to a specific channel on one of the power supplies.

All the voltages required to operate an SCT module are listed in Table 3.4. The RESET and SELECT links are used, respectively, to send the reset command to the read-out chips and to configure the module to use its redundant clock input. By far the most current is drawn for the analog (V_{cc}) and digital (V_{dd}) power supply of the ABCD3TA chips.

The distance between the power supply cards and the SCT end-cap is ~80 meters, creating a significant voltage drop over the cable. Two sets of sense-wire lines are incorporated in the power tapes to monitor the voltage drop over the V_{dd} and V_{cc} lines, allowing the power supply card to compensate the voltage drop so that the required voltage arrives at the module.

Special power tapes are used in SCT end-cap to minimize the material contribution within the available surface on the support structures. So-called *wiggly tapes* are placed on the surfaces of the disks and *Low Mass Tapes* (LMTs)

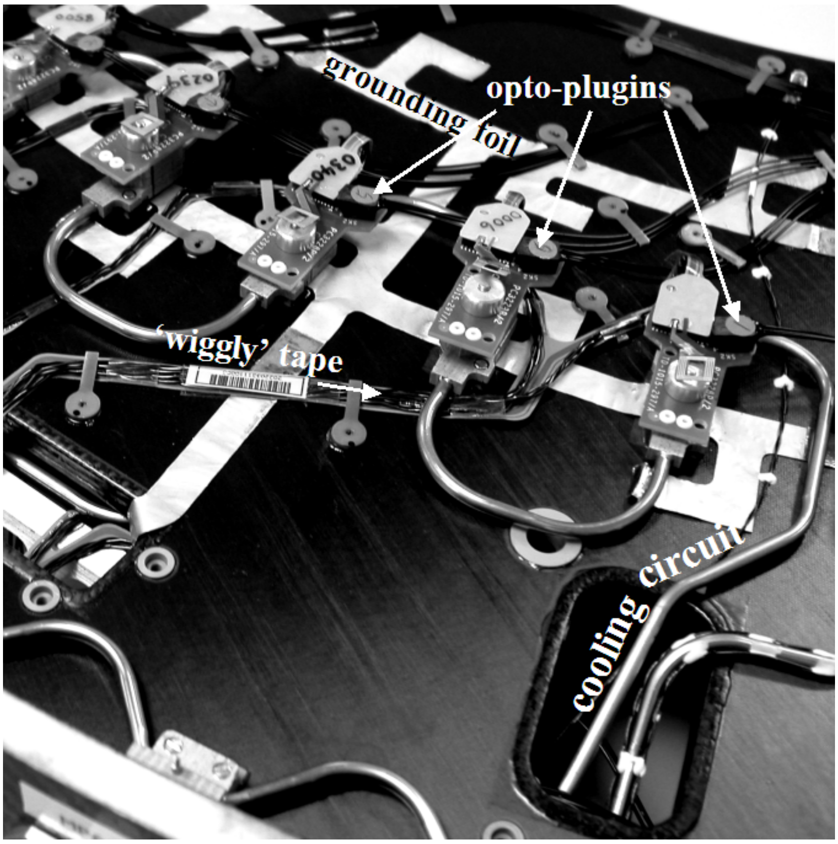

Figure 3.16: Photograph of part of an SCT disk that illustrates various services on the disk. In this photograph the modules were temporarily replaced by 'dummy' hybrids.

are placed over the cylinder surface.

On-disk: wiggly tapes

Power tapes on the disks provide the connection between the SCT modules and the patch panels at the outer edge of the disks, where they connect to the power tapes on the cylinder. The complicated routing of the power tapes over the disk surface led to the design of the 'wiggly' tapes. The wiggly tapes are constructed using double sided Kapton tapes, with copper traces on the tapes to form the power lines. One wiggly tape incorporates the power lines of up three modules and contains connectors for each module that are connected at the hybrid. The V_{dd} and V_{cc} lines could not be implemented as traces on the tapes, as the required traces for the high current on these lines would be too wide to fit on the tape. Instead the V_{dd} and V_{cc} lines are incorporated by a separate pair of copper-clad aluminum wires that are attached on top of the tape.

Voltage name	Electronic circuit	Nominal voltage (V)	Nominal (max) current (mA)
Analog V_{cc}	ABCD3T	3.5 ± 0.2	900 (1300)
Digital V_{dd}	ABCD3T DORIC4A VDC	4.0 ± 0.2	570 (1050)
VCSEL control voltage V_{vcsel}	VDC	1.6-6.6	3.5 (5.3)
V_{pin}	*p*-*i*-*n*-diode	6.0	-0.4 (-0.42)
RESET	HIGH/LOW	Vdd/-0.7	-0.4 (-0.42)
SELECT	HIGH/LOW	Vdd/-0.7	1.3 (1.4)
Current source	NTC thermistor	V_{max}=8V	0.08
Sensor bias V_{bias}	sensor	150 (Vmax=500)	0.001 (0.5)

Table 3.4: Power supply voltages required to operate each SCT end-cap module.

On-cylinder: LMTs

Low Mass Tapes (LMTs) are extra wide (21 mm) polyimide power tapes with copper traces. The widths of the traces were optimized to reduce the heat load in the available surface. The traces used for the high current lines (V_{dd} and V_{cc}) are 4.5 mm wide, while 0.5 mm wide traces are used for the other lines.

LMTs connecting to modules in the same ϕ-segment of the disks are occupying the same surface position on the cylinder and are stacked together. When powered, the heat in the center of a stack of LMTs can rise to 50° Celsius [37], which leads to a significant heat load to the detector. In order to transport this heat away from the detector, dedicated cooling pipes are placed along side the LMTs, with foils wrapped around the LMTs and the cooling pipes to create sufficient thermal contact between the two components.

3.5.2 Optical fibers

The communication between the SCT modules and the off-detector data acquisition system is made using optical signals. The advantage of optical fibers compared to electric cables is that they have smaller dimensions and a lower mass which helps to minimize the material budget. Also, unlike electric signals, optical signals are immune to electromagnetic interference and cross-talk.

Three optical connections ('links') are used for each SCT module. Two optical links are used to return the data from each side of the module, and one link is used to receive clock-and-command signals. Conversion between optical and electrical signals take place by components inside a *opto-plugin*, that connect the module hybrid to the optical fibers routed along the disk surface. Fiber ribbons carry the optical signals along the length of the cylinder and terminate at the far-end of the end-cap where they the connect with the ∼90 meter long fiber cables that send the optical signals to the off-detector read-out system. The opto-electronic components and the performance of the optical communication system will be discussed in detail in chapter 4.

3.5.3 Cooling

The SCT end-cap requires a cooling system to keep the silicon sensors at a low temperature and to remove the heat produced in the readout electronics.
Upper limits on the heat loads of the different heat sources in the SCT end-cap are listed in table 3.5 indicating a total heat lead of approximately 11 kW per end-cap, after maximum irradiation of the sensors[8].

Silicon Sensor	0.5 W per sensor	$2.9 \cdot 10^3$ W
Electronics hybrid	7.2 W per module	$7.1 \cdot 10^3$ W
Power tapes	1.0 W per module	$1.0 \cdot 10^3$ W
Total		$11.0 \cdot 10^3$ W

Table 3.5: Maximum estimated heat loads in one SCT end-cap.

The inner detector cooling system [38] uses an evaporative cooling scheme, which offers several benefits. Using the latent heat of vaporization, rather than a liquid-specific heat capacity, gives a larger cooling capacity relative to the volume of cooling system, so both the size of the system and the coolant mass flows can be reduced. Another advantage of evaporative cooling is the smaller difference in temperatures along the cooling lines, which allows one circuit to cool down up to 13 modules in series.

The cooling system uses C_3F_8 as a cooling fluid, which was chosen for its high stability under radiation exposure. Throughout the cooling process the C_3F_8 fluid follows a thermal cycle as is indicated in the phase diagram in figure 3.17.

The cooling cycle goes through the following steps: The cooling fluid is compressed (A-B) in a set of oil-free compressors, which prevents contamination of the C_3F_8. The fluid is condensed (B-D) through thermal contact with

[8]The leakage current in the silicon sensors increases due to radiation damage, leading to a higher heat load for the sensor.

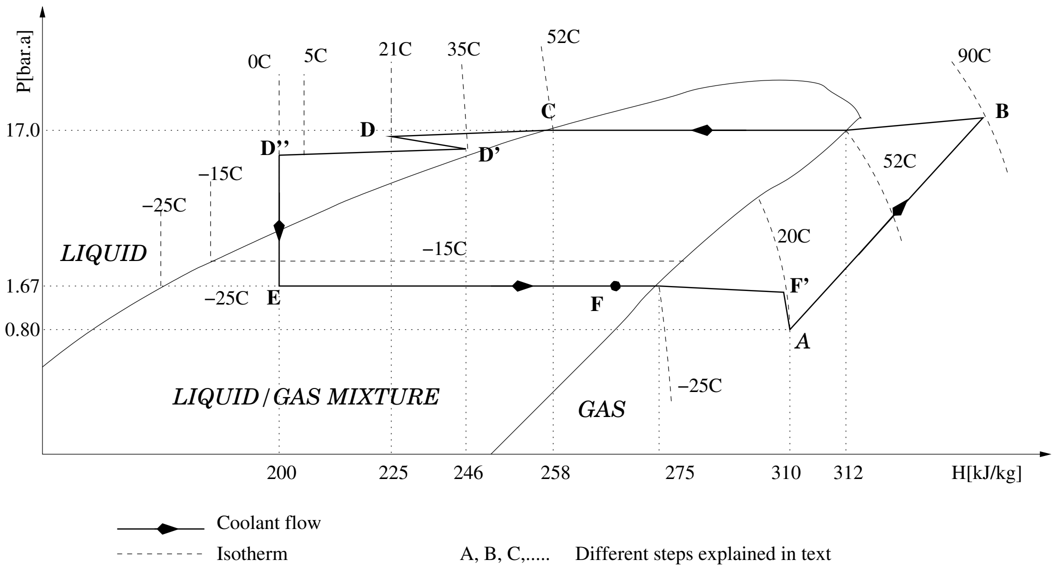

Figure 3.17: Coolant circulation of the ATLAS ID evaporative system presented on the diagram of the saturation properties of C_3F_8 [39].

the CERN cooling water and is subsequently sub-cooled (D'-D") on arrival at the detector. During the transport from the compressor to the SCT detector the cooling liquid could heat up (D-D'), due to the presence of heat-producing power cables[9]. The (cold) cooling liquid is routed through capillaries at the inlets of the SCT end-cap in which the fluid expands (D"-E). The fluid then remains in boiling condition along the cooling circuit that is in thermal contact with the detector modules to provide evaporative cooling to the modules (E-F). In the final step, before the coolant returns to the compressor, heaters located at the cooling exhaust pipes heat the coolant (F-F') to ensure that any remaining liquid is evaporated and that the temperature of the C_3F_8 return lines is above the ATLAS cavern dew-point.

The sub-cooling takes place using heat exchangers that exchange heat between the (warm) cooling liquid at the detector inlets and the (cold) cooling gas/liquid mixture at the outlets. This lowers the temperature of the C_3F_8 liquid before the coolant enters the boiling phase, increasing the efficiency of the thermal cycle. The heat exchangers are placed directly before the heaters.

The temperature of the cooling liquid in the detector structures is regulated by setting the boiling pressure of the fluid using the back pressure regulators located at the end of the return tubes of the cooling station. From the C_3F_8 phase diagram in figure 3.17 it can be seen that a back pressure of 1.67 bar absolute results in the required coolant temperature of -25°C.

[9]The heating of the cooling liquid to 35° Celsius is a worst case scenario, most likely the temperature of the cooling liquid remains below this.

Module cooling

The modules are cooled through the thermal contact with the cooling pipes in which C_3F_8 liquid is evaporating. The thermal contact is made via two carbon-carbon cooling blocks that are connected to each cooling pipe. One cooling block carries away the heat of the hybrid and the nearby silicon sensors, while the second cooling block cools down the far-end silicon sensors. The inner modules do not have the second cooling block, since they have a shorter silicon surface one cooling block provides sufficient cooling for the entire module.

One cooling circuit is connected to the cooling blocks of 10 or 13 modules and corresponds to one quadrant in one ring of modules. The cooling circuits are placed on the disk surface and are shaped with a series of bends that provide stress-relief during temperature changes.

Separate capillaries carry the coolant to each cooling circuit inlet. The exhausts from the circuits in one disk quadrant merge at the disk periphery, so that all inner, middle and outer modules in one disk quadrant rely on a single cooling line outlet.

LMT cooling

As mentioned before, the power tapes on the cylinder are stacked together and require cooling to reduce the temperature inside the LMT stacks. Dedicated cooling pipes which are fed from the module evaporative cooling circuit are used for the LMT cooling. The pipes are fed from the cooling circuits of disk 7,8 and 9, which have additional capacity for cooling the LMTs as they contain less module rings. Each set of three LMT stacks has a pipe on either side: one from disk 9 and one from disk 7 or 8. In case of failure of the cooling circuit on one these disks, the LMTs are still cooled by the cooling circuit from another disk, preventing the loss of a full azimuthal slice of modules.

3.6 Material in the detector

To limit multiple scattering, material in the inner detector is required to be minimized. Understanding the amount of material that is present in the detector helps to determine appropriate corrections to the track parameter propagation, which ultimately helps to improve the tracking resolution. For this reason, the material distribution in the SCT end-cap was required to be understood at the level of 1%.

Most material in the SCT end-cap is not a result of the silicon detectors themselves but from the services that are required to power, support, cool and read-out the modules. A record was kept of the material in the SCT end-cap by systematically weighing the different components added to the system during the construction of the detector. However the addition of, for example, extra sealant or additional fastening materials inevitably reduced the exact knowledge of the material. Weighing the completed disks with services resulted in a value that was 1.4% higher than estimated [36].

Using the information of the material distribution from this weight measurements, a simulation was made of the average radiation lengths added by the SCT end-cap in different η-regions of the detector. The distribution of the radiation lengths from this simulation is shown in figure 3.18.

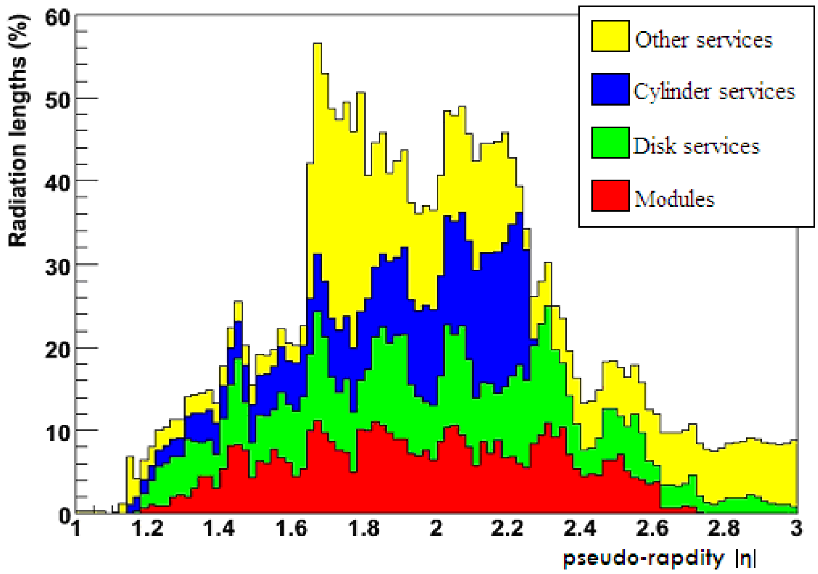

Figure 3.18: Percentage of radiation lengths crossed by a particle coming from the origin and traversing the SCT end-cap [36].

Note that it contains the radiation lengths for the SCT end-cap only, thus excluding material of the beam-pipe and pixel detector that a particle would traverse before entering the end-cap. The "other services" mentioned in figure 3.18 refer to the thermal enclosures, the cylinder support and the services in the ATLAS cavern that connect the end-cap with the off-detector systems. A steep increase in the radiation lengths is seen for values of $|\eta|$ between 1.6 and 2.3, which corresponds to particles passing the surface at the far-end of the end-cap cylinder, where the connections with the off-detector services take place. A large fraction of the services and structural material are outside the silicon detection layers, therefore deteriorating the calorimeter resolution but not the tracking performance. The material budget of the SCT end-cap is significantly more than the original requirement of maximum 10% radiation length, but this proved to be unavoidable in the light of other requirements such as mechanical stability, on-detector read-out and thermal performance.

The estimation of the material distribution in the SCT end-caps is used, together with the information from all the other ATLAS detector components, to provide realistic event simulation and to make material maps used by the track reconstruction software (see chapter 6).

Chapter 4

Optical communication for the SCT

The communication between each SCT module and the data acquisition system is made via an optical system [40]. This chapter describes the architecture of this system as is used by the ATLAS SCT, and the opto-electronic components used in the system. The optical performance of the SCT end-cap as measured at various stages of the SCT end-cap construction will be discussed. In addition the typical problems with the optical components discovered during the testing of the SCT end-cap are discussed in detail.

4.1 Opto-electronic components

Each SCT module is connected to the read-out system using three individual optical links: one link to receive the clock and command signals and two links to return the data of the module to the data acquisition. The conversion from electronic to optical signals is done using Vertical Cavity Surface Emitting Lasers (VCSELs), while the conversion from optical to electronic signals is done using photo-sensitive *p-i-n* diodes [40].

One SCT module requires two VCSELs and one p-i-n diode on the detector-side and one VCSEL and two p-i-n diodes on the data acquisition side of the system. The on-detector opto-electronics are placed in an opto-plugin that connects to each module, while the off-detector opto-electronics are integrated in the electronics of the data acquisition system.

The opto-electronic components are coupled to Step Index Multi-Mode (SIMM) fibers [41] to send the optical signals from and to the detector. The fibers are composed of fiber harnesses on the disks, fiber ribbons on the cylinder and ~80 meter long fiber cables between the detector and the off-detector read-out systems. The connections between the different fibers are made at patch panels on the disk periphery and the far-side of the SCT end-cap.

4.1.1 Conversion from electronic to optical: VCSEL

The Vertical Cavity Surface Emitting Laser (VCSEL) [42] is a type of semiconductor laser diode that emits laser light perpendicular from the surface of the structure.

The basis of any laser is to force photons to pass many times through a gain medium by trapping them inside a highly reflective optical cavity. The process of stimulated emission creates new photons with the same phase, frequency, polarization and direction of travel as the original photon. This means that light trapped inside the optical cavity is effectively amplified. The energy for the creation of the new photons comes from the recombination of electron-hole pairs that are pumped into the gain region by a drive current applied to the VCSEL. The laser components as implemented in the VCSEL[1] used in the ATLAS SCT are shown in figure 4.1.

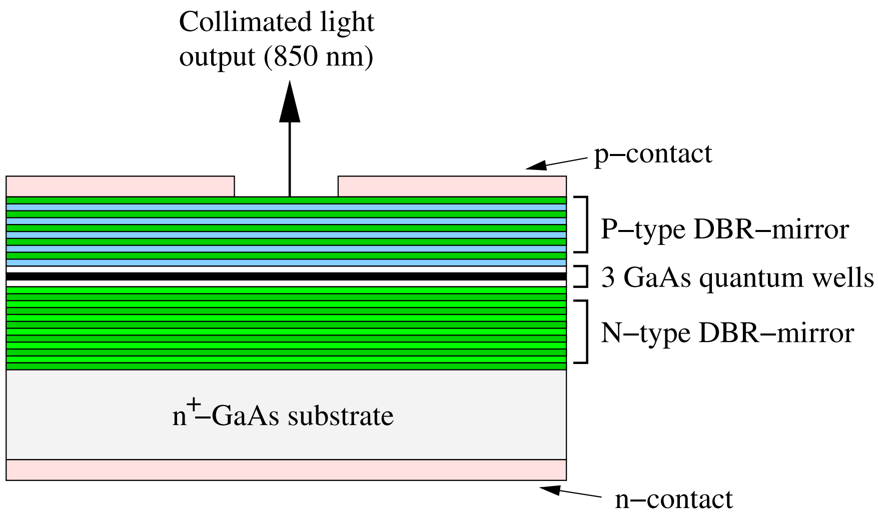

Figure 4.1: A schematic representation of the GaAs VCSEL used in the ATLAS SCT optical links.

The gain medium of the SCT VCSEL is composed of Gallium Arsenide (GaAs) which has a 'direct band-gap' [43] of 1.43 eV (865 nm). In a direct band-gap, electrons at the conduction-band minimum can combine 'directly' (without transferring momentum to the silicon lattice) with holes at the valence band maximum, and the recombination energy across the band-gap is emitted in the form of a photon of light.

The optical cavity of the VCSEL is formed using distributed Bragg reflector (DBR) mirrors. DBR-mirrors are formed with layers of alternating high and low refractive indices. Each layer boundary causes a partial reflection of an optical wave. For photons with a wavelength close to four times the thickness of

[1]VCSEL type TSD-8A12 supplied by Truelight, Taiwan.

the layers, the multiple reflections combine with constructive interference, and the layers act as high-quality reflectors. The gain region between the mirrors consist of so-called ‘quantum wells’ that confine the photons to a planar region. The VCSELs used by the SCT were designed to reflect 99% of photons inside an optical band of 850 ± 10 nm wavelength. The small amount of light ($\approx 1\%$) which passes through the top mirror forms the light output of the VCSEL.

The VCSEL forms a pn-junction by using and p- and n-doped DBR mirrors. Applying a forward electrical bias over the junction, holes are injected in the p-type[2] and electrons are injected in the n-type, so that the width of the depletion region is reduced. For a sufficiently high forward bias (1.9 Volt for an SCT VCSEL), the depletion zone eventually becomes thin enough that electrons can cross the junction into the p-type where they recombine with holes, and vice versa for holes that inject into the n-type. Although the electrons recombine with holes shortly after penetrating into the p-type, the electric current continues, as holes flow in from the opposite direction. The forward bias current is applied between the backplane and a ring shaped-electrode on the p-side, allowing the output beam to exit from the top of the structure.

The SCT VCSELs were designed to have an average coupled power into the SIMM fiber or more than 700 μW at a drive current of 10 mA. The amplitude of the drive current can be set via an external control line and can be varied from 0 to 20 mA. The rise time of the VCSEL light is maximally 120 ps, which is sufficiently fast for transmitting signals with a frequency of 40 MHz.

VCSELs are very susceptible to electro-static discharge (ESD). A small discharge through a VCSEL is sufficient to cause dislocations in the material, which can alter the behavior of the active region or mirror such that the optical cavity is destroyed and the VCSEL ceases to function. To prevent ESD damage, researchers were required to wear “ESD-safe” clothing and shoes, to prevent the build-up of static charge, while working on the assembly of the SCT end-cap.

4.1.2 Conversion from optical to electronic: p-i-n diode

The ATLAS SCT uses silicon p-i-n photo-diodes to receive the light produced by the VCSELs and convert it into an electric signal. The basis of *p-intrinsic-n* diode is the use of a junction with a lightly doped near intrinsic semiconductor region between p- and n-type material. Figure 4.2 shows the schematic lay-out of the silicon-based p-i-n diode[3] used in the ATLAS SCT end-cap.

Applying a reverse bias over the p-i-n diode sweeps out all the charge carriers and leave behind a non-conducting depletion area. Photons arriving at the p-i-n diode can produce electron-hole pairs in the depletion area. These charge-carriers are swept out of the region by the reverse bias so that a current

[2]Electrons are being removed from the p-type, leaving behind holes.
[3]Silicon p-i-n diode types Apex 10, supplied by Centronic, UK.

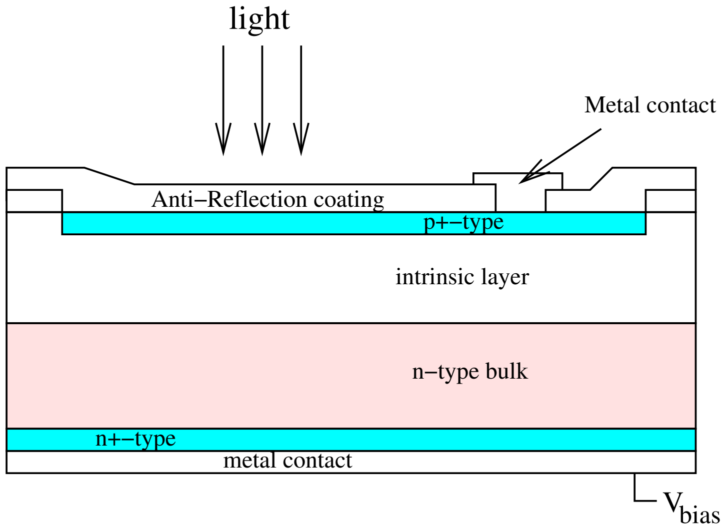

Figure 4.2: A schematic representation of the p-i-n diode used in the ATLAS SCT optical links.

is induced. The advantage of using an intrinsic layer is to create a larger depletion region with an almost constant electrical field. This increases the area where electron-hole pairs can be generated, and makes the induced current approximately proportional to the amount of light received by the diode.

ATLAS SCT uses silicon based p-i-n diodes that have an active diameter of 350 μm with an intrinsic region of $\sim$ 15 μm, chosen to be well above the average absorption length of photons with a wavelength of 850 nm, which is 10 μm. The low thickness allows the p-i-n diode to be fully depleted at relatively low reverse bias voltage (<10 V) even after receiving the expected amount of radiation damage. Radiation damage effects alter the doping concentrations in the p-i-n diode similarly as was described previously for the SCT silicon sensor (see section 3.2.4), causing the p-i-n diode response to reduce with increased radiation. The p-i-n diodes were designed to have a typical response of 0.5 A/W, before radiation damage, which is expected to reduce to $\sim$0.35 A/W, after 10 years of LHC running [44].

A minimum mean current of 30 μA is required by the chips decoding the diode output signal to correctly interpret the signal. However this minimum needs to be adjusted when taking into account the occurrence of *Single Event Upsets* (SEU). SEU is the effect where the deposition of a sufficiently large amount of energy in the electronics, for example from a α-particle or low energy proton or nucleus passing through the module hybrid, causes a bit to flip and creating a bit-error in the system.

Between the various chips and opto-electronics used in the SCT end-cap, the p-i-n diode is most sensitive to SEU effects, due to its relatively large surface diameter of 350 μm. The extra charge required to create a bit error increases with increasing value of current in the p-i-n diodes, I_{pin}. Studies made on the performance of p-i-n diode in various particle beam tests give a minimum requirement of I_{pin}=75 μA to stay below the maximum bit-error rate during high luminosity runs of the LHC [44].

4.1.3 Optical fibers

The optical signals are carried in Step Index Multi-Mode (SIMM) optical fibers[4], chosen for their radiation hardness [41]. "Step-index" indicates the refractive index profile of the optical fiber, which is used to contain the light within the core of the fiber. The profile is formed by a uniform refractive index within core of the fiber, and a cladding around the core with a much lower refractive index. The fibers are radiation hard by design as they use a pure silica core, while normal SIMM fibers have doped cores that make them more susceptible to radiation damage. Figure 4.3 illustrates the reflection of light inside the optical fiber.

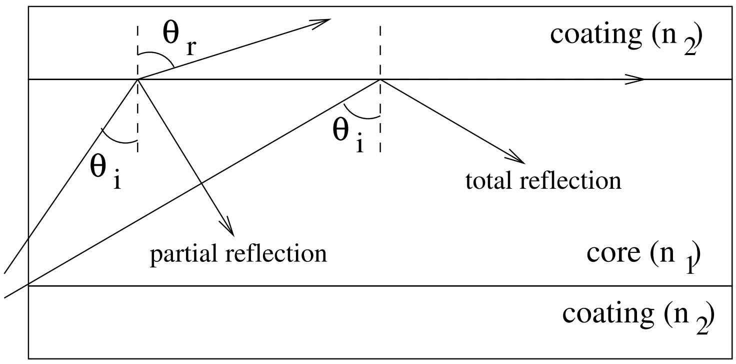

Figure 4.3: Schematic illustration of light reflecting in an optical fiber.

When a ray of light hits the transition between material with different refractive indices, part of the light is reflected at the incident angle, and part of the light enters the coating with an angle defined as the reflection angle θ_r. When θ_r becomes greater than 90°, all the light is continuously reflected back into the core, and the optical signal can propagate along the fiber. The maximum incident angle at the fiber, θ_{max}, for which light is propagated along the fiber is given by:

$$n \sin(\theta_{max}) = \sqrt{n_1^2 - n_2^2}, \tag{4.1}$$

where n is the refractive index of the medium from which the light enters the fiber. By using a much lower refractive index in the coating (n_2) relative

[4]Supplied by Fujikura, Japan.

to the core material (n_1), the light can be contained in the fiber core over a large range of incident angles. For the optical fibers used in ATLAS $\sqrt{n_1^2 - n_2^2}$ (defined as the 'numerical aperture' of the fiber) is 0.200 ± 0.015.

Absorption and scattering of the light in the optical fiber leads to some loss of light along the fiber length. The light loss in the fibers was measured to be less than 15 dB/km, corresponding to ~1.2 dB loss in the 80 meter fibers that connect the SCT end-cap with the off-detector electronics. Taking into account additional loss in the optical connector (≈ 0.5 dB per connector) and some margin for unexpected losses a minimum excess power in the range 6-8 dB is required from the VCSELs [40].

Any small light leak from the fibers onto the silicon sensors can lead to significant excess noise in the detector, as photons with a wavelength of around 850 nm have a high probability to produce electron-hole pairs in the silicon sensors. To prevent any light leakage from the fibers in the vicinity of the sensor, the fibers are wrapped inside black tubing material that is opaque to the light from the VCSELs.

4.1.4 Signal encoding

The SCT modules need to receive two types of information in order to function properly: the 40 MHz LHC clock, in order to assign hits to specific bunch crossings, and the configuration data, that contains the module specific settings for the read-out electronics at the module hybrid.

The TTC (Trigger, Timing and Command) signals uses bi-phase mark (BPM) encoding to encode the configuration data on top of the 40 MHz bunch crossing, allowing clock and command signals to go on one fiber. The principle of BPM-encoding is illustrated in figure 4.4. The encoding represents each clock cycle as alternating 0's and 1's and for each data signal an additional transition between 0 and 1 is added. The BPM-encoded TTC signals are produced by a set of specialized chips on the DAQ-side of the system [45].

On the module the BPM signal is decoded by the DORIC[5] chip, that recovers the 40 MHz clock and passes the configuration data to the read-out chips on the module. When returning data from the module, the data is collected by two master chips and transferred to two channels on the VCSEL Driver Chip (VDC). This chip translates the signal into the drive signal that operates two VCSELs that are connected to the module via the opto-plugin. The light from the VCSELs on the modules arrive at an array of *p-i-n* diodes on the DAQ-side, where it is decoded. From there on the data can be processed for calibration tests or passed along the read-out chain for physics data taking runs.

[5] Digital Optical Receiver Integrated Circuit

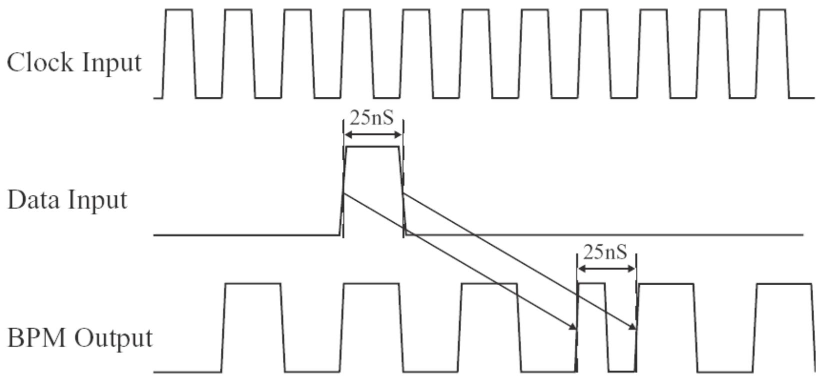

Figure 4.4: Illustration of bi-phase mark (BPM) encoding, where clock and command are combined into one data stream. The signal is delayed by three bunch-crossings. Note that without data input the BPM output corresponds to the clock input divided by two in frequency.

4.1.5 Redundancy options

During the 10 years of LHC operation, access to the inner detector will be limited and there will be very little possibility of for repairs in case of defects in the optical components at the detector-side. To prevent loss of data from a module in the case of failure of one of its optical links, redundancy options are provided: In case of a broken data link, all the data from the module can be returned through the second data link. In the case of a broken clock-and-command link, the module can receive its signals via one other SCT module using the connections that are present between the electronic hybrids of neighboring modules.

4.2 Test of the optical components on the disk

The optical fibers that are mounted on each SCT disk come in packages, so called optical harnesses, that connect to up to six SCT modules. An optical harness contains one opto-plugin for each module to connect three optical fibers to each module hybrid. Each opto-plugin houses two VCSELs and one p-i-n diode to establish the communication for that particular module.

Once the disks had been placed inside the end-cap cylinder, access to the opto-electronics on the module-side was no longer possible, and any problems in the opto-harnesses had to be solved before that. In order to detect malfunctioning opto-electronics or misplaced connections, the VCSEL power output and the p-i-n diode response were measured at various stages of the end-cap construction. These tests took place after all other disk services (power tapes, cooling circuits etc.) were in place, and just before the modules were placed on the disk.

4.2.1 Response of the p-i-n diodes

The p-i-n diode response was measured by injecting laser light on the p-i-n diode and measuring the current that was induced in the p-i-n bias supply line. A reverse bias of 5 V was applied over the p-i-n diode during the test. The laser light had a wavelength of 850 nm and fixed power output of 360 μW. The induced current on the bias line divided by the laser power was used to find the p-i-n diode response in A/W.

Figure 4.5 shows the measured response after opto-harness placement for all 988 p-i-n diodes of SCT end-cap A. The figure shows the p-i-n response measured during these test to be around 0.42 A/W. The response for p-i-n diodes measured by shining light directly on the p-i-n (no loss of lights in the harness fibers and connectors) was 0.48 A/W [46]. This means the measured value in the end-cap harness has an average loss of 0.7 dB, which is within the expected loss of the connectors and fibers of around $\sim$ 1 dB. The spread in the measured values of the p-i-n diodes response is mostly a result of the spread in the power loss for different optical fibers and connections, as the direct p-i-n diode measurements (see [46]) showed very little spread.

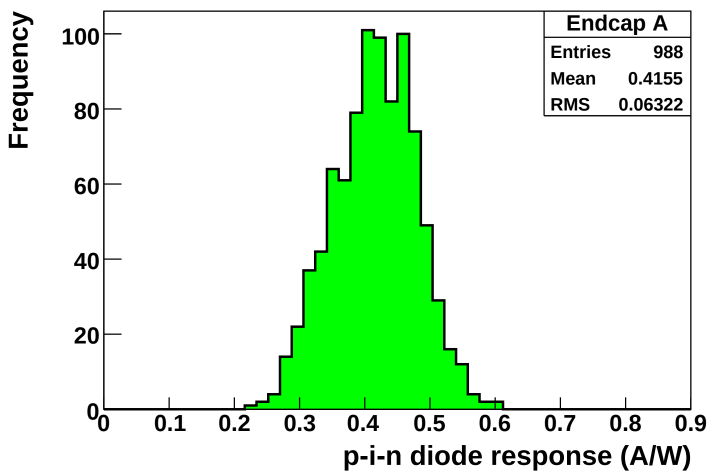

Figure 4.5: Response of the p-i-n diodes in the opto-harnesses of SCT end-cap A.

4.2.2 Power output of the VCSELs

In a real module the VCSELs are switched on and off by the driver current from the VDC chip on the modules. Since the opto-harness test was done before module placements, dummy hybrids were used that connect lines of the power tape on the disk via a 2 kΩ resistance to the VCSEL power lines in the opto-plugin. This allowed each VCSEL to be powered individually by powering one of the two VCSEL power lines. In the test a current of 10 mA was applied on each VCSEL and the light output power was measured using an large array photo-diode.

Results of the measurement for all 1976 VCSELs in the opto-plugins of SCT end-cap A are shown in figure 4.6. The figure shows an average VCSEL power output of $\approx$ 1200 μW. The spread in the power output is due to the spread in power from the VCSELs as well as the spread of the coupling efficiency into the fibers, and was observed in previous tests of the optical links [40].

Figure 4.6 shows one entry for which the power output is 0 μW. This is a VCSEL that had developed a defect[6] during placement of the services of the disks.

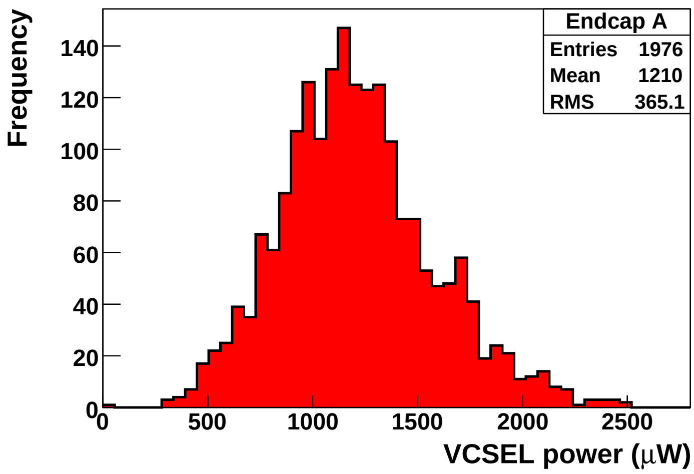

Figure 4.6: Power output of VCSELs in the opto-harnesses of SCT end-cap A.

4.3 Optical links performance of ATLAS SCT end-cap A

The final tests for the optical communication system is to test if the electronics on the SCT modules are capable of correctly interpreting the received optical signals, and that the optical signals returned by the module can be decoded by the data acquisition system.

[6]The data for the affected module can be read-out via its second link, so no readout channels were lost for this defect.

The SCT end-cap was built in successive stages, with each stage adding more components to the optical system and often blocking access to components placed in the earlier stages. Therefore, the performance of the optical links for sending and receiving streams of data had to be tested in every major construction stage, as each new fiber connection could potentially result in problems for the module read-out.
The main test stages are:

- *Modules-to-disk*: After placement of the modules on the disk, the optical read-out of all modules on the disk was tested using the on-disk services.
- *Disk-to-cylinder*: After placement of each disk in the cylinder, the optical system was re-tested, this time also using the on-cylinder services.
- *CERN reception test*: After arrival of the SCT end-cap at CERN the optical system was re-tested in case problems developed during the handling and transport of the detector.
- *Final commissioning*: After placing the SCT end-cap in its designated position in the ATLAS cavern, the SCT end-cap was tested with its final services, including the $\sim$80 m long fiber cables.

The next sections describe how the optimum configuration settings for the optical links were determined at each test stage.

4.3.1 Optical calibration settings

The read-out of the modules is facilitated by the *SctRodDaq* software application that is designed to provide an interface between the off-detector readout hardware and the data acquisition system [47] within ATLAS. The software has been designed to send the configurations to the modules and to collect the returning data. The software also provides several calibration scans designed to find the optimum optical settings for the module.

Stable communication requires that the optical clock-and-command signal induces sufficient current on the p-i-n diode at the module, and that the optical signal received from each of the two VCSELs of the SCT module is interpreted correctly. In order to optimize the communication for each module, the DAQ-software can adjust three settings:

- *Laser current (clock-and-command)*: The value of the laser current for the VCSEL arrays on the DAQ-side can be adjusted to optimize the optical power used for the clock-and-command signals. The laser current can be adjusted in 256 steps, in a range between 1 to 18 μA.
- *Delay time (data)* The delay time of data signal determines when to discriminate the received signal. The delay time can be adjusted in 25

steps of 1ns each. It is used to set the sampling point for the received optical signal as far away from the clock-edge as possible.

- *Threshold current (data)* The value of the threshold current determines where to discriminate the current induced by the data signal on the p-i-n diode arrays on the DAQ-side. The threshold current can be adjusted in 256 steps in a range between 0 to 255 μA.

The optical settings for all modules typically had to be optimized at the start of every test stage, as it implied using different fiber lengths and new connections. Once the right optical settings are found, each module can be configured by sending the configuration data to the module. Apart from changing the DAQ-related settings, optimizing the optical communication sometimes required adjustment of the bias voltage applied to the VCSELs, as is explained in the later sections.

4.3.2 Clock-and-command links

The clock-and-command links represent the optical fibers and opto-electronics that send clock-and-command data to the module. In order for the clock-and-command links to function correctly, the p-i-n diode at the module needs to produce sufficient current to allow the module electronics to decode the diode output signal. The settings that can be optimized to achieve this are the current settings of the VCSEL on the DAQ-side and the bias voltage of the p-i-n diode at the module.

The p-i-n diodes were designed to be operated with a bias voltage of 6 Volt. The responsitivity of the p-i-n diode is nearly constant for values of the bias voltage above 4 Volt [46] so the default value of the bias voltage almost never had to be changed to optimize the performance of the clock-and-command links.

The required power output of the VCSEL on the DAQ-side depends on the light losses along the optical fiber path and the sensitivity of the p-i-n diode on the detector-side. The power output is determined by the configuration of the laser current.

Optimizing the laser current

The optimum laser current for driving the VCSELs on the DAQ-side was determined for all modules in the different test stages in order to establish stable communication with the SCT module. When the optical power received at the p-i-n diode is too high, too much current is induced which effectively saturates the diode so the signal can not be discriminated any longer. When the intensity of the light is too low, the current produced by the p-i-n diode is not sufficient to drive the DORIC chip that interprets the signals.

For each module there is a range of values of the laser current for which the module correctly interprets its clock-and-command data, allowing the module to be configured. When the module is correctly configured, it returns a fixed data bit-stream, which can be used as an indication that the correct setting has been found.

The optimum value of the laser current is determined using a scan in the DAQ-software that monitors the data returned by the module at different settings of the laser current. The scan results in two histograms per module, which correspond to the two data links of each module. Figure 4.7 shows an example of the current scan result of one data link. The histogram is a 2D-projection of a 3D histogram, with on the x-axis the time (in bins of 25 ns) and on the y-axis the laser current. The shade of gray in the histogram represents the fraction of triggers interpreted as '1'. For example when all triggers return 1 a dark gray entry is added to the histogram and for all triggers returning 0 a white entry. In the example in figure 4.7, the module was correctly configured at laser current setting of f ≈ '110' (6.5 mA) and above, as the fixed data bit-stream becomes clearly visible above this value.

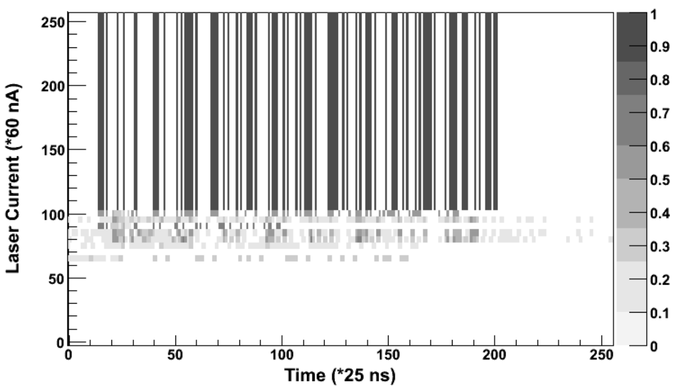

Figure 4.7: Example of a graphical display showing a typical current scan result from one data link of a SCT end-cap module.

For most modules it has been found that the laser current is optimized at a default setting of "160", corresponding to a current value of ≈ 10 mA.

4.3.3 Data links

The data links represent the optical fibers and opto-electronics that send the data from the module as binary output signal to the data acquisition system. In order for the data links to function correctly, the light sent from the VCSELs at the detector-side needs to induce sufficient current when arriving at the p-i-n diode at the DAQ-side. The p-i-n diodes that receive the optical data signal from the modules use two main settings in the software: the delay time determines the time when the signal is discriminated and the threshold current discriminates the signal at the DAQ-side. The optimum values for the threshold current and the delay-time were determined using the techniques explained in the next sections.

The light output from the VCSELs on the modules can be tuned by changing the VCSEL bias voltage on the module power supply line. The default value for the VCSEL voltage is 4.5 V but some data links required a deviation from this value based on the result of the threshold current scan.

Optimizing the threshold current

The photo-diodes at the DAQ-side measure the light returned by the VCSELs at the modules, and interpret the data as 0's or 1's depending on the induced current being below or above the setting of the threshold current. Each of the two data links for every module has a setting for the threshold current.

The induced current in the p-i-n diode has a slow fall-off behavior, so that a small amount of current remains present in the photo-diode several time-bins after light was received. The threshold current should be configured such that it is well above the fall-off current and well below the maximum current that is induced by the incoming light.

The optimum threshold current can be determined by measuring the trigger occupancy over the range of settings for the threshold current. During this scan the chips are set to return the data of their configuration register, which results in a fixed pattern of optical 0's and 1's. Figure 4.8 shows a typical example of the output of such an threshold scan, indicating the minimum and maximum current setting, between which the data stream is interpreted correctly. The figure shows that for an threshold setting below the indicated minimum, the signal is sometimes interpreted as '1' when it should be '0', which is caused by the slow fall-off of the p-i-n diode signal. In order to prevent misinterpreting the optical signals the optimum value for the threshold should be set above this 'noise' and below the maximum threshold setting.

The light-output of the VCSEL can vary slightly over time, so the optimum threshold for which the module works reliably needs to have a sufficient margin from the minimum and maximum threshold values. The optimum setting is defined at 70% between the minimum and maximum threshold, as this proved to be a reliable setting for most modules.

The threshold scans were used to find a variety of problems on the optical return lines as is discussed in detail in section 4.3.4.

Optimizing the discrimination time

The delay time determines the time at which the light received by the p-i-n diode on the DAQ-side is discriminated. The delay time should be chosen such that the sampling-point is set far away from the clock-edge. The clock-edge

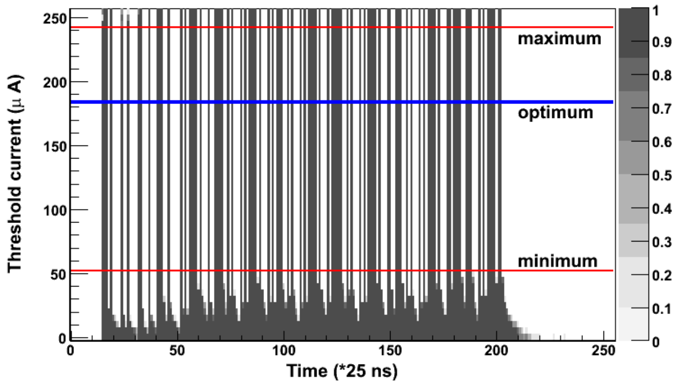

Figure 4.8: Example of the graphical display showing the threshold scan results for one data link of an SCT module, with indications to the minimum, maximum and best threshold setting.

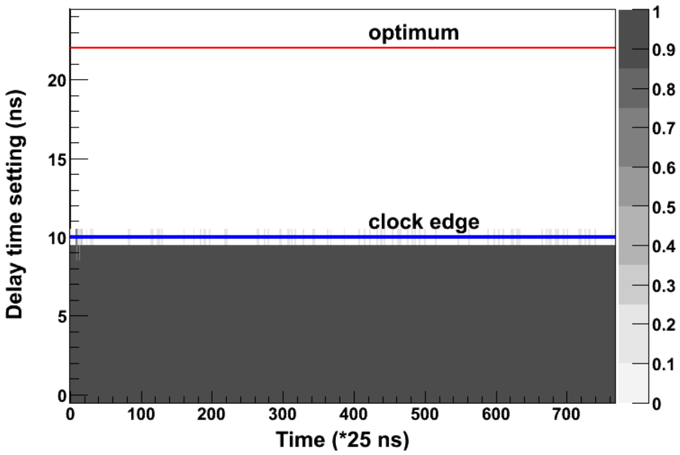

Figure 4.9: Example of the graphical display showing the delay time scan result of one data link.

corresponds to the transition between the optical 0 and 1, and sampling the signal at or around this transition results in bit-errors.

The optimum setting for the delay time depends on the length of the fibers, and as a result is different between different modules and in the different test stages. The best setting for the delay time is determined by changing the value of the delay time between 0 and 24 ns in steps of 1 ns, and measuring the trigger occupancy over time. During this test the module chips are set to return a data signal corresponding to the clock signal divided by two, while the read-out system is set to sample at half frequency. This is done so that depending on the setting of delay time the fraction of measured triggers is either 0 or 1.

An example of the result of the delay test is illustrated in figure 4.9, which also gives an indication to the delay time where the transition between 0's and 1's takes place. The delay time corresponding to this transition point indicates the clock edge, where the light pattern is most likely to be misinterpreted. The optimum value of the delay time is chosen as far away from the clock-edge as possible, so the delay time is defined at 12.5 ns from the measured clock transition point.

Interdependency of the threshold and delay settings

Experience from assembly tests done for the entire SCT, barrel and end-caps, showed that the optimum threshold value depends on the chosen setting for the delay time (and vice versa). In order to optimize both settings simultaneously, a two-dimensional test was developed. In this test the trigger occupancy is measured while varying both the threshold current and the delay time setting in a single scan.
An example of the result of this test is given in figure 4.10. The trigger occupancy indicated by the gray-scale now corresponds to the *average trigger occupancy*, which is equal to 0.5 when the correct data pattern is interpreted.

Using the result of the 2-dimension scan, the clock edge can be determined from the delay value with the lowest maximum threshold (at 2 ns in figure 4.10). As before, the optimum delay value is chosen to be 12.5 ns after the clock edge. The minimum and maximum threshold values that correspond to a trigger occupancy of 0.5 are determined at the optimum delay value, and as before the optimum threshold is at 70% between this minimum and maximum.

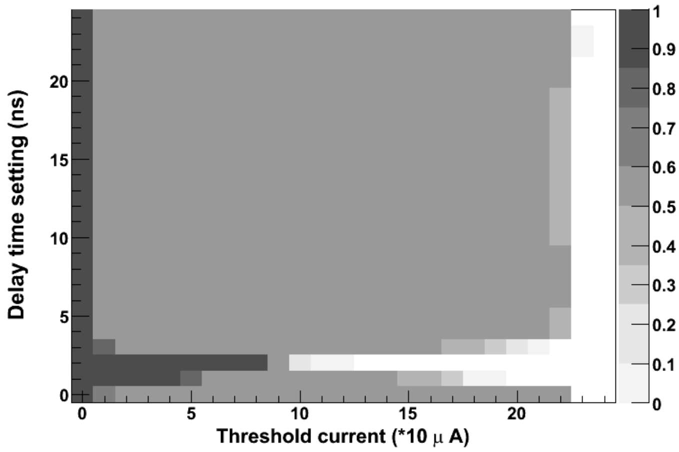

Figure 4.10: Example of the graphical display showing the average trigger occupancy (gray-scale) as a function of the delay setting and the threshold current for one optical link.

The two-dimensional scan was particularly useful for testing the optical links when no module cooling was available; the scan can find the optimized settings within ∼ 7 seconds after powering the modules, allowing the modules to be powered off before overheating. Particular problems in the optical return signal, such as "slow turn-on" discussed in the next section, can not be found with the two-dimensional scan, so that threshold scan remained a necessary tool for finding all problems with the data links.

4.3.4 Optical problems summary

A variety of optical problems was found while testing the optical communication of SCT end-cap A. One module has no p-i-n diode response and is permanently configured to receive its clock-and-command data via the neighboring module. Another 12 modules have so-called 'dead' VCSELs (when light from one of the data links does not arrive at the DAQ-side) and can only return the data using the other of the two data links.

Some data link were found to be 'problematic', which meant that the links were found to work in principle, but would from time to time result in bit-errors in the optical communication. The problematic links were found to be a result of the fluctuating power output of the VCSELs over time. In particular, some data links were found to have only a small range of values for the threshold current available for which a correct data pattern was returned in the threshold test. These data links have an increased chance of creating a bit-error during fluctuations of the light output.
The main problems that lead to a data link becoming "problematic" are identified as:

- *Slow turn-on*: the light output of the module increases over time, resulting in a decreased margin of the threshold range usable of over the entire time period. See figure 4.11 for an example.
- *Low light*: the current induced on the receiving diode-arrays at the BOC is relatively low, reducing the maximum threshold setting for which the signals can be correctly discriminated. See figure 4.12 for an example.
- *High noise*: the light-output from the data link is very high so that the slow fall-off behavior of the diode-arrays dominates even at high thresholds. See figure 4.13 for an example.

Note that not all 'problematic' links are unusable, but using these links in calibration or physics runs would increase the chance for problems to occur while interpreting the optical return signals.

Sometimes a problematic link could be made to work again by varying the values of VCSEL bias voltage between 4.0 and 6.0 V (default is 4.5V) in order to increase or decrease the light output of the VCSELs. However, there is only

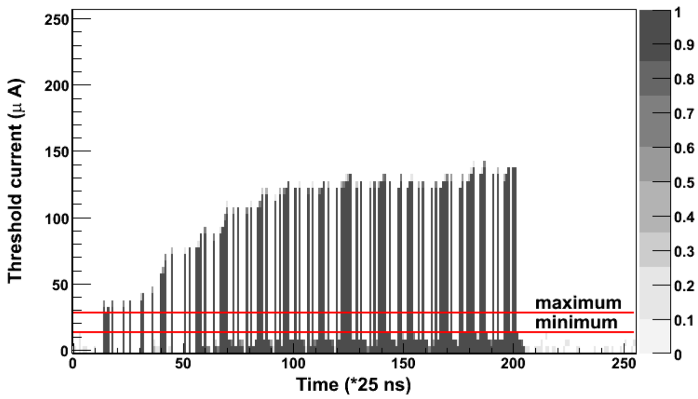

Figure 4.11: Example of a problematic data link with *slow turn-on*.

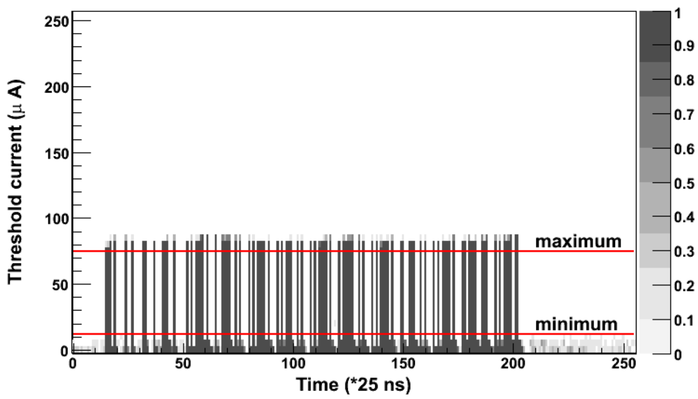

Figure 4.12: Example of a problematic data link with *low light*.

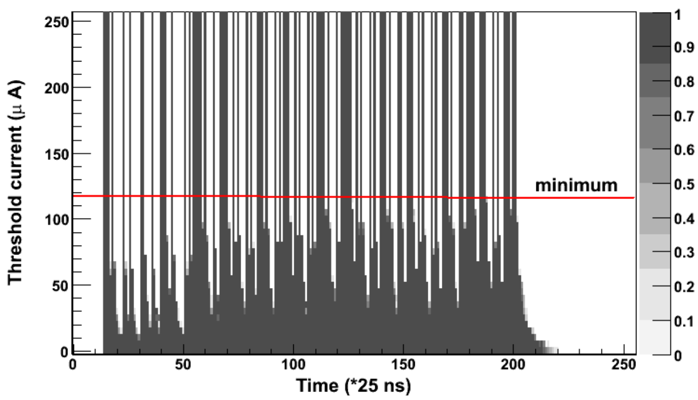

Figure 4.13: Example of a problematic data link with *high noise*.

one setting of bias voltage available for the two VCSELs connected to each module. This means that altering the VCSEL voltage to save one data link might cause problems for the second link. Figure 4.14 shows an example how the threshold scans for two data links of one module are affected using three different values of V_{VCSEL}. In this example increasing the voltage made the second data link usable, while making the first link slightly 'noisy'. A reference

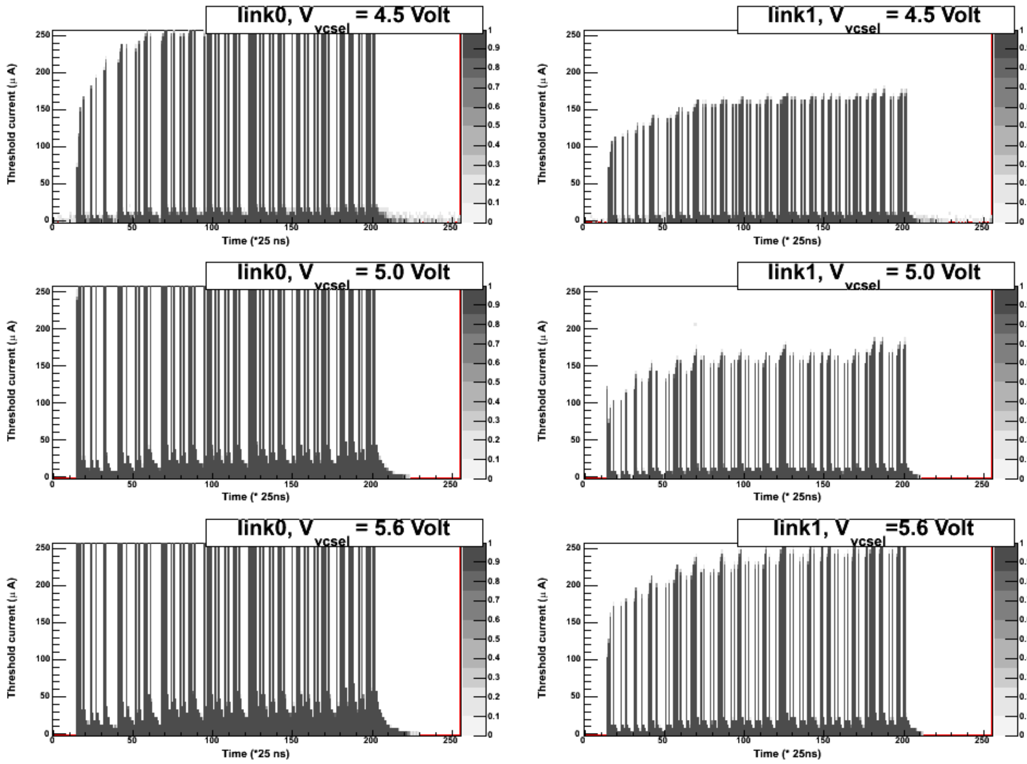

Figure 4.14: Example of the resulting threshold scans for one module at three different values of V_{VCSEL}, with link0 on the left and link1 on the right hand side.

table for all optical problems found in SCT end-cap A is given in appendix A.

During the first optical tests of disk 1A, a large number of optical problems was found. As a consequence, two optical harnesses, corresponding to a total of 9 SCT modules, were replaced on disk 1A which reduced the number of optical problems. However, not all optical problems could be solved by replacing optical harnesses due to the limited number of available spare harnesses and the possible danger of removing modules and services on the disk in order to reach the optical harness. Instead, the remaining problems are circumvented by using the redundancy of the system. In the end no read-out channels were lost due to optical communication problems.

4.4 Conclusion

The tests of the performance of the optical communication system of ATLAS SCT end-cap A have shown that communication can be established with all 988 SCT end-cap modules. Most modules have both data links functioning properly. This means that in the case of future problems the redundancy of the system can still be utilized. A total of 12 modules have only one of their two data links working. The data for these modules can be retrieved by the remaining link, so that no channels are lost as a result. One module had a problem with the on-detector p-i-n diode but it can still be configured by receiving its clock-and-command signals via a neighboring module.

A concern for future data-taking is the instability of the optical communication for a few modules with 'problematic' data links. The optical performance tests show that problematic data links have a smaller range of workable settings available, which sometimes leads to bit-errors during fluctuations of the light output. These links can function, but they need frequent maintenance to re-optimize their settings over time.

Chapter 5

SCT module performance

This chapter describes the module performance tests that were done at various stages during the assembly of SCT end-cap A. This includes tests of the sensor current behavior, the digital and analog functionalities of the SCT module read-out chips and the equivalent noise charge on the silicon strips.
The test results show that the modules of the SCT end-cap A perform well within their requirements. All the test results are documented and remain an important reference for the module performance during the lifetime of the detector.

5.1 Introduction

The module performance tests that took place during the assembly of the SCT end-cap were aimed at checking the full functionality of each of the silicon detectors. These tests included measurements of:

- Sensor current: Check that the sensor behaves like a diode and can be fully depleted. The maximum allowed leakage current (before irradiation) is 6 μA at V_{bias}=150 Volt.
- Analog functionality of the module electronics: Test the read-out of the strips and ensure that at least 99% of all silicons strips can be read out and ensure that the noise on the strips agrees with the expected value for that module.
- Digital functionality of the module electronics: Check that the data is correctly stored in the digital pipeline and can be read out by the data acquisition system. In addition, the channel masking and chip bypass functionality is tested.

The SCT end-cap modules were produced at various production sites. Each site was responsible for ensuring quality of the modules before sending them to

Nikhef. This chapter focuses on the module performance as measured during the various assembly stages including the final commissioning of the SCT end-cap after installation in the ATLAS cavern.
The main test stages during the SCT end-cap assembly were:

- *Modules-to-disk*: Immediately after placement of the modules on the disk, all the modules on the disk were tested. This test stage was important to test the module functionality using the on-disk services for the first time. Problematic modules could only be replaced in this test stage as later stages did not have sufficient access to the disk

- *Disk-to-cylinder*: After placement of each disk in the cylinder, all the modules on the disk were re-tested, to find and resolve problems with the fibers and cables routed on the outside of the cylinder.

- *CERN reception test*: After arrival of the SCT end-cap at CERN all SCT modules were tested to see if any new problems developed during the handling and transport of the detector.

- *Final commissioning*: After installation in the in the ATLAS cavern, the SCT end-cap was tested to check that no problems occurred during the installation of the detector and to test the connections with the readout systems in the services caverns.

At each of these four stages the tests for the module performance (described later in this chapter) were repeated. Only during the first stage could modules that failed the performance test be replaced. Tests at later stages were aimed at finding problems with the services such as the power tapes and optical fibers and ensuring that no common mode noise was added to the system due to grounding problems.

5.2 Test set-ups

Tests of a single disk with modules were done inside a dedicated disk-test-box as shown in figure 5.1. In this box a single disk with all modules mounted to it, could be powered, cooled and operated under similar conditions as in the ATLAS experiment. The disk-test-box was closed off with a large panel during the testing to prevent ambient light from falling on the silicon sensors and to contain the dry air. Dry air was flushed through the box to keep the dew point well below the temperature of the cooling circuits, to prevent condensation on the modules.

A second (bigger) test-box, shown in figure 5.2 , could enclose the full end-cap cylinder to allow dry air to be flushed through the box while the detector was cooled. The cylinder test box was also designed to safely transport the SCT end-cap from Nikhef to CERN.

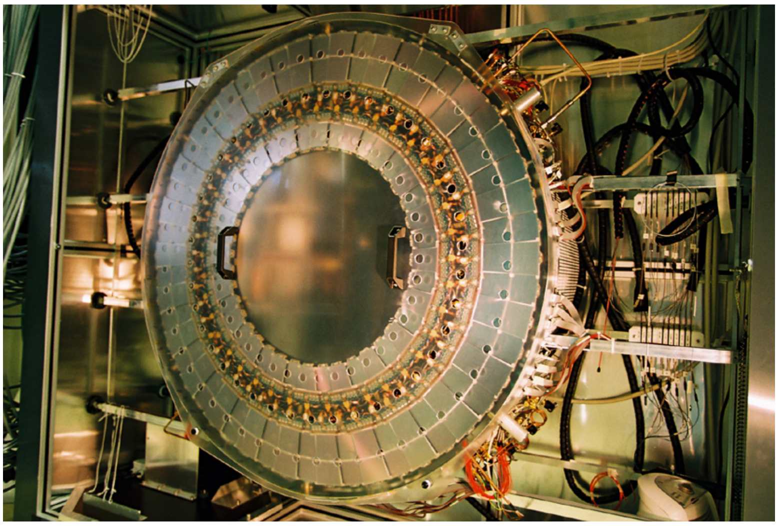

Figure 5.1: The disk test-box in the Nikhef clean-room containing one SCT end-cap disk.

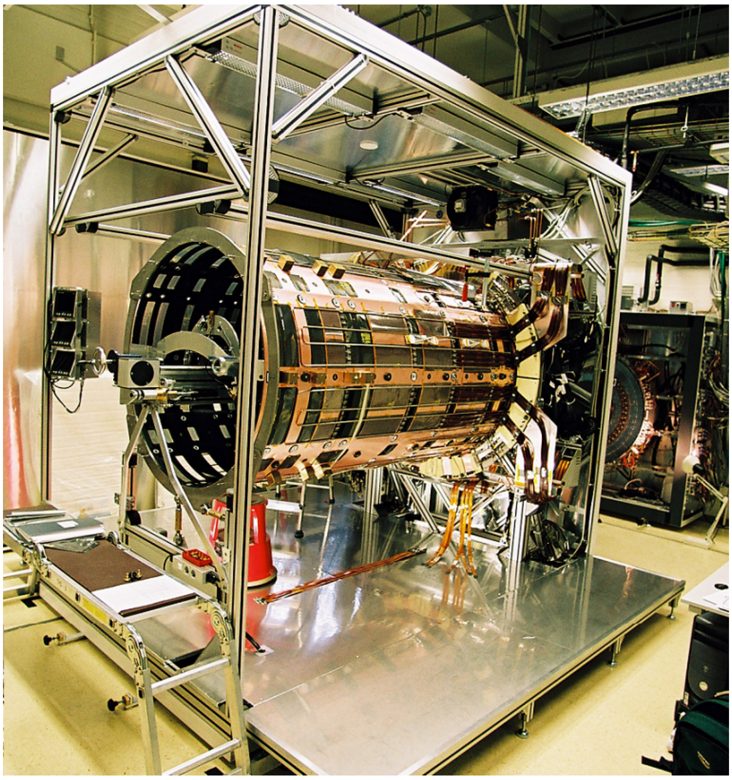

Figure 5.2: The cylinder test box in the Nikhef clean-room containing the partly assembled SCT end-cap A.

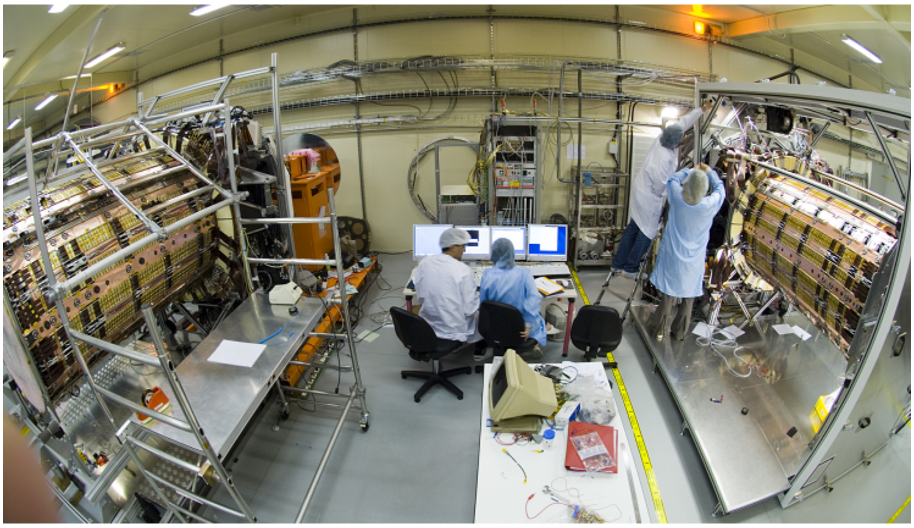

Figure 5.3: The two SCT end-caps during the CERN reception tests. The author of this thesis, can be seen on the right-hand side of the picture, as she is connecting cables to the SCT end-cap A

Upon arrival at CERN the SCT end-caps were re-tested in the clean-room of the surface reception building (SR1) at CERN (see figure 5.3). After the reception tests, the SCT end-caps were placed inside the TRT end-caps and together they were lowered into the cavern and placed in their final position on either sides of the SCT barrel.

With the SCT end-cap A in its final position in the ATLAS cavern, all the modules were re-tested with the real services that are used to operate the SCT during data-taking in ATLAS.

5.3 Sensor current

The current in the silicon sensor under the influence of a reverse bias voltage is measured to study if the silicon sensors are working correctly. As explained in 3.3, the silicon sensors in the SCT module use a reverse biased p-n junction to measure the passage of charged particles. The reverse bias voltage induces a current in the sensor which is composed of the generation current and the surface current. Generation current refers to the thermally induced charge in the depletion layer and is therefore proportional to the depletion volume which is proportional to $\sqrt{V_{bias}}$ (see equation 3.4). The surface current can be approximated by an Ohmic resistance.
This allows the measured sensor current to be expressed as a function of the

applied bias voltage, V_{bias}, and the depletion voltage of the silicon, V$_{dep}$ [48]:

$$I_{bias} = \begin{cases} A \cdot \sqrt{V_{bias}} + B \cdot V_{bias} + C & V_{bias} \leq V_{dep} \\ A \cdot \sqrt{V_{dep}} + B \cdot V_{bias} + C & V_{bias} > V_{dep} \end{cases} \tag{5.1}$$

where A, B and C are sensor-dependent constants. The first term describes the generation current contribution, the second term describes the surface current contribution and the last term accounts for the measurement offset.

The sensor behavior was studied by plotting the measured leakage current for increasing values of the sensor bias voltage to form an IV-curve for each module. It should be noted that each module uses 2 or 4 sensors, and so the leakage current measured on the modules is actually the sum of the currents from multiple sensors. Figure 5.4 shows an example of an IV-curve for one module as measured during the final commissioning of the SCT end-cap at CERN. The fit to the IV-curve in the example with equation 5.1 indicates average depletion voltage of the sensors of 73 ± 4 Volt, which agrees with the expected value for silicon sensors before irradiation (see section 3.2).

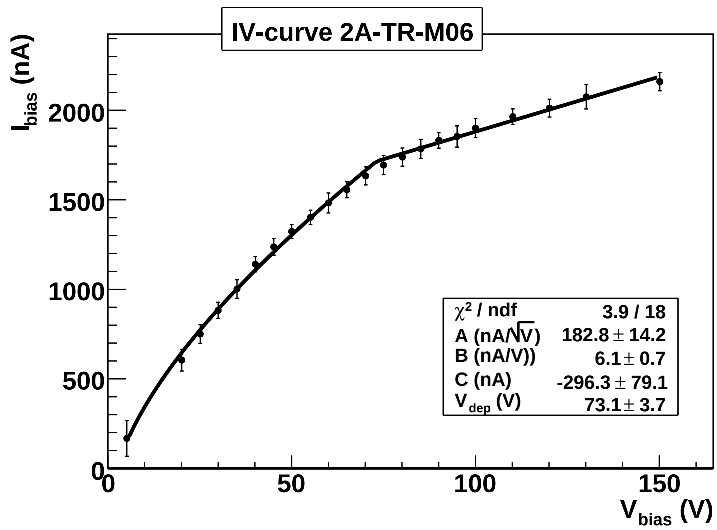

Figure 5.4: Example of an IV-curve of an SCT end-cap module as measured during the commissioning in the ATLAS cavern, showing the result of the fit with equation 5.1.

It should be noted that the IV-curve shown in figure 5.4 is not a typical example, as most of the ATLAS silicon sensors (before radiation damage) have a much lower sensor current. Due to the limited precision with which the sensor current is measured, the IV-curves could not be fitted with a reasonable enough accuracy for most modules to determine the depletion voltage.

Radiation damage to the silicon sensors will lead to a different value of the required depletion voltage, so that monitoring the depletion voltage is important to see the effect of radiation damage to the silicon sensors over time. Another method for monitoring the depletion voltage is by studying the input noise as a function of the bias voltage as is detailed in [49].

The silicon sensors had two different manufacturers: CiS and Hamamatsu, which used a slightly different design for the sensors (for details see [30]). From the tests made during production of the silicon sensors, it is known that the sensor current produced by CiS-sensors is higher than that of sensors produced by Hamamatsu.

Figure 5.5 shows the distribution of the measured sensor current at 150 V bias voltage as was measured in the final commissioning of the SCT end-cap, showing the higher average sensor current for the CiS sensors compared to the Hamamatsu sensors. Despite this effect, figure 5.5 also shows that all the modules still satisfy the requirement of having a leakage current of less than 6 μA.

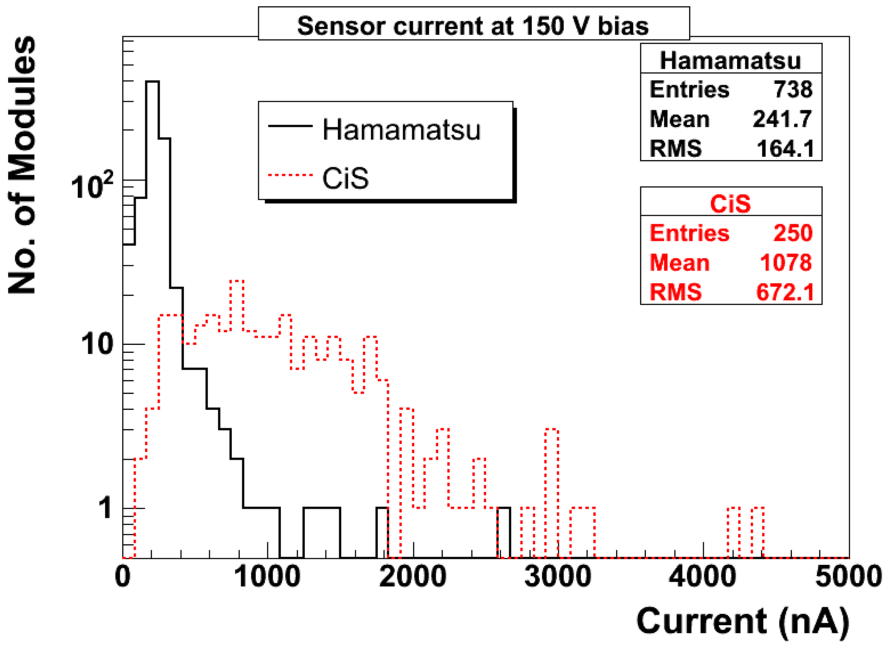

Figure 5.5: Bias current induced in the end-cap A modules with 150 V bias voltage.

Note, that this *initial* difference in sensor current has little or no impact on the module performance as the doping concentration in the sensor will be altered when the module is irradiated. Studies with irradiated modules confirm that Hammamatsu and CiS sensors will reach similar sensor currents after receiving radiation during LHC running [30].

5.4 Digital tests

The digital tests check specific functionality of the digital part of the ABCD3TA chips on the module and the ability to read out data from the module in general. All the tests are based on measuring the occupancy of each channel while varying a specific setting in the chip configuration. The correct optical settings (see chapter 4) had to be determined before the digital tests took place, as problems with the module communication would lead to failures in interpreting the triggers in the digital tests.

5.4.1 Channel masking

The readout chips of the modules apply a mask to the measured hits on all the strips. A channel that is masked always returns 0. Masking is necessary for strip channels with very high noise, as unmasked noisy channels add fake hits and increase the amount of data that has to be read-out.

In order to check the capability of the chips to mask on and off all the channels on the chips, the trigger occupancy is measured using different settings of the mask register. During the test the output is set such that any channel which is not masked returns a signal corresponding to '1'. The tests starts with a mask register where all channels are unmasked. For each consecutive mask register in the test, one more channel on each chip is masked, until all channels are masked at the final mask register. A typical example of the result of the masking test is shown in figure 5.6. The figure is a 2D projection of a 3D histogram, where the shade of gray indicates the trigger occupancy as a function of the channel number and the mask register. In this example no problems with the channels masking were found.

In the entire SCT end-cap A, a total of 9 channels were found that could not be masked off, which represents only $6{\times}10^{-4}\%$ of all channels in the SCT endcap and is neglible for the performance of the endcap. If there was a channel that needs to be masked due to high noise which also had masking defect, it would have to be masked offline, but none such channels were found on the SCT endcap A in any of the test stages.

5.4.2 Chip bypass test

When reading out the data of an SCT module, the readout chips are requested to pass their data and the data of their neighbors along to the "Master" chips so that all data from one side of the module (6 chips) can be returned via one of the two data links. The SCT module is designed with the possibility of bypassing a broken chip to reduce the loss of data in case of a chip failure.

The chip bypass functionality is tested by trying all possible combinations of bypassed chips that are set in the module configuration settings. The chips

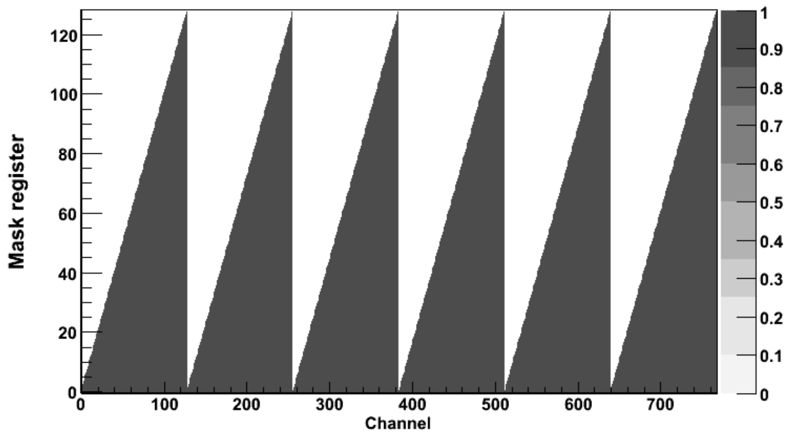

Figure 5.6: Example of the graphical display showing the result of an channel masking test of one side of an SCT end-cap module.

that are included in the module configuration are set to return signals from all their channels. Chips that are bypassed can not return any events and result in a white block (trigger occupancy = 0.) in the histogram produced by the chip bypass test. An example of the result of the chip bypass test is shown in figure 5.7, corresponding to the situation where all the possible chip bypass combinations are working correctly[1]. No problems were found for the bypass-functionality of the chips for any of the modules in SCT end-cap A.

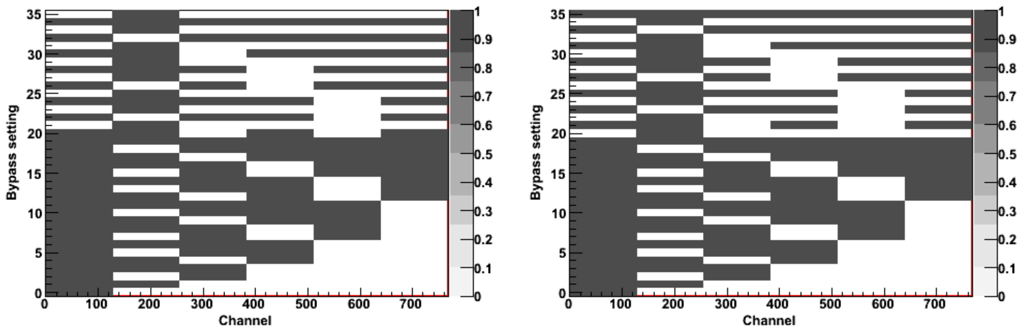

Figure 5.7: Example of the chip bypass test, where the two plots represent 6 chips on the front (left) and back (right) of one SCT module. The y-axis represents the 36 possible chip-bypass-combinations used during the scan.

[1]Note that the data is returned using a data-chain containing at least one master and one end-chip (see figure 3.12) so not all combinations of chips are possible.

5.4.3 Pipeline test

One of the most important digital functionalities of the readout chip is the ability to store information of the strip hits in the pipeline. Defects in the pipeline of one channel would result in the loss of all data measured in the corresponding strip.

Each readout-channel of the module has an associated pipeline to store the hit or no-hit information from up to 132 events, ordered in 12 cells with 11 events. During the pipeline test, the chips are configured to read-out a mask register which is loaded alternatively with all 1's and all 0's. When issuing the read-out command the chips return the data from the pipeline. When a pipeline cell returns a 0 when it should have stored a 1, its defect is listed as "Dead cell". When a pipeline cell returns 1 when it should have returned 0, its listed as a "Stuck cell". Sometimes all the pipeline cells of single channel are seen to be stuck or dead, rendering the entire channel unusable. An example of pipeline scan finding a stuck pipeline is shown in figure 5.8.

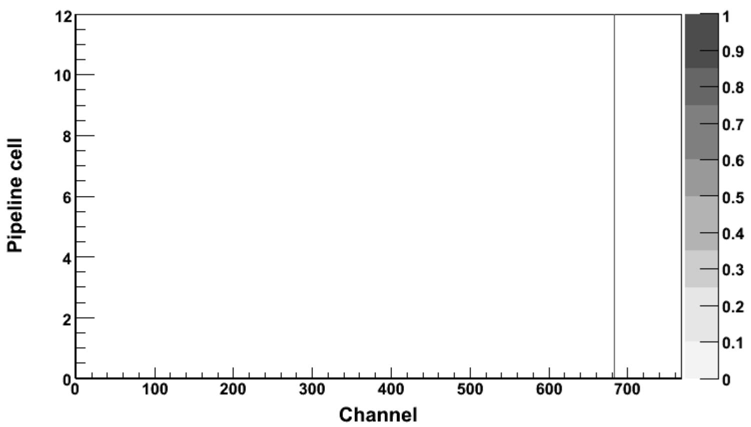

Figure 5.8: Example of the result of a pipeline scan when reading out the pipelines filled with 0's, showing one of the few pipeline defects found on SCT end-cap A. Channel 682 is seen to return 1's, instead of 0's from all 12 pipeline cells.

Since the pipeline is downstream of the masking registers in the data flow, a stuck pipeline cell cannot be masked off and will contribute to the noise occupancy of the module. The information of pipeline defects is stored and used to mask off the channels offline.
Very few pipeline defects where found in the modules during the assembly tests for SCT end-cap A, as illustrated by the total number of pipeline defects given in table 5.1.

Pipeline defect	No. of channels	% of total channels
Dead pipeline	2	1.32×10^{-4}
Dead cell	3	1.98×10^{-4}
Stuck pipeline	2	1.32×10^{-4}
Stuck cell	8	5.27×10^{-4}
All pipeline defects	15	9.88×10^{-4}

Table 5.1: Summary of pipeline defects on SCT end-cap A.

5.5 Analog tests

In the analog stage the signal induced in the strip is amplified, shaped and discriminated using a threshold setting. For data-taking the default setting of the threshold is chosen such that it corresponds to the output signal as created by an input signal equivalent to 1 fC charge induced on the strip[2]. To find the threshold corresponding to 1 fC the analog response needs to be reconstructed for each channel.

Measuring the analog response signal on the strips also allows to determine the input noise of the strips. One of the requirements of the silicon sensors is that the noise on the strips does not exceed 1800 electrons, to guarantee a noise occupancy on the silicon strips of less than $5\cdot10^{-4}$. The measurement of the input noise is also used to determine the total number of usable channels in the SCT end-cap A, which is required to be greater than 99%.

5.5.1 Reconstruction of the analog strip response

Since the SCT modules were designed with a binary read-out system, the analog channel response can not be measured directly. Instead, the analog response is reconstructed by injecting a calibration charge on the channel and measuring the corresponding occupancy over a range of threshold values. The calibration charge is produced by the charge injection circuitry of the read-out chip.

The injected charge is shaped and amplified in the analog circuitry to form an output signal. The discriminator threshold determines whether or not the output signal corresponded to hit. The probability that the injected charge produces a hit depends on the setting of the discriminator threshold. The average hit probability is measured by repeating the process of injecting charges

[2] A signal of 1 fC is well above the expected the noise, and well below the average induced charge from the passage of a charge particle, see also 3.2.4

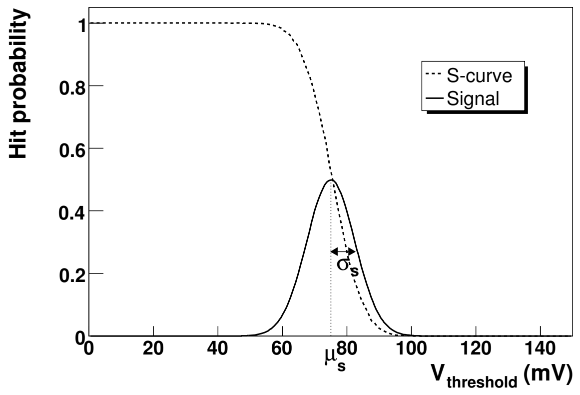

Figure 5.9: Typical example of an S-curve (dotted line) as measured on one SCT channel. The corresponding signal response shape (solid line) as a function of signal height is also indicated.

and counting the fraction of read-out triggers that produced a hit. This measurement is repeated over a range of threshold setting to produce a so-called S-curve, for which an example is shown in figure 5.9.

The S-curve represents the probability p that a channel registers a hit at certain threshold voltage V_{thr}, given by:

$$p(V_{thr}) = \int_{V_{thr}}^{\infty} f(s)ds \tag{5.2}$$

where $f(s)$ is the probability distribution function that gives the chance of measuring a signal with signal height s. The signal height distribution is assumed to be Gaussian:

$$f(s) = \frac{1}{\sigma_s\sqrt{2\pi}} e^{-(s-\mu_s)^2/2\sigma_s^2} \tag{5.3}$$

where μ_s is the mean signal height and the width of the Gaussian σ_s is the RMS noise of the signal. By fitting the S-curve the DAQ software can determine the noise σ_s.

During the analog tests, S-curves are measured for all the chip channels over a range of values for the injected charge. The threshold setting at which the probability of getting a hit is 50%, corresponding to μ_s, is defined as the V_{t50}-point. The value of the V_{t50}-point for each channel should increase linearly with the value of the injected charge, while the *output noise*, σ_s, is expected to be approximately constant as a function of charge[3].

[3]In practice, the *output noise* of each channel on the SCT module is always determined as the value of σ_s from the S-curve obtained with a 2 fC input charge.

5.5.2 Finding the optimum delay

The correct setting for the delay between the charge injection time and readout time, the so-called *strobe-delay*, has to be determined in order to measure accurate S-curves for all channels. If the strobe-delay is set too low the signal has not yet arrived and no hits are registered, while if the delay is set too high, the signal has decayed below its average threshold. Ideally the value is chosen such that the peak of the shaper response is sampled at the peak of the signal.

The strobe-delay scan helps to determine the optimum setting of the strobe-delay by measuring the fraction of triggers resulting in a hit over a range of strobe-delay settings. An example of the result of such as scan is shown in figure 5.10

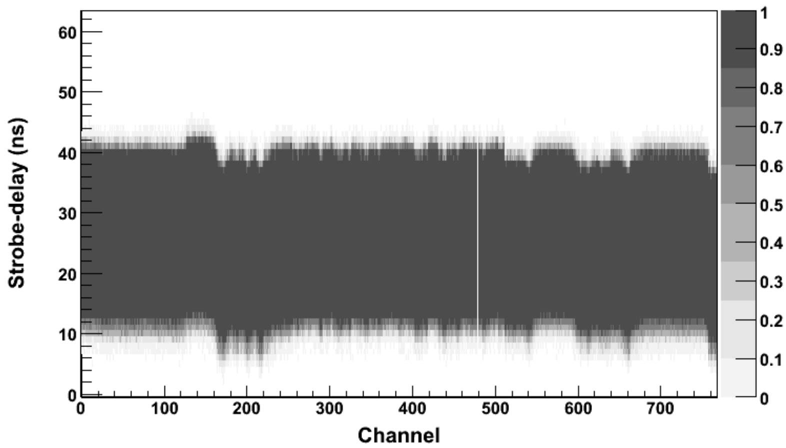

Figure 5.10: Strobe-delay scan result for one link of an SCT end-cap module.

During the scan a 4 fC injection charge is used, while the value of the discriminating threshold is set to correspond to a 2 fC signal. This is done so that for the correct timing of the delay, all triggers should correspond to a hit. The optimum delay setting is determined from the delay-value at 40% between the start and end of the full occupancy region, so that the signal is sampled at or close to its maximum.

5.5.3 Noise and gain measurement

The S-curves that are measured for each SCT channel determine the *output noise* on the signal. By measuring the *gain* of the analog signal amplification, the *input noise* of each channel can be determined. The input noise can be used to identify several channel defects and helps to determine if the module was properly biased.

The gain is determined, for each chip, by measuring S-curves at three different values of the injected charge; 1.5 fC, 2 fC and 2.5 fC. The gain (in mV/fC) then follows from the slope of a linear fit to the three V_{t50}-points as is shown in figure 5.11. The output noise of each channel divided by the gain-factor of the chip results in the measured value of the input noise.

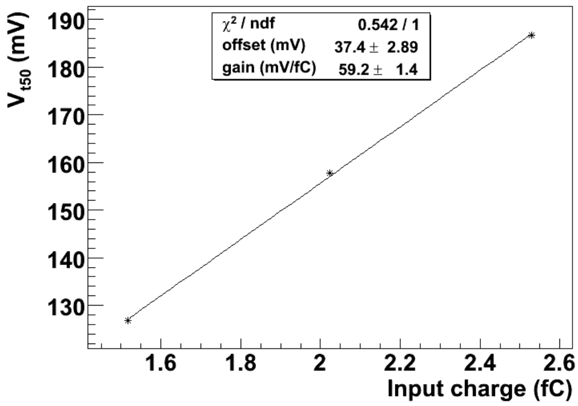

Figure 5.11: Example of fit to determine gain (in mV/fC) from measurements of the V_{t50}-points at three different value of the input charge. The V_{t50}-points represent the average value for all channels on the read-out chip.

Figure 5.12 shows an example of the input noise measured for the 1536 channels of an Outer-type SCT end-cap module. The average noise in this module corresponds to around $16{\cdot}10^2$ electrons, which is the typical noise value for an Outer-type module[4]. The most probable charge deposit of a minimum ionizing particle in one strip is $21{\cdot}10^3$ electrons (see section 3.2.1), so that the expected signal over noise ratio for this module is ≈ 13.

From the measurement of the input noise several channel defects can be identified. The main channel defects are defined as:

- *Dead*, measured input noise = 0, no hits are measured at any threshold for any injected charge

- *Unbonded*, measured input noise is < 800, most likely as a result of broken bond between the hybrid and the silicon strip sensor.

- *Part-bonded*, measured input noise is < 1100, a result of a broken bond between the two daisy-chained silicon sensors, used in the extended surface of the Outer and Middle modules.

- *Noisy*, the input noise is greater than 1.15 times the average input noise of all channels on the same chip.

[4]The expected value of the input noise depends on the length of the silicon strips used in the different types of modules.

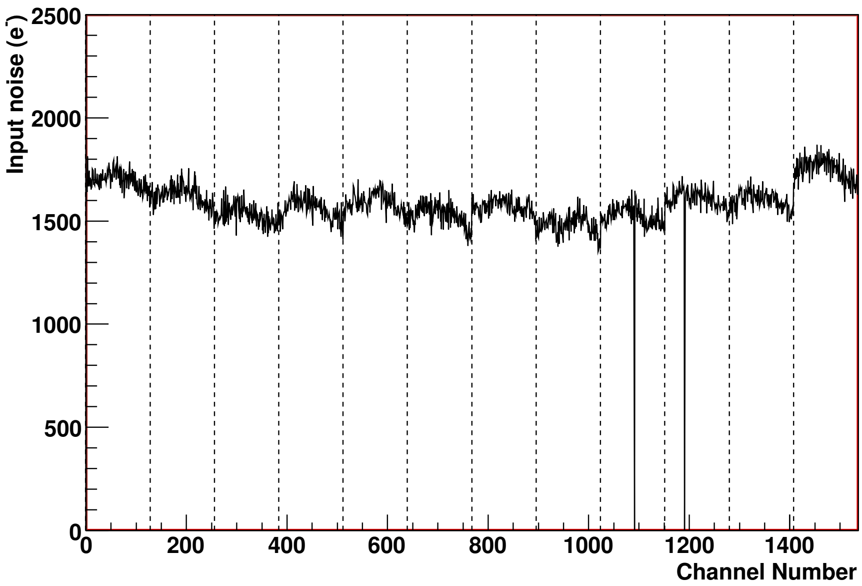

Figure 5.12: Example of the input noise measured on one SCT end-cap module with two defects, namely 'dead' channels at 1091 and 1191.

- *Very-noisy*, the input noise is greater than 1.25 times the average input noise of all channels on the same chip.

The assumptions made for the input noise of "part-bonded" and "unbonded" channels are based on the fact that the capacitive load on the channel is decreased when the silicon strip sensor is reduced/removed from the read-out chain, resulting in a lower noise contribution. Since inner modules and short-middle modules use only one single sensor on each side of the module, their channels could never have a "part-bonded" defect, and their input noise is typically around 1000 e^-.

5.5.4 Input noise results

The average input noise measured on the modules differs between the different types of modules due to the different length of the silicon strips. Longer silicon strips have a higher capacitance and thus a higher expected value for the input noise.

The input noise also depends on the temperature of the silicon. The sensor temperature typically varies between modules and depends on the settings of the cooling used during the test. In the region of module temperatures during the assembly tests, the temperature dependence of the input noise can be approximated by a linear function [50]. Figure 5.13 shows the average noise on the different types of modules, as a function of the temperature[5].

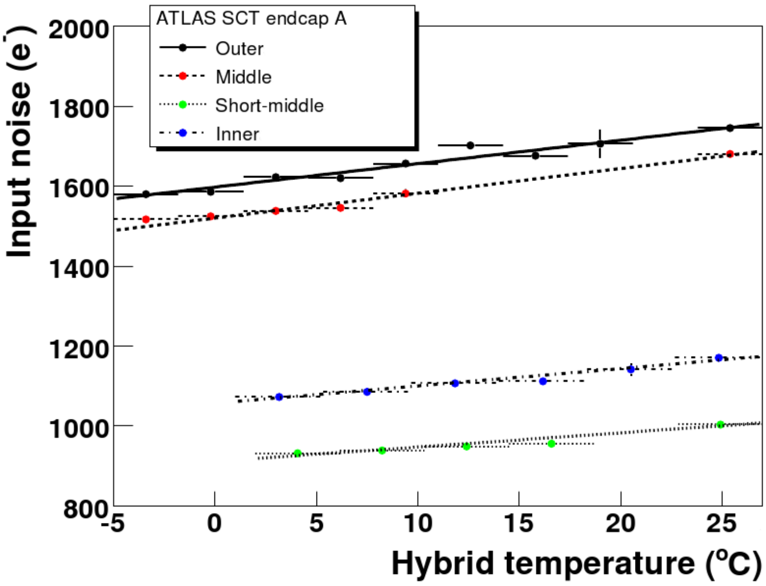

Figure 5.13: Input noise versus temperature, showing the straight line fits from which the temperature coefficients were determined.

The slopes of the straight line fits in figure 5.13 are given in table 5.2. The values in table 5.2 were used to apply a temperature correction to the average measured input noise on each module, so that all results for the input noise correspond to a hybrid temperature of 0°C.

Module type	temperature dependence average input noise (e^-/°C)
Outer	5.9±0.2
Middle	6.1±0.2
Inner	4.4 ±0.2
Short-middle	3.6 ±0.2

Table 5.2: Temperature dependence of the input noise for the different type of SCT end-cap modules.

The average input noise, after temperature correction, is illustrated for the

[5]Module temperature is measured at the electronics part of the modules, in this approximation it is assumed that the temperature of the silicon sensor is linearly dependent to this temperature.

four different types of modules in figure 5.14, representing the test results from the modules-to-disk test made at Nikhef.

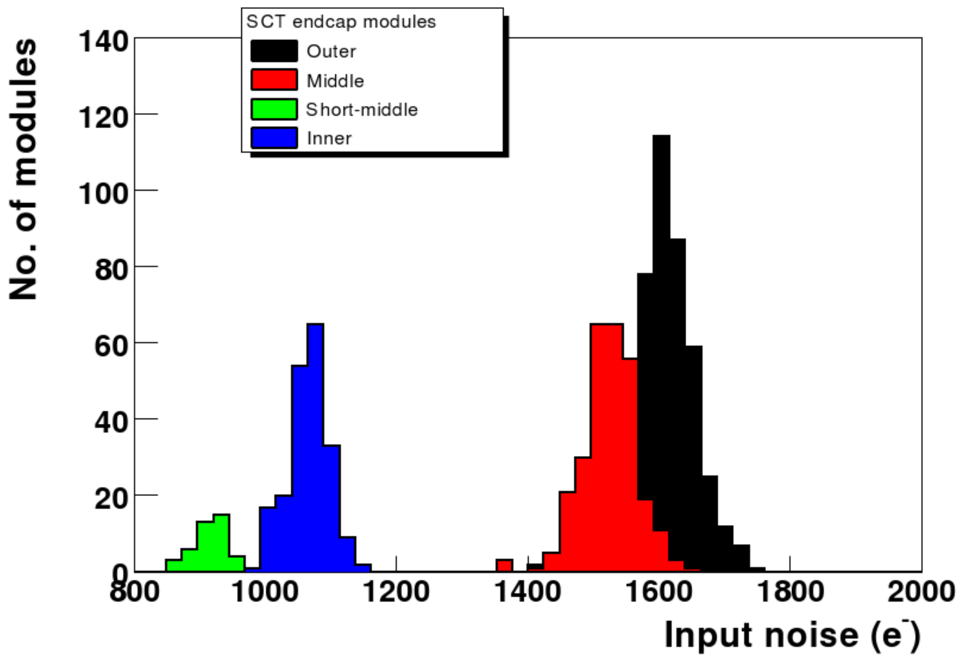

Figure 5.14: Input noise as measured during the modules-to-disk test at Nikhef for all modules of SCT end-cap A. All values have been corrected to correspond to a temperature of 0°C

It was important to ensure that the input noise of the modules does not increase with services successively added to the system, as that would indicate problems in the grounding scheme. Table 5.3 shows the results of the input noise as measured in the four main test stages, from which can be concluded that the input noise did not increase and that no common-mode noise has been introduced into the system.

5.6 Module problem summary

5.6.1 Defective channels results

The number of channel defects found per module is shown in figure 5.15, separated into the different type of channel defects that are found from measuring the input noise on the modules. The most frequently occurring defects are dead channels. The data used to generate this plot was taken during the CERN reception tests, but no significant change in the number of channel defects was found between the different test stages. The number of channels with

Module type	**Modules -to-disk**		**Disk-to -cylinder**		**CERN reception**		**ATLAS cavern**	
	mean	σ	mean	σ	mean	σ	mean	σ
Outers	1608	44	1590	40	1600	37	1612	37
Middles	1525	39	1516	43	1527	42	1540	42
Inners	1067	30	1055	29	1055	28	1059	29
Short-middles	916	27	909	31	913	30	913	31

Table 5.3: Average input noise in electrons, as measured during the four main test stages for all modules of SCT end-cap A. All values have been corrected to correspond to a module temperature of 0°C.

certain defects is listed in table 5.4. From the defective channel results it can be concluded that 99.7% of all channels in the SCT end-cap are operational.

5.6.2 Dead chips

The channel defects listed in table 5.4 do not include the unusable channels from a total of 3 dead chips found on SCT end-cap A. The latest configuration of the SCT end-cap[6] has 3 chips bypassed. The problems with these chips were found during the CERN receptions tests, where some modules failed to complete the calibration tests. Eventually these problems were solved by bypassing a specific chip on each module, but it remains unclear what are the exact problems with these chips. In order to ensure stable running of the SCT end-cap A while taking physics data, these chips remain bypassed. The

[6]Commissioning of SCT end-cap A in ATLAS cavern, January/February 2008

Defect type	**No. of channels**	**% of total channels**
Dead	3169	0.208%
Unbonded	357	0.023%
Part-bonded	45	0.003%
Noisy	235	0.015%
Very-noisy	91	0.006%
Total	3897	0.257%

Table 5.4: Channel defects on SCT end-cap A.

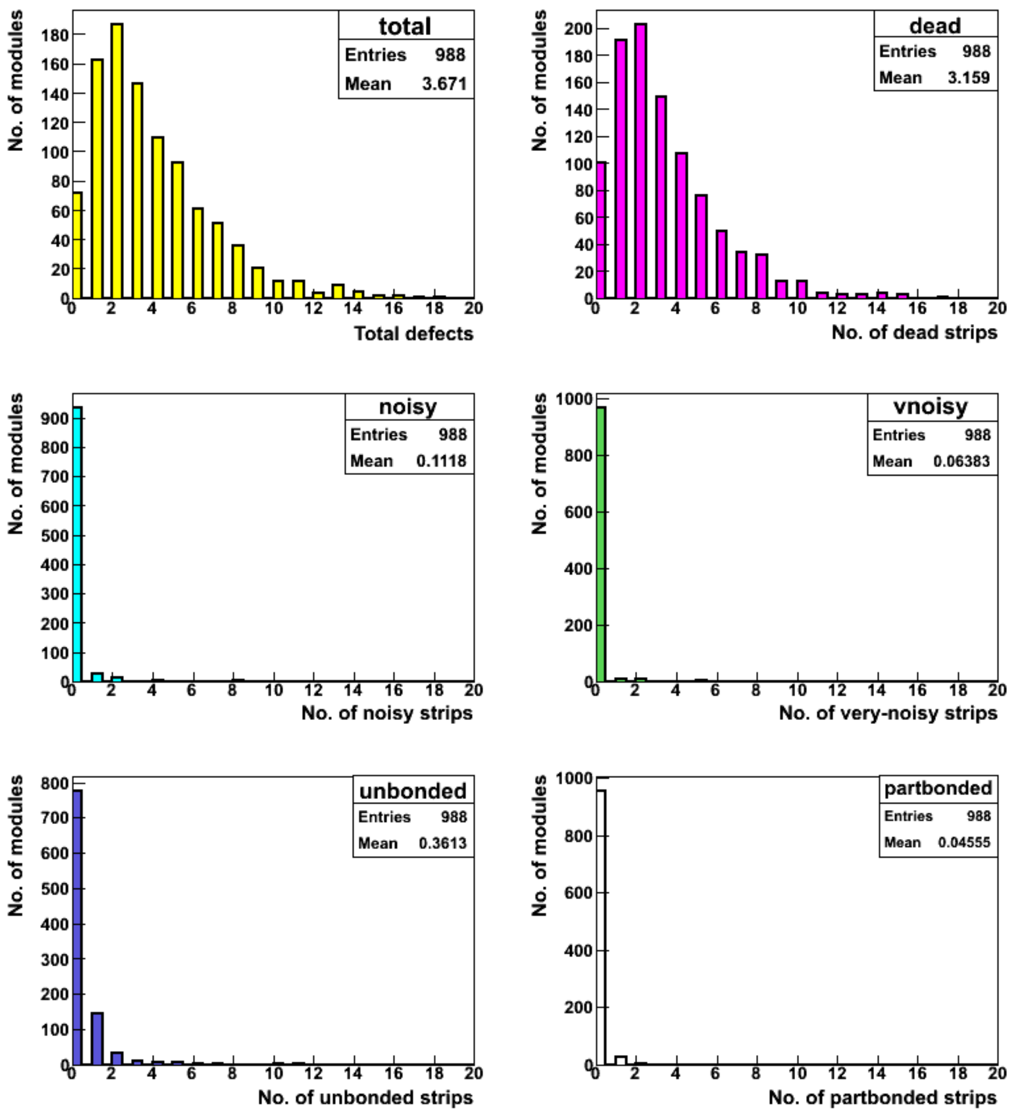

Figure 5.15: Channel defects per module for all modules on SCT end-cap A.

problematic chips give rise to an additional loss of 3×128=384 channels.

5.7 Conclusion

The SCT module performance was tested during all assembly stages of the SCT end-cap including the commissioning of the detector in its final position within the ATLAS experiment. These tests show that the SCT end-cap modules perform within their specification. The leakage current was measured to be within the requirement of less than 6 μA at 150 V bias Voltage.

Tests were done to check the performance of the front-end read-out electronics. Three chips were found to be unusable, resulting in the loss of 384 channels of the SCT end-cap. Very few defects were found for the digital functions of the chips. The total number of channels in the SCT that can be used after subtracting channel losses from dead, noisy or unbonded channels, is 99.7% which is well within the required 99% efficiency for the detector.
The measurement of the input noise during several test stages shows that the input noise on the modules did not change between the test stages, indicating that no common mode noise was added to the system during assembly.

Chapter 6

Vertex fitting with kinematic constraints

This chapter introduces the ATLAS track and vertex reconstruction using the measurements provided by the inner detector. Track reconstruction aims to accurately reconstruct the trajectories of charged particles. Reconstruction of the common intersection point of a set of particle trajectories helps to identify the decay point, or vertex, of unstable particles.

In order to improve the resolution of the reconstructed decay vertices, information about the physical laws governing a particle decay can be exploited by adding kinematic constraints to the vertex fit. A method for kinematically constraining a vertex fit was developed and will be described in detail in this chapter.

One example of a kinematic constraint in a vertex fit is requiring the invariant mass of the decay-products to be equal to the mass of the decaying particle. This constraint can be used to improve the resolution of the momentum of reconstructed muons from the decay of J/ψ-particle as will be presented in this chapter.

6.1 Athena framework and applications

A common software framework is needed for the large set of software applications used for the reconstruction and simulation of events in the ATLAS detector. The ATLAS software is implemented in the Athena [51] framework. This framework takes care of the order of running the requested algorithms, and it offers various common services used by the different algorithms, such as access to information about the detector geometry, magnetic field and calibration constants.

The software is designed to reconstruct data taken by the ATLAS detector and also to produce simulated events of proton-proton collisions in ATLAS.

Samples of simulated events are of vital importance for testing the reconstruction algorithms and preparing data analysis before the start of the LHC. The steps to simulate and reconstruct events are schematically:

- **Event generation:** The first step in the simulation chain is the simulation of the proton-proton collision itself. The physics processes in high-energy collisions are described in event generators, such as Pythia [5], that simulate the particles and their momentum four-vectors as produced in a collision .

- **Detector simulation:** The second step is to simulate the interactions of the generated particles with the material in the detector. This task is performed by the GEANT4 [52] program which uses a detailed description of the ATLAS geometry and the material distribution in the detector. The GEANT4 algorithms transport the particles through the magnetic field and simulates material interactions such as multiple scattering, energy loss, and photon conversions. The decay of unstable particles is also simulated at this stage.

- **Detector response:** At the next stage, the response of the detector including electronics is simulated. This step is also called digitization. If a particle hits a detection volume (like a silicon sensor), a 'hit' is registered in the simulated detector response. The digitization consists of simulating the response of the detector to the energy deposits in these hits. Both the response of the detector and of the electronics are simulated in a fair amount of detail. The output format of the detector response simulation is equivalent to the real data after the bytestream conversion and mapping[1] took place.

- **Reconstruction:** Starting from the detector response data, which can be real or simulated, various algorithms are used to reconstruct the event. This includes algorithms that perform pattern recognition, track fitting, vertex determination, energy measurement and particle identification. On simulated data, the reconstructed objects can be matched and compared to the simulated input to validate the performance of the ATLAS reconstruction software.

All the calibration data required by the event reconstruction is stored in the ATLAS conditions database where it can be accessed by the different Athena software applications. Calibration constants are used to convert various raw detector data in position or energy measurements.

[1] Assigning the output of the read-out channels to the different detector elements.

6.2 Track reconstruction

A large number of charged particles will be produced in the proton-proton collision of the LHC, resulting in a large number of hits in the ATLAS inner detector. The track reconstruction software has to distinguish the hits from the different charged particles and determine a trajectory that best matches the measurements.

6.2.1 Track finding strategy

Track reconstruction in the inner detector uses the measurements of the pixel, SCT and TRT detectors. Several strategies for track finding in the ATLAS inner detector are available [53][54][55]. The main track reconstruction strategy is the "inside-out" strategy, which starts by finding a track candidate in the pixel and SCT detectors and then extends the trajectories of successfully fitted tracks to the TRT to reconstruct a full inner detector track.

Figure 6.1 shows the number of measurements made along a trajectory in the inner detector for tracks originating from the interaction point as a function of $|\eta|$ as found with the inside-out track strategy. The tracks have on average 3 pixel hits and 8 hits from the silicon strip detectors close to the interaction point. The tracks also have an average of 30 TRT-hits, at larger distances from the interaction point, that provide an accurate measure of the curvature of the track.

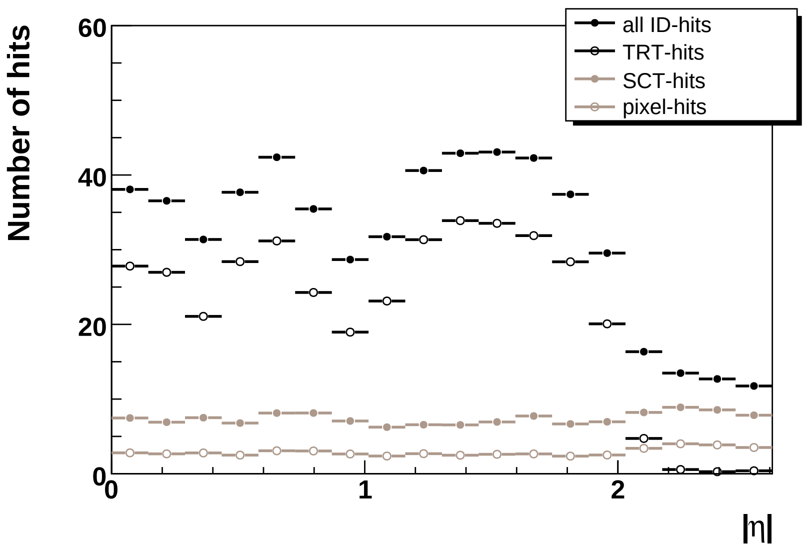

Figure 6.1: Number of hits by detector type used in reconstructed tracks in the inner detector as a function of $|\eta|$.

The main steps of the inside-out track strategy are as follows:

- **Pattern recognition**: The measurements in the pixel and SCT detectors form *silicon space-points*. Each silicon space-point represents a 3D precision point which is formed either from a cluster of silicon pixels or from the intersection of the front and backside silicon strips in an SCT module. The pattern recognition starts by finding track seeds that are formed of all three silicon space-points that are compatible with a minimum p_T cut of 500 MeV.
  The track seeds provide already enough directional information to associate additional silicon hits to the track segment by using a fast Kalman filter [56] to follow the trajectory. At this stage information from the separate silicon pixel and strip hits is used, rather than the silicon space-points. If the track seeds can be extended to contain a minimum of 7 silicon hits, a track candidate is formed.
  Depending on the underlying physics event, a large amount of track seeds can be found in each event. Figure 6.2 shows an example of the track seeds found in a simulated $t\bar{t}$ event in ATLAS. Many of the proposed track seeds represent fake track segments and can not be extended to form track candidates.

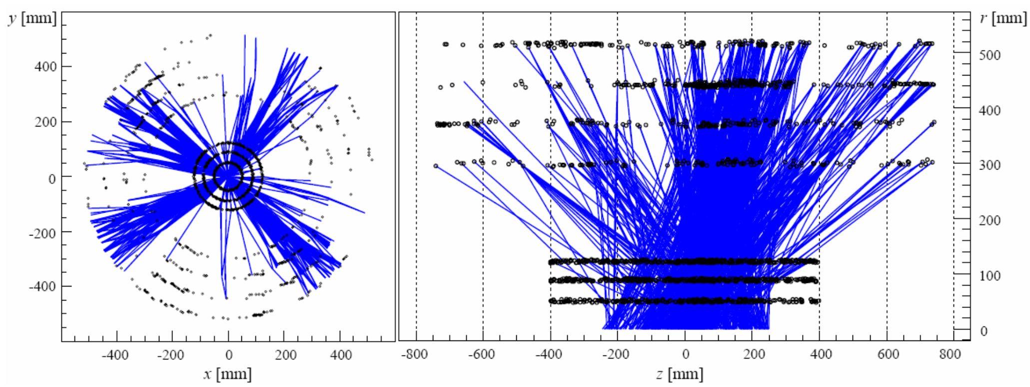

Figure 6.2: Track seeds consisting of three silicon space-points in the ATLAS inner detector barrel as found in a simulated $t\bar{t}$ event [53].

- **Ambiguity solving**: Many of the initial track candidates share hits, are incomplete or are fake tracks. The ambiguity solving process assigns a 'score' to each track candidate to indicate the likelihood that the track candidate originated from a real particle trajectory. In general, each hit associated with the track leads to higher score, in order to favor fully reconstructed tracks over smaller track segments. On the other hand, 'holes', defined as the passage of the track through a detector element without producing a hit, will lower the track score. Hits that are shared between tracks are assigned to the track with the highest score and removed from the other track. Track candidates that after the ambiguity solving process have less than the minimum number of 7 hits are neglected for further processing.

- **TRT track extension**: The fitted silicon track parameters at the outermost silicon measurement, closest to the TRT, are used to define a road through the TRT, and any drift radius measurements that are within 10 mm of this road are assigned to the silicon track.
  The track is re-fitted with the addition of the TRT measurements and compared with the original silicon-only track using the track scoring mechanism. In the case that the track score of the silicon track was higher than the extended version, the silicon track is kept.

This track reconstruction sequence is complemented by an 'outside-in' strategy. The outside-in strategy starts from unassigned TRT segments and looks for matching hits in the pixel and SCT detectors. This type of track reconstruction is mainly aimed at late decays of neutral particles and photon conversions to e^+e^- pairs, and is also able to recover the remaining trajectory after a catastrophic energy loss.

Figure 6.3 shows the track reconstruction efficiency as a function of $|\eta|$ for isolated muons, pions and electrons with p_T=5 GeV, as was obtained using simulated events [16]. In addition to multiple scattering, pions are affected by hadronic interactions in the inner detector material, while electrons are subject to even larger reconstruction inefficiencies due to bremsstrahlung. As a result, the efficiency curves as a function of $|\eta|$ for pions and electrons reflect the increase of material in the inner detector in the forward direction.

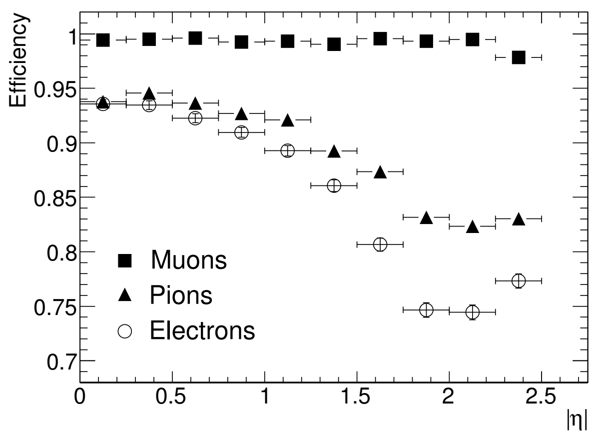

Figure 6.3: Track reconstruction efficiencies in the inner detector as a function of $|\eta|$ for muons, pions and electrons with p_T= 5 GeV [16].

6.2.2 Track parametrization

A track in ATLAS is parametrized at the point of closest approach with the global Z-axis using five *perigee parameters* (as illustrated[2] in figure 6.4):

- $\frac{\mathbf{q}}{\mathbf{p}}$: the charge of the particle divided by the momentum
- $\phi_{\mathbf{0}}$: the angle with the x-axis in the X-Y plane at the perigee point
- $\theta_{\mathbf{0}}$: the angle with the z-axis in the R-Z plane
- $\mathbf{d_0}$: the signed distance to the z-axis. The sign of d_0 is positive, when $\phi - \phi_0 = \frac{\pi}{2} \mod (2\pi)$, where ϕ denotes the angle to the perigee position in the x-y plane, as shown in figure 6.4.
- $\mathbf{z_0}$: the z-coordinate of the track at the point of closest approach to the global Z-axis.

These track parameters can then be propagated to different positions within the ATLAS detector by using the field map of the ATLAS magnetic field.

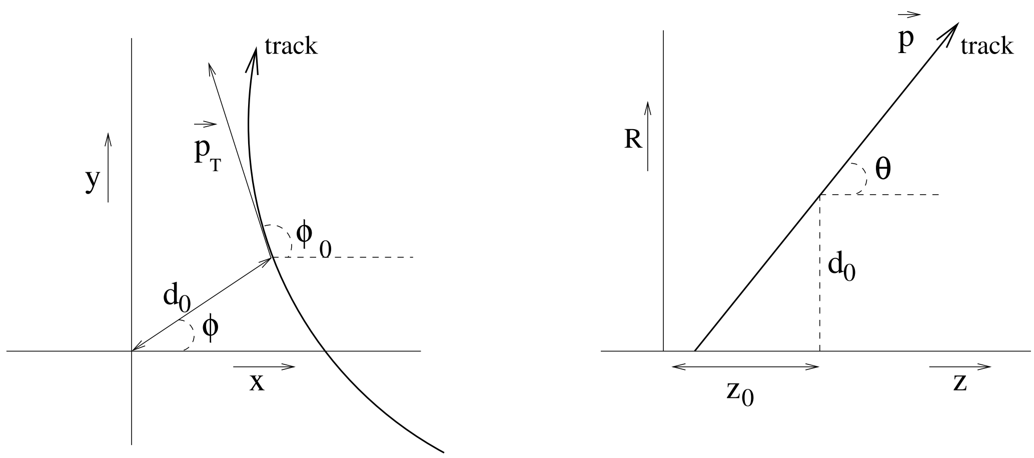

Figure 6.4: Illustration of the perigee parameters of a track in the transverse plane (left) and RZ-plane (right), as defined in the global ATLAS tracking frame.

Apart from the perigee parameters, a reconstructed track object can also contain a set of track parameters at various other positions along the trajectory. These extra track parameters can be used to describe interactions of the particle trajectory with material in the inner detector, which can change the momentum and direction of the track at the scattering centers along the track.

[2] The illustration in figure 6.4 approximates the helix in the RZ-plane as a straight line close to the interaction point.

6.2.3 Track fitting

The pattern recognition provides a list of measurements along a particle trajectory, as well as a first-estimate of the track parameters of the track. The task of the track fitting method is to compute the best possible estimate of the track parameters. The two track fitting techniques which are widely using in high energy physics, the *global least-squares fit* and the *Kalman filter* are both implemented in the ATLAS software framework. In order for the track reconstruction to run with a reasonable CPU time, both track fitters use “material maps” instead of the full ATLAS geometry, to correct the track prediction for multiple scattering and energy loss effects. The material maps in the ATLAS tracking geometry [57] represent the material in the form of layers, each with assigned thickness and radiation length. The track fitting methods also rely on the same *propagator* tool which calculates track parameters and covariance matrices at a destination surface while taking into account the bending of the charged particle in the magnetic field. In ATLAS, the presence of an inhomogeneous magnetic field means that a numerical approximation has to be used. The default propagator in ATLAS uses the Runga-Kutta method [58], which follows the path of particle by taking one step at a time, while optimizing the step-size to reach the required propagation precision. In ATLAS the propagation errors are shown to be within a few microns over distances of up to 10 meters, which is negligible compared to the internal detector resolution.

Global least-squares fit

The global least-squares fit [59] obtains the best estimate for the track parameters by directly minimizing the following χ^2 function:

$$\chi^2 = \sum_{i=1}^{N_{meas}} \left(\frac{\Delta_i}{\sigma_i}\right)^2 + \sum_{i=1}^{N_{layer}} \left(\frac{\theta_{scat}^2}{\sigma_{scat}^2} + \frac{(\sin\theta_{loc})^2\phi_{scat}^2}{\sigma_{scat}^2}\right) \tag{6.1}$$

where the first term is the sum of all the detector hits of the residuals, Δ_i, divided by the by the error on the measurement σ_i. The residuals are given by the distance between the measured and the predicted value of the hit position along the track.
The second term in equation 6.1 is a sum over the number of material layers along the track, N_{layer}. Here the possible change of track direction at a scattering center is implemented by adding two extra fit-parameters, ϕ_{scat} and θ_{scat}. The scattering angles are added to the χ^2 as measurements with zero as initial value and with an error σ_{scat} that is calculated from the traversed material thickness in terms of radiation lengths, see equation 3.1 in section 3.1. The fit also reduces the momentum of the track after traversing a material layer by an amount equal to the average energy loss corresponding to the traversed material.

The minimization of the χ^2 in the global least-squares fit involves the inversion of a large matrix [60] with a size of N $\times$ M, with N the number of fit-parameters and M the number of measurements plus the number of scattering angles used in the fit. The CPU time required for the inversion of the matrix scales with M^2 so for fits with a large number of measurement and scattering planes this inversion can cost a significant amount of CPU time.

Kalman filter

The Kalman filtering technique [56] is a widely used method for track fitting. This techniques determines the optimal track parameters through an iterative process of stepping from one measurement to the next. At each measurement surface the local track parameters are described by the track state vector and the covariance matrix of the state vector.

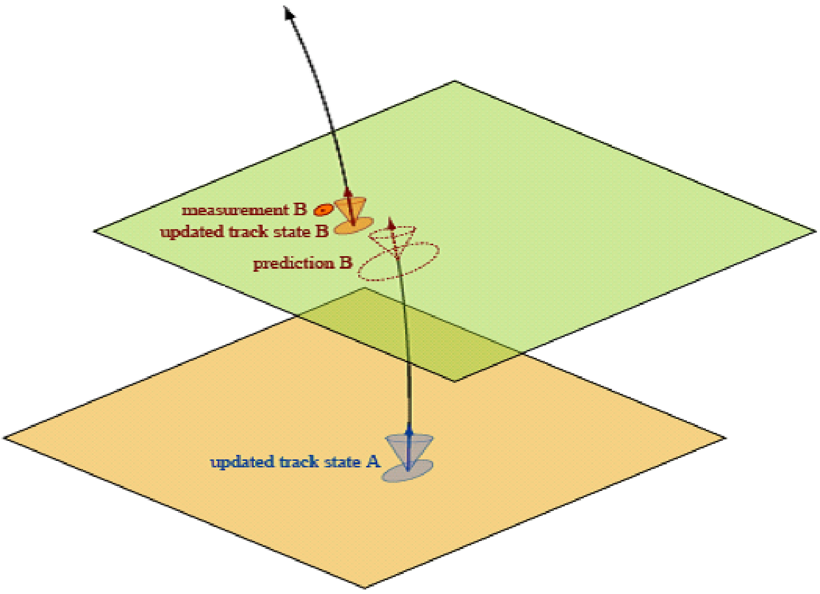

Figure 6.5: A single filtering step in the Kalman method. The different sizes of the ellipses and the cones indicate the change of the errors of the track parameters during a filtering step.

In each filtering step (illustrated by figure 6.5) the track parameters are extrapolated to the next measurement surface to calculate a prediction of the track state at the next surface. Extrapolation involves the propagation through the magnetic field of the track state vector and its covariance matrix, as well as updating the errors when the track passes through a material layer.
The predicted value together with the actual measurement are used to update the track state at the next measurement surface. The filtering process is bi-directional with the aim to get precise parameters both at the perigee position

and at the outer end of the tracks and to have a balanced sensitivity to outliers[3]. One advantage of the Kalman filter is that all calculations are made locally (i.e. one measurement at a time) and the algorithm remains fast, in terms of CPU time, even in the presence of many measurements and multiple scattering planes, since no large matrix inversion is required.

Track fitting performance

The different track fit methods should give identical results, as both are attempting to find to optimum track trajectory by minimizing the hit residuals of the tracks. Figure 6.6 shows the resolutions obtained with the two fitting methods on the impact parameters and the transverse momentum, as function of the transverse momentum, obtained by fitting simulated single muon tracks in the inner detector. It can be seen that the results in figure 6.6 are indeed identical for the two fit methods. The figures show that the resolution on the impact parameter improves for increasing values of p_T, while $\Delta p_T/p_T$ improves at lower values of p_T.

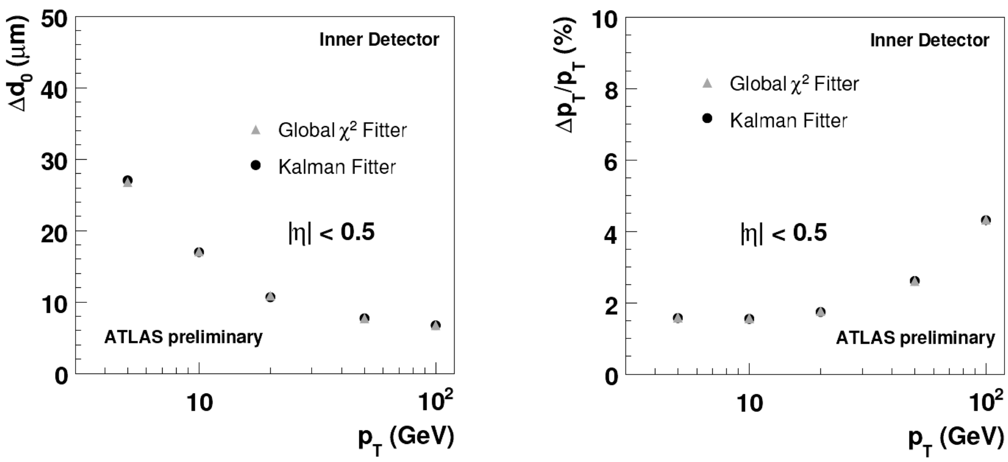

Figure 6.6: Obtained resolutions on the impact parameter (left) and transverse momentum (right) for Kalman filter and global least-squares fit methods for simulation single muon tracks in the inner detector [60].

The time required to fit a track depends on the number of hits and the number of material layers along the trajectory. On average, each inner detector track contains 35 hits and has 15 material layers along the trajectory. In the case of the global least-squares fit this leads to a total of 35 fit parameters (5 from the perigee, 2 × 15 from the scattering angles). Using fast matrix algorithms the global least squares method requires about twice as much CPU

[3]Hits that are incorrectly associated to the track and typically give a large χ^2 contribution.

time as the Kalman filter method. Though the Kalman filter technique is faster than the global least-squares fit, the global least-squares fit has the advantage of the explicit calculation of the scattering angles, which can be used to study the material distributions along the tracks.

At the event reconstruction stage, one of the two track fitters can be selected. At the time of writing the global χ^2 fitter was the default track fitter used for track reconstruction in the inner detector.

6.2.4 Muon identification and combined reconstruction

This thesis focuses on the reconstruction of $J/\psi \rightarrow \mu^+\mu^-$ events, which requires tracks that are identified as muons. To identify a track in the inner detector as originating from a muon, the track has to be matched with a track or track segment in the muon spectrometer. The ATLAS reconstruction software provides several strategies to identify and reconstruct a muon track.

The most commonly used packages for combined tracking are *STACO* and *MUID*. Both algorithms identify muons by pairing tracks reconstructed in the muon spectrometer with tracks reconstructed in the inner detector. MUID produces the combined track from a re-fit of the inner detector track with the addition of the measurements from muon spectrometer track, while STACO determines the combined track parameters from the weighted average of the two sets of track parameters.

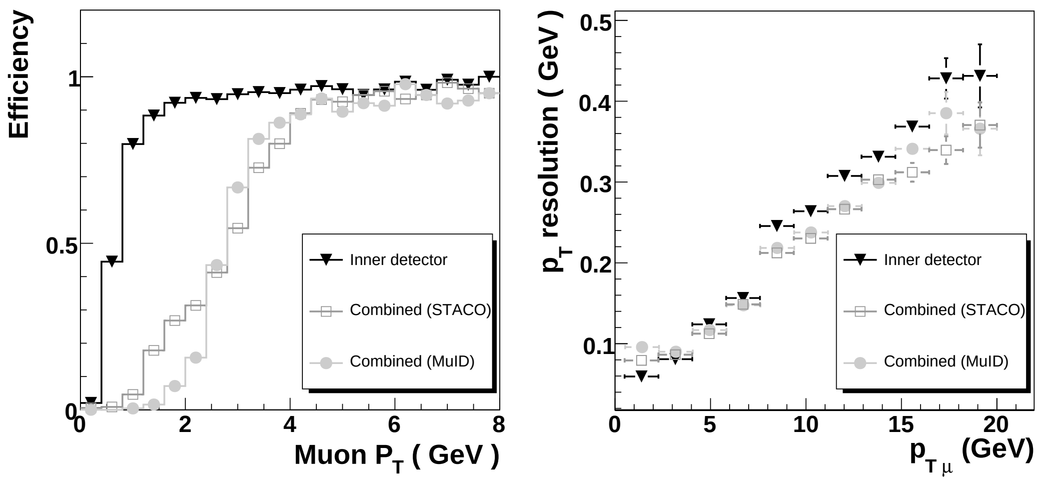

Figure 6.7: Efficiency (left) and p_T resolution (right) of muons in simulated $J/\psi \rightarrow \mu^+\mu^-$ events reconstructed by the combined muon algorithms.

Figure 6.7 shows the efficiency and p_T resolution of tracks reconstructed by the inner detector track reconstruction and the two combined reconstruction strategies. The plots were obtained using a sample of simulated $J/\psi \rightarrow \mu^+\mu^-$

events, in which one of the two muons was required to have a p_T of at least 9 GeV. The plots shows that muon identification only becomes efficient (>90%) for tracks with a transverse momentum greater than 5 GeV, as muon tracks with low transverse momenta are stopped in the calorimeter. For high momentum muons, using the information from the combined measurement in the inner detector and muon spectrometer is expected to improve the p_T resolution of the reconstructed muon. However, this effect is not very significant for $J/\psi \rightarrow \mu^+\mu^-$ events where the muons have relatively low transverse momenta.

6.3 Vertex reconstruction

Finding the common intersection points between sets of reconstructed tracks allows to identify the proton-proton interaction point as well the decay vertices of unstable particles produced in the collision. Identifying and reconstructing different vertices within one event relies on precise track reconstruction and helps to study various physics processes.

Most of the reconstructed tracks from a proton-proton collision in ATLAS will originate from the collision point, indicating the *primary vertex* of that collision. The beam spot defines in which region the proton-proton collisions take place and can be described by a Gaussian with the standard deviation of approximately 5 cm in the direction of the beam and approximately 15 μm in the perpendicular plane. Within this region, especially for high luminosity runs of the LHC, more than one proton-proton interaction per bunch-crossing can take place.

Some particles, such as b-hadrons, can decay at measurable distance from the primary vertex, and tracks originating from such decays can be used to identify *secondary vertices*. A primary vertex often is formed from the intersection of 20 or more reconstructed tracks while secondary vertices are often fitted with just 2 or 3 trajectories. Tracks from secondary vertices can often be identified by a significantly high value of the impact parameter (d_0) relative to the primary interaction.

The work described in this chapter used simulated $b\bar{b} \rightarrow X + (J/\psi \rightarrow \mu^+\mu^-)$ events to validate the performance of a new method for vertex fitting with kinematic constraints. In this type of event, the secondary vertex of the b-decay can be identified from the intersection point of two reconstructed muon tracks with an invariant mass around the J/ψ value.

6.3.1 Vertex fitting

The vertex fit has to determine a common intersection point between the trajectories, given the track parameters and their covariance matrices as determined from the track fit. Several strategies for vertex fitting are currently implemented in the ATLAS reconstruction software [61].

One example of a vertex fit method implemented in ATLAS is the *Billoir vertex fitting method* that follows the scheme presented in [62]. This method finds the vertex position $\vec{x}$ and momentum vector of the tracks $\vec{p_i}$, that minimizes the following χ^2:

$$\chi^2 = \sum_{i=1}^{N} (\vec{\eta}(\vec{x},\vec{p_i}) - \vec{\eta}_{0i})^T V_{\eta 0i}^{-1} (\vec{\eta}(\vec{x},\vec{p_i}) - \vec{\eta}_{0i}), \tag{6.2}$$

where $\vec{\eta}_{0i}$ is the vector of track parameters from the original track fit, $\vec{\eta}(\vec{x},\vec{p_i})$ is the prediction of the track parameters at the perigee and $V_{\eta 0i}$ is the covariance matrix of the track parameters as obtained from the original track fit. In the Billoir method the vertex position is estimated by approximating the equations of motion of a charged particle with a first order Taylor expansion to obtain an analytical solution for the χ^2-minimization. Apart from reconstructing the vertex position and its covariance matrix, the Billoir method also refits the parameters of the incident tracks with the knowledge of the vertex.

The Billoir method for vertex fitting is widely used and the approach is similar to the method for vertex fitting with kinematic constraints that is presented in this thesis. For this reason the Billoir method for vertex fitting will be used as reference in comparing results of the kinematic vertex fit in section 6.5.

6.4 Vertex fitting with kinematic constraints

The use of kinematic constraints in the vertex fit can help to improve the resolution of the fitted parameters and to test the hypothesis of a certain interaction type.

Constrained vertex fitting is implemented in several packages in the ATLAS software framework. As part of the work done here, a tool for constrained vertex fitting [63] has been developed, based on the method of applying kinematic constraints using Lagrange multipliers in the Cartesian tracking frame [64]. At the time of writing, the only implemented kinematic constraints for this tool are the vertex constraint and the mass constraint but the framework of the new method facilitates the implementation of other types of constraints in the future.

6.4.1 Track parameters in the Cartesian frame

The Cartesian coordinates are the momenta and the energy of a track and the position on the track where the momenta are defined:

$$\vec{\alpha} = (p_x, p_y, p_z, E, x, y, z) \tag{6.3}$$

The advantage of using Cartesian coordinates is that they provide a track representation which uses physically meaningful quantities for reconstruction of particle decays and allow the track to be parametrized at the position representing its decay vertex, rather than a global reference point. The use of the Cartesian representation therefore simplifies the formulation of most kinematic constraints.

The Cartesian coordinates are related to the standard perigee track coordinates: $\vec{\eta} = (d_0, z_0, \phi_0, \theta, \frac{q}{p})$ through the following:

$$
\begin{aligned}
p_x &= |\frac{q}{p}|^{-1} \cos\phi \sin\theta \\
p_y &= |\frac{q}{p}|^{-1} \sin\phi \sin\theta \\
p_z &= |\frac{q}{p}|^{-1} \cos\theta \\
E &= \sqrt{|\frac{q}{p}|^{-2} + m^2} \\
x &= x_{\text{ref}} - d_0 \sin\phi \\
y &= y_{\text{ref}} + d_0 \cos\phi \\
z &= z_{\text{ref}} + z_0
\end{aligned}
\tag{6.4}
$$

It can be noted that in the Cartesian frame the track is represented by a set of 7 parameters instead of 5. The extra parameters make the Cartesian frame an over-constrained parametrization, which is reflected by the correlations in the corresponding 7×7 covariance matrix, V_α.

The covariance matrix V_α, that represents the errors and correlations of the track parameters in the Cartesian frame, is obtained by transforming the original 5×5 matrix, V_η, with the Jacobian matrix $\mathbf{J}$:

$$
V_\alpha = \mathbf{J} V_\eta \mathbf{J}^T \tag{6.5}
$$

The Jacobian matrix $\mathbf{J}$ for this coordinate change can be computed by taking the differentials of the equations in 6.4 as is explained in appendix B.

6.4.2 Lagrange multiplier technique for adding constraints

Each kinematic constraint is expressed as a vector of equations $\mathbf{H}(\vec{\alpha}_i, \vec{x})$, where $\vec{\alpha}_i$ is a vector of Cartesian parameters of all tracks participating in the fit and $\vec{x}$ is the vertex position. The constraint equations are formulated such that when $\mathbf{H}(\vec{\alpha}_i, \vec{x}) = 0$, the constraint is satisfied.

The constraint equations are linearized by using the first order Taylor expansion around a convenient point $(\vec{\alpha}_A; \vec{x}_A)$:

$$\begin{aligned} 0 &= \left[\frac{\partial \mathbf{H}(\vec{\alpha}_A, \vec{x}_A)}{\partial \vec{\alpha}}\right](\vec{\alpha} - \vec{\alpha}_A) + \left[\frac{\partial \mathbf{H}(\vec{\alpha}_A, \vec{x}_A)}{\partial \vec{x}}\right](\vec{x} - \vec{x}_A) + \mathbf{H}(\vec{\alpha}_A, \vec{x}_A) \\ &\equiv \mathbf{D}(\vec{\alpha} - \vec{\alpha}_A) + \mathbf{E}(\vec{x} - \vec{x}_A) + \mathbf{d}, \end{aligned} \quad (6.6)$$

where **d** is the vector of values of the constraint equations at the expansion point $(\vec{\alpha}_A; \vec{x}_A)$, **D** is the matrix of partial derivatives of the constraint equations at the expansion point with respect to the track parameters and **E** is the matrix of the partial derivatives of the constraint equations at the expansion point with respect to the vertex coordinates.

The constrained vertex fit has to find the solution for the values of $\vec{\alpha}$ and $\vec{x}$ in equation 6.6, and at the same time minimize the χ^2 contribution of the original track fit. The method of Lagrange multipliers solves these problems by introducing an extra set of variables, $\vec{\lambda}$, so that the χ^2 function to be minimized is given by:

$$\chi^2 = (\vec{\alpha} - \vec{\alpha}_0)^T V_{\alpha_0}^{-1} (\vec{\alpha} - \vec{\alpha}_0) + 2\lambda^T (\mathbf{D}(\vec{\alpha} - \vec{\alpha}_A) + \mathbf{E}(\vec{x} - \vec{x}_A) + \mathbf{d}), \quad (6.7)$$

where the first term is the χ^2 contribution from the original track fits and the second term is the contribution from the constraints, with $\vec{\lambda}$ the vector of Lagrange multipliers.

The quantities $\vec{\alpha}_0$ and V_{α_0} in equation 6.7 are the old track parameters and the covariance matrix from the original track fit. The original error matrix $V_{\alpha 0}$ contains in block-diagonal form the covariance matrices of the Cartesian track parameters:

$$V_{\alpha 0} = \begin{pmatrix} V_{\alpha 1} & \emptyset & \cdots & \emptyset \\ \emptyset & V_{\alpha 2} & \cdots & \emptyset \\ \vdots & \vdots & \ddots & \vdots \\ \emptyset & \emptyset & \cdots & V_{\alpha N} \end{pmatrix}, \quad (6.8)$$

where the zero entries on the off-diagonal elements of $V_{\alpha 0}$ represent the lack of correlations between the track parameters of different tracks before the constraints are applied.

The values of track parameters $\vec{\alpha}$ and vertex position $\vec{x}$ that satisfy the given set of constraints can be found by minimizing the χ^2 in equation 6.7 with respect to $\vec{\alpha}$, $\vec{x}$ and $\vec{\lambda}$, resulting in the following equations:

$$\begin{aligned} V_{\vec{\alpha}_0}^{-1}(\vec{\alpha} - \vec{\alpha}_0) + \mathbf{D}^T \lambda &= 0, \\ \mathbf{E}^T \lambda &= 0, \\ \mathbf{D}(\vec{\alpha} - \vec{\alpha}_A) + \mathbf{E}(\vec{x} - \vec{x}_A) + \mathbf{d} &= 0, \end{aligned} \quad (6.9)$$

where the second equation is the same as equation 6.6 which shows that the solution of the χ^2 minimization satisfies the (linearized) constraints.

The solution for the updated track parameters $\vec{\alpha}$ and the vertex prediction $\vec{x}$ is given by [64]:

$$\begin{aligned} \vec{\alpha} &= \vec{\alpha}_0 - V_{\alpha_0}\mathbf{D}^T\lambda && (6.10)\\ \vec{x} &= \vec{x}_A - V_E E^T\lambda_0 && (6.11) \end{aligned}$$

where the vectors λ_0 and λ and the matrix V_E are given by:

$$\begin{aligned} \lambda_0 &= V_D(\mathbf{D}(\vec{\alpha}_0 - \vec{\alpha}_A) + d),\\ V_E &= (\mathbf{E}V_D\mathbf{E}^T)^{-1},\\ \lambda &= \lambda_0 + V_D\mathbf{E}\vec{x}, && (6.12)\\ \text{where } V_D &= (\mathbf{D}V_{\alpha_0}\mathbf{D}^T)^{-1}. \end{aligned}$$

This solution was obtained using linearized constraint-equations at a chosen expansion point, and so the updated track parameters and vertex position represent only a first guess of the actual solution. The solution only becomes exact once the chosen expansion point is equal to the vertex position and updated track parameters that minimize the χ^2. For this reason, the vertex fit uses an iterative procedure that updates the expansion points $\vec{\alpha}_A; \vec{x}_A$ to be equal to the new values obtained by equation 6.11 and repeats the calculation of the $\mathbf{D}$, $\mathbf{E}$ and $\mathbf{d}$ to find an improved solution. The iterative procedure continues until the vertex prediction for one iteration becomes equal to that of the previous iteration.

After the final iteration the covariance matrices of the vertex and updated track parameters are determined. The covariance matrix of the vertex position, V_x, is equal to V_E. The covariance matrix of the updated track parameters is given by:

$$\begin{aligned} V_\alpha &= V_{\alpha 0} - V_{\alpha 0}\mathbf{D}^T V_{\tilde{D}}\mathbf{D}V_{\alpha 0}, && (6.13)\\ \text{where } V_{\tilde{D}} &= V_D - V_D\mathbf{E}V_E\mathbf{E}^T V_D. \end{aligned}$$

The new covariance matrix V_α now contains the covariance matrices of the updated track parameters as well as the correlation between the track parameters of different tracks created by imposing the constraints.

6.4.3 Mass constraint

The equation to force a number of N trajectories to have a common invariant mass m_{constr} can be written as:

$$\mathbf{H}_0 = (\sum_{i=0}^{N} E_i)^2 - (\sum_{i=0}^{N} p_{xi})^2 - (\sum_{i=0}^{N} p_{yi})^2 - (\sum_{i=0}^{N} p_{zi})^2 - (m_{constr})^2 = 0, \quad (6.14)$$

where p_{xi}, p_{yi}, p_{zi} represent the momenta of the track at the decay vertex. These momenta are not the same as in the Cartesian coordinates of tracks, which were obtained from transforming the track parameters at the perigee position (see equation 6.4). In order to determine the value of p_{xi}, p_{yi}, p_{zi} at a the vertex position, the Cartesian coordinates have to be transported through the magnetic field. The magnetic field is approximated to be perfectly solenoidal so that the coordinates on any point along the track can be calculated as function of the path length s by:

$$\begin{aligned}
p_x &= p_{0x}\cos\rho s - p_{0y}\sin\rho s \\
p_y &= p_{0y}\cos\rho s + p_{0x}\sin\rho s \\
p_z &= p_{0z} \\
E &= E_0 \\
x &= x_0 + \frac{p_{0x}}{a}\sin\rho s - \frac{p_{0y}}{a}(1-\cos\rho s) \\
y &= y_0 + \frac{p_{0y}}{a}\sin\rho s + \frac{p_{0x}}{a}(1-\cos\rho s) \\
z &= z_0 + \frac{p_{0z}}{|\vec{p}|}s
\end{aligned} \tag{6.15}$$

where $(p_{x0}, p_{y0}, p_{z0}, E_0, x_0, y_0, z_0)$ are the original coordinates, $\rho = a/p$ and a is a bending factor which, for momentum units in MeV and coordinate units in mm, is given by $a = -0.2997 \cdot Bq$, where q is the charge of the particle and B the magnetic field strength in Tesla.
Eliminating s in equations 6.15, the momentum of the track can be defined in terms of its position:

$$\begin{aligned}
p_x &= p_{0x} - a(y - y_0) \\
p_y &= p_{0y} + a(x + x_0) \\
p_z &= p_{0z}
\end{aligned} \tag{6.16}$$

So the equation that forces a set of track parameters to have an invariant mass m_{constr} at a vertex $(x_{vtx}, y_{vtx}, z_{vtx})$ is written as:

$$\begin{aligned}
\mathbf{H}_0 &= \left(\sum_{i=0}^{N} E_i\right)^2 - \left(\sum_{i=0}^{N}(p_{xi} - a(y_{vtx} - y_i))\right)^2 - \left(\sum_{i=0}^{N}(p_{yi} + a(x_{vtx} - x_i))\right)^2 \\
&\quad - \left(\sum_{i=0}^{N} p_{zi}\right)^2 - (m_{constr})^2 = 0
\end{aligned} \tag{6.17}$$

Solving this constraint using the Lagrange multiplier technique requires the formulation of **D** and **d**. In this case **d** is a one-dimensional vector containing the value of $\mathbf{H}_0(\vec{\alpha}_A)$ and **D** is a matrix of size $1 \times 7N$ that can be calculated from the derivatives of equation 6.17.

6.4.4 Vertex constraint

The vertex constraint consist of two constraint equations for each trajectory in the vertex fit. For a solenoidal magnetic field these equations are given by [64]:

$$\begin{aligned} H_{i+1} &= p_x \Delta y - p_y \Delta x - \frac{a}{2}(\Delta x^2 + \Delta y^2) = 0., \\ H_{i+2} &= \Delta z - \frac{p_z}{a} \sin^{-1}\left(a(p_x \Delta x + p_y \Delta y)/p_T^2\right) = 0., \end{aligned} \tag{6.18}$$

where $\Delta x = x_{trk} - x_{vtx}$, and a is the bending factor as defined previously. The corresponding **E** and **D** matrices can be written for n tracks as:

$$\mathbf{E} = \begin{pmatrix} E_1 \\ E_2 \\ \vdots \\ E_3 \end{pmatrix}, \ \mathbf{D} = \begin{pmatrix} D_1 & \emptyset & \dots & \emptyset \\ \emptyset & D_2 & \dots & \emptyset \\ \vdots & \ddots & \ddots & \vdots \\ \emptyset & \dots & \emptyset & D_n \end{pmatrix} \tag{6.19}$$

where $\mathbf{E}_i$ is a 2×3 matrix and $\mathbf{D}_i$ is a 2×7 matrix. The block diagonal form of **D** results from the vertex constraint equations of each track having no correlation with the track parameters of the other tracks since each track is separately constrained to pass through the vertex position. The matrix $\mathbf{E}_i$ can be determined from taking the derivatives of equations versus the vertex coordinates and the matrix $\mathbf{D}_i$ can be determined from taking the derivatives of equations versus the track parameters of the i-th track.

6.4.5 The *VertexKinematicFitter* software package

The method described in section 6.4 was implemented as an additional tool for vertex fitting in the ATLAS software framework. An important feature of the new *VertexKinematicFitter* software package is that it provides a general framework where any type of user-defined constraint can be added to a vertex fit, while other constrained vertex fitting methods available in ATLAS have always implemented specific constraints as part of a specific tool.

The inputs to the constrained vertex fitter are a set of *kinematic particle* objects, where each kinematic particle represents the track parameters and associated particles mass, together with a list of *kinematic constraints*. The output of the fit contains the vertex position and its covariance matrix as well as the updated track parameters defined at the vertex position.

The constraint equations and their derivatives are contained in the implementations of the different kinematic constraints, while the main method only holds the constraint equations for the vertex constraint. This makes the tool behave as a conventional χ^2 vertex fitter when no additional constraints are given.

6.5 Vertex fit with mass constraint results

In order to study the performance of the kinematic vertex fitting method, a sample of simulated $b\bar{b} \to X + (J/\psi \to \mu^+\mu^-)$ events is used. The simulated sample is based on events where one muon has $p_T > 6$ GeV and the other muon has $p_T > 4$ GeV, corresponding to one possible trigger scenario to be used in real ATLAS data-taking. For each event that had two inner detector tracks that were identified as muons by STACO (see 6.2.4) two types of vertex fits are made. One vertex fit uses the method described in section 6.4 to perform the fit while constraining the invariant mass to the exact value of the J/ψ. Another vertex fit uses the Billoir method for vertex fitting so that the performance of both fit methods can be compared.

Figure 6.8 shows the invariant mass of the reconstructed track parameters at the vertex position obtained with the Billoir method and the kinematic vertex fit with mass constraint. It can be seen that, as expected, the mass constrained vertex fit forces the invariant mass to be exactly equal to the value it was constrained to.

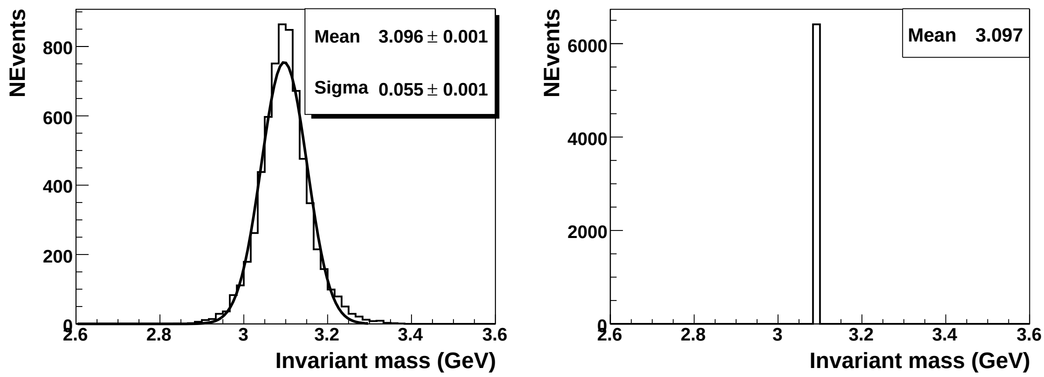

Figure 6.8: Invariant mass of the reconstructed muons at the vertex position as obtained with the Billoir method for vertex-fitting (left) and the kinematic fit with mass constraint (right) using a sample of simulated $b\bar{b} \to X + (J/\psi \to \mu^+\mu^-)$ events

6.5.1 Vertex fitting results

The method for vertex fitting with kinematic constraints implemented an iterative approach to find the best solution for the vertex prediction. Figure 6.9 shows the distance between the reconstructed and the true vertex as a function of the number of iterations of the fit. The initial value of the vertex prediction (corresponding to iteration=0) is always equal to $(0; 0; 0)$. It can be seen that for all the vertices in figure 6.9 the fit converged within 2 iterations.

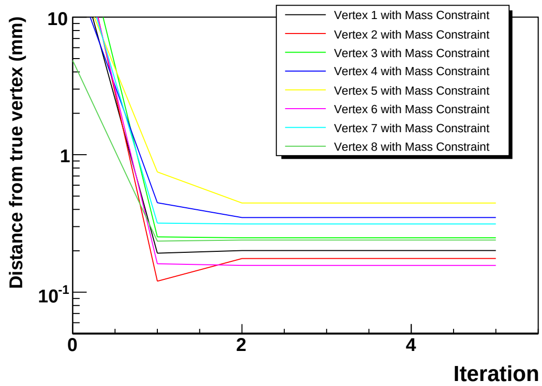

Figure 6.9: Distance between the reconstructed and the true vertex as a function of the number of iterations of the vertex fit with mass constraint, for a sample of 8 vertices from simulated $b\bar{b} \rightarrow X + (J/\psi \rightarrow \mu^+\mu^-)$ events.

The distance between the primary vertex and the secondary vertex reconstructed using the two muon tracks gives a measure of the decay-length of the b-hadron that produced the J/ψ. Figure 6.10 shows the signed transverse decay length, L_{XY}, as obtained using the secondary vertex reconstructed with the Billoir method and the mass constrained vertex fit. It can be seen that the two fitters obtain similar results for the transverse decay length.

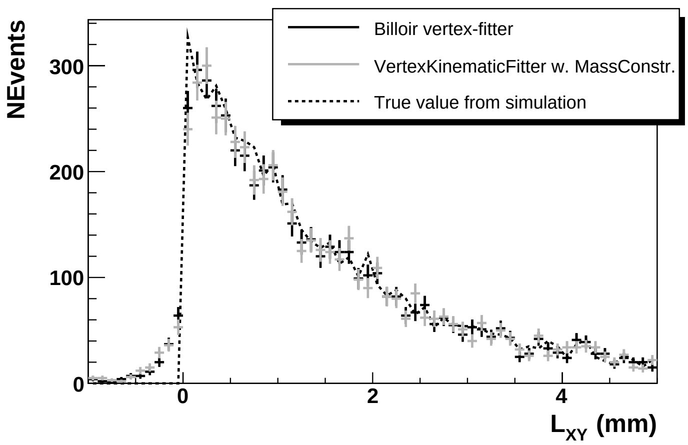

Figure 6.10: Signed transverse decay length as obtained from the secondary vertex of two muon tracks in simulated $b\bar{b} \rightarrow X + (J/\psi \rightarrow \mu^+\mu^-)$ events.

A measure of reliability of the vertex fit are the pull distributions of the vertex coordinates. The pull is defined as the difference between the reconstructed and the true vertex coordinate, divided by the estimated error on the coordinate. Figure 6.11 shows the pull distribution of the vertex coordinates as obtained with the mass constrained vertex fit. For comparison, figure 6.12

shows the same distributions obtained with the Billoir method. The Gaussians fitted to the pull distributions have, for both vertex fitting methods, a width that is significantly above one, indicating that the errors of the vertex fits were underestimated. It can also be seen that the vertex pull distribution of the mass constrained vertex fit are significantly wider as those for the Billoir method, implying that the errors were more severely underestimated by the mass constrained fit since the vertex resolution was the same for both fitters. This needs to be further investigated.

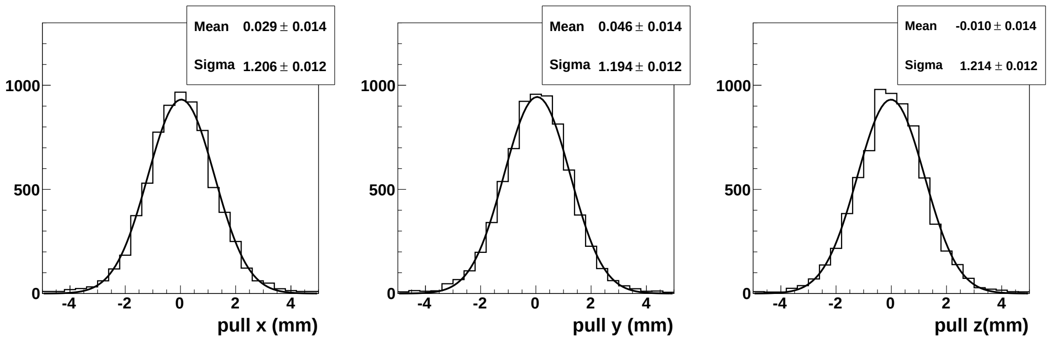

Figure 6.11: Pull distributions of the vertex coordinates for simulated $b\bar{b} \rightarrow X + (J/\psi \rightarrow \mu^+\mu^-)$ events, as obtained with the kinematic vertex-fit with mass constraint. All the distributions are fitted with a single Gaussian.

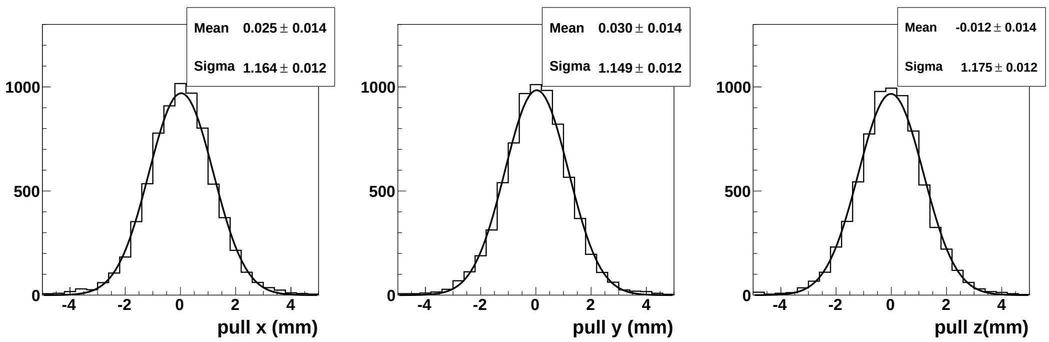

Figure 6.12: Pull distributions of the vertex coordinates for simulated $b\bar{b} \rightarrow X + (J/\psi \rightarrow \mu^+\mu^-)$ events, as obtained with the Billoir method for vertex fitting. All the distributions are fitted with a single Gaussian.

6.5.2 Track parameters at vertex

The updated track parameters at the vertex obtained by both the Billoir method and the mass constrained vertex fit are compared with the true track parameters from the simulated events to obtain the track parameter resolutions shown in figure 6.13. The results show that the addition of a mass-constraint in the vertex-fit helps to improve the measurement of q/p_T of the tracks. The other track-parameters are determined with a similar precision as with the Billoir method and are not significantly affected by the mass constraint.

It can be noted that the use of a mass constraint improves the resolution of q/p_T of the muon track by 20-25% over the whole momentum range. This improvement is a direct result of the mass constraint that constrains the possible momenta of the tracks to the true invariant mass of the J/ψ.

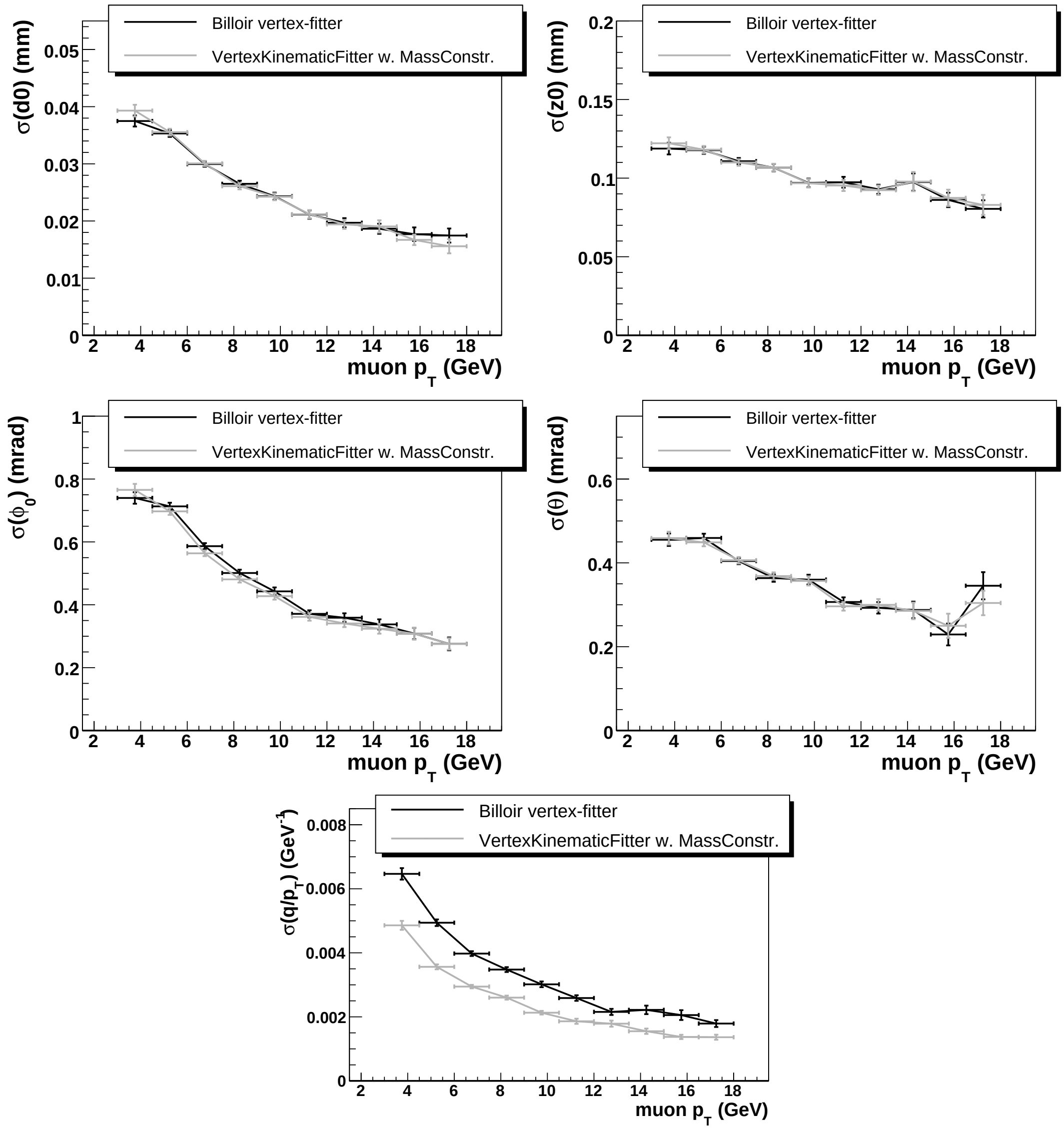

Figure 6.13: Resolutions of the reconstructed track parameters at the vertex as a function of the transverse track-momenta, as obtained with the two vertex fitting methods using simulated $b\bar{b} \to X + (J/\psi \to \mu^+\mu^-)$ events.

Figure 6.14 shows the distribution of the pull of q/p of the updated track parameters obtained with the different fit methods. The width of the pull of q/p using the mass-constraint is slightly increased from 1.30 to 1.34, which is most likely caused by the error on q/p being underestimated in the first place. The widths of the pull distribution for d_0, ϕ and θ are 1.2 for both fitters.

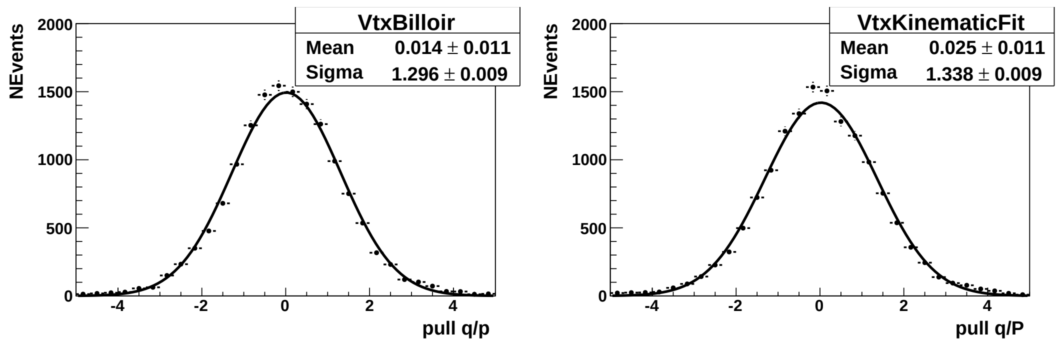

Figure 6.14: Pull distributions of q/p of the track parameters at the vertex obtained with the Billoir method (left) and the vertex fit with mass constraint (right) using simulated $b\bar{b} \to X + (J/\psi \to \mu^+\mu^-)$ events.

6.6 Conclusion

A tool for kinematically constraining a vertex fit in ATLAS was developed. This tool is based on minimization of the χ^2 with Lagrange multipliers in the Cartesian frame. This method allows any constraint that can be formulated as function of the Cartesian track parameters at the vertex position to be included in the vertex fit. The tool has been designed for use within the offline reconstruction and physics analysis algorithms and provides a general interface for vertex fitting with kinematic constraints. The constraints are implemented as independent modules which makes the addition of other constraints simple and flexible.

In a sample of simulated $b\bar{b} \to X + (J/\psi \to \mu^+\mu^-)$ events it has been shown that the use of a mass constraint improves the momentum resolution of the track parameters at the vertex while achieving similar results for the vertex resolution and resolution of the other track parameters as obtained with the Billoir method for vertex fitting.

Chapter 7

Weak mode misalignments in $J/\psi \rightarrow \mu^+\mu^-$ events

The knowledge of the exact position of the detector elements in ATLAS determines the resolution with which a particle trajectory can be reconstructed. Uncertainties in the positions of the detector elements in ATLAS are present due to the limited precision from the building and installation of the detectors and as a result of movements over time. Alignment algorithms use the information of the hit residuals of a large numbers of tracks to estimate with high precision the shifts of the detector elements relative to their nominal position. Certain types of systematic shifts of the detector elements, so-called 'weak mode' misalignments, can not be solved by these standard alignment algorithms working with hit residuals. The weak modes introduce a significant bias in the reconstructed momenta of the measured particles while leaving the hit residuals unaffected. This chapter shows how the use of a mass constraint in $J/\psi \rightarrow \mu^+\mu^-$ events can be used to correct biases in the reconstructed momenta induced by weak mode misalignments.

7.1 Inner detector alignment

To fully profit from the performance of the ATLAS inner detector, the best possible knowledge of the position of the detector elements is essential. The "as-built" precision is $\mathcal{O}(100)$ μm as determined from survey data of the inner detector before installation in the ATLAS cavern. The module positions need to be determined with a precision of approximately 10 μm or better in the bending plane [24], to ensure that the misalignment of silicon modules does not inflate the track parameter uncertainties by more than 20% above the intrinsic resolution at high p_T. For precision measurements, such as for example the mass of the W-boson, an understanding of the module positions at the level of 1 μm or better is required.

After assembly and survey, a nominal detector geometry is used to represent the best knowledge of the module positions. Subsequent alignment parameters quantify the change in position and rotation of the detector elements over time, relative to the nominal detector geometry. The track-based alignment procedure [65] uses a large sample of tracks to determine the alignment parameters that minimize the hit residuals.

Another way to monitor movements of the detector elements uses a hardware-based alignment procedure. Hardware alignment is available in the SCT, which has been equipped with a Frequency Scanning Interferometry (FSI) optical alignment system [66]. The FSI system is capable of monitoring micron-scale motions of the detector on a time scale as short as 10 minutes. Although this system can not derive the full set of alignment constant needed to determine the exact module position, it complements the track-based alignment by providing information of movements of the detector elements over time.

7.1.1 Track-based alignment

The track-based alignment algorithms have the task to determine and update the alignment parameters. For the ATLAS inner detector, the smallest components that are aligned are the numerous detector modules: 1744 pixel modules, 4088 SCT modules and 136 TRT modules. Six alignment parameters are defined for each detector element: three for their position and three for their rotations, so that aligning the detector leads to solving a system with 35,808 degrees of freedom.

Alignment parameters for the inner detector are derived from a dedicated stream of tracks, selected at a rate of ∼10 Hz, which means that the alignment parameters can be updated every 24 hours. To reach a precision of 10 μm on the silicon-module positions, approximately one million tracks with various topologies have to be selected within this 24 hour period and written out to the calibration and alignment stream.

Several different alignment methods are available in ATLAS [65] to obtain a set of updated alignment parameters. The main ingredient for track-based alignment approaches is that for a perfectly aligned detector all the hit residual distributions are centered around zero with a width determined by multiple scattering and the intrinsic detector resolution. The global χ^2 method [67] is one example of a track-based alignment method that obtains the alignment parameters by minimizing the sum of χ^2-values of a large number of tracks.

7.1.2 Alignment results using cosmic tracks

At the time of writing this thesis, no LHC collisions were available to provide a track sample for alignment. However, using tracks measured in events from cosmic muons intersecting the detector, a first attempt to determine the alignment parameters was made. Figure 7.1 shows the residual distribution in the precision coordinate as measured in SCT barrel modules, using the nominal geometry and the aligned geometry [68]. It can be seen that the original "as-built" precision (without alignment) is 182 μm and that after alignment the width of the residual distributions is reduced to 28 μm, very close to the intrinsic resolution of the silicon strips of 23 μm.

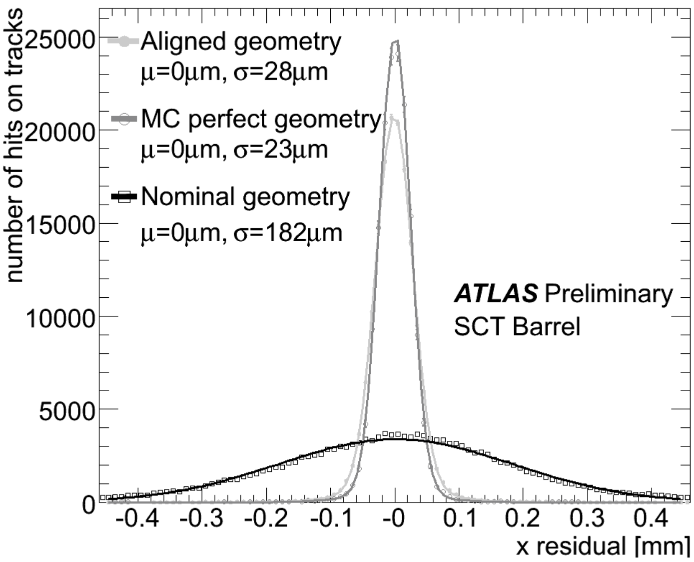

Figure 7.1: Residual distribution in the precision coordinate as measured in the SCT barrel modules, integrated over all hits-on-tracks in the SCT barrel for the nominal geometry and the preliminary aligned geometry [68].

7.1.3 Alignment results using simulated data

A realistic 'data challenge' [16], using millions of simulated events, was made to check the performance of the various algorithms in ATLAS. Within the context of this data challenge the inner detector alignment algorithms were tested using simulated events with a misaligned detector geometry. The misaligned geometry introduced a number of systematic displacements and rotations of large and smaller-scale structures on top of a smaller random misalignments at the module level. The alignment algorithms used this data to obtain an aligned geometry of the inner detector, based on high-p_T muons and cosmic rays. The study showed that after the alignment residual distortions of the detector geometry remained [16], which were observed to be much smaller in the barrel than in the end-cap region of the inner detector. This can be explained by the presence of cosmic tracks in the alignment sample, that pass mostly through the barrel region and can remove some of the effects of the systematic displacement of the detector.

Figure 7.2 shows the reconstructed di-muon mass in $Z \to \mu^+\mu^-$ events after alignment, as well as the result obtained without misalignment ('Ideal layout'). After alignment the Z mass resolution is 3.9 GeV [1], compared to a resolution of 2.6 GeV for a perfectly aligned detector [16]. The difference between the aligned and ideal layout indicate the presence of residual alignment distortions after the first-pass alignment.

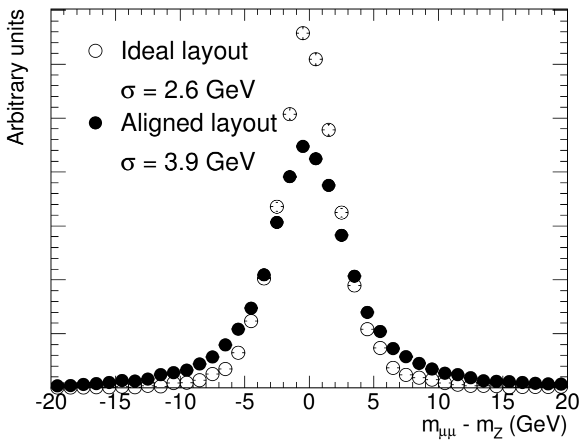

Figure 7.2: Difference between the reconstructed and true mass of di-muon pairs, as obtained from simulated $Z \to \mu^+\mu^-$ events with a perfectly aligned (ideal) inner detector and for the aligned inner detector using the results from the ATLAS alignment algorithms [16].

A measure of the residual distortions is extracted, as will be done with real data, by searching for possible asymmetries between the p_T-spectra of negative and positive muons in $Z \to \mu^+\mu^-$ events. This is illustrated in figure 7.3 which clearly demonstrates a significant charge asymmetry in the events obtained in the aligned geometry. The charge asymmetry indicates a shift in the reconstructed curvature as a result of "left over" systematic deformations of the detector geometry. These systematic deformations are not (or only weakly) constrained by the minimization of the hit residuals and are commonly referred to as *weak mode misalignments*. These types of misalignments are discussed in the next section.

7.2 Weak mode misalignments

Weak modes represent systematic deformations of the detector which affect the reconstructed track parameters but are not (or only weakly) corrected by

[1]It should be noted that a width of 3.9 GeV is an impressive result, given that the Z peak was not even visible before alignment.

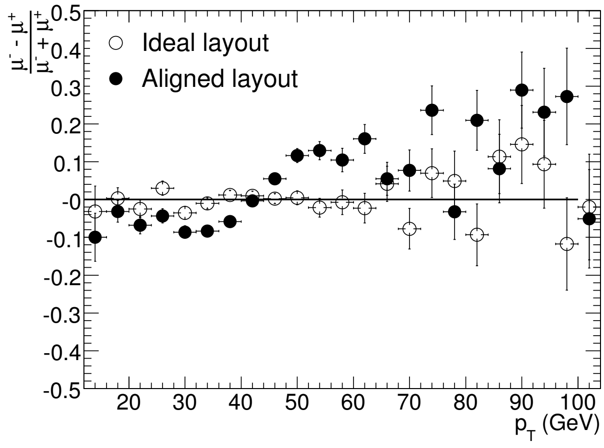

Figure 7.3: Asymmetry between negative and positive muons as function of p_T, as obtained from simulated $Z \to \mu^+\mu^-$ events with a perfectly aligned (ideal) inner detector and for the aligned inner detector using the results from the ATLAS alignment algorithms [16].

minimization of the hit residuals from tracks that originate from the interaction point. Figure 7.4 illustrates a weak mode misalignment where the shift in the ϕ-coordinate increases as function of R, which results in an incorrect curvature reconstruction. These detector shifts do not change the hit residuals significantly and thus would not be corrected by the standard alignment procedure based on minimization of the residuals.

The existence of weak modes is a result of the cylindrical symmetry of the detector in combination with using tracks that originate from the interaction point. When using a large set of tracks that originate from the center of the detector, the standard alignment procedure settles on a geometry that minimizes the hit residuals in which a systematic detector deformation can remain.

The cylindrical symmetry of the ATLAS detector results in nine different weak modes, based on the correlation between the cylindrical detector coordinates: R, ϕ and Z. Table 7.1 summarizes the different types of weak modes that are based on a shift of the detector position in one of the cylindrical coordinates as function of one of the coordinates.

The presence of weak modes in the detector geometry lead to a bias on the reconstructed track parameters, so eliminating weak modes is of vital importance for achieving the full physics potential of ATLAS. Using tracks that are not originating from the interaction point, such as cosmic-ray tracks or tracks from the beam halo, help to eliminate certain weak modes. However, compared to the number of tracks produced in proton-proton collision events, the statistics of these types of tracks are limited and do not cover the full inner

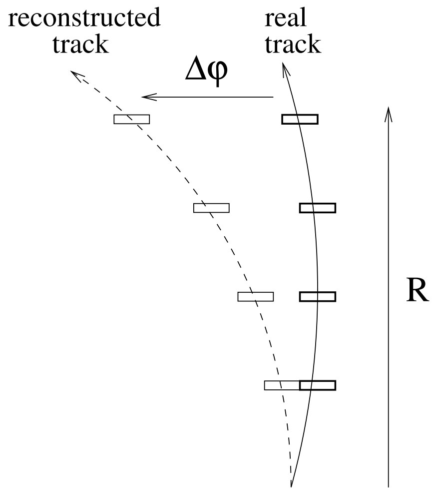

Figure 7.4: Illustration of the effect of a weak mode misalignment where the detector elements are moved by $\Delta\phi$ as a function of their radial distance of the interaction point. The hit residuals of the reconstructed track (dashed line) are not increased by the position shifts, but its curvature is different from the real track.

	ΔR	$\Delta\phi$	ΔZ
R	Radial expansion	Curl	Telescope
ϕ	Elliptical	Clamshell	Skew
Z	Bowing	Twist	Z expansion

Table 7.1: Naming convention for the nine types of weak modes in ATLAS. ΔR, $\Delta\phi$ and ΔZ indicate the cylindrical coordinate that is shifted and R, ϕ and Z indicate the cylindrical coordinate to which the shift is proportional.

detector geometry[2].

Another way to constrain weak mode misalignments is by using track pairs from well-known decays, for example Z or J/ψ to two muons. Fitting these tracks to a common decay vertex and a known invariant mass provides sensitivity to systematic correlations between different detector elements.

This chapter focuses on the study of weak mode misalignment using a mass constrained vertex fit in $J/\psi \to \mu^+\mu^-$ events.

[2]Cosmic muons are almost exclusively reconstructed in the barrel and the beam halo tracks are only reconstructed in the very forward detector region.

7.2.1 Effect of weak modes on J/ψ mass

A mass constrained vertex in $J/\psi \to \mu^+\mu^-$ events only helps to correct weak modes that affect the reconstructed invariant mass of the J/ψ. For this reason, a simple toy model was developed to study the various weak modes and to assess which have a significant effect on the reconstructed invariant mass.

The toy model simulates two tracks with an invariant mass equal to the J/ψ mass. Measurements of each track are simulated as the intersection points of the track with a set of 10 cylinders. The radius of the cylinders are chosen so that they represent the actual ATLAS inner detector geometry: three cylinders represent the pixel barrel layers, four cylinders represent the SCT barrel layers and three cylinders are used to represent measurement at the inner, middle and outer radius of the TRT barrel. In reality, the TRT modules provide many more measurement points, but within the toy model this approximation is sufficient. Figure 7.5 shows an example of two tracks and their measurements as simulated by the toy model.

The intersection points are calculated using the assumption of a solenoidal

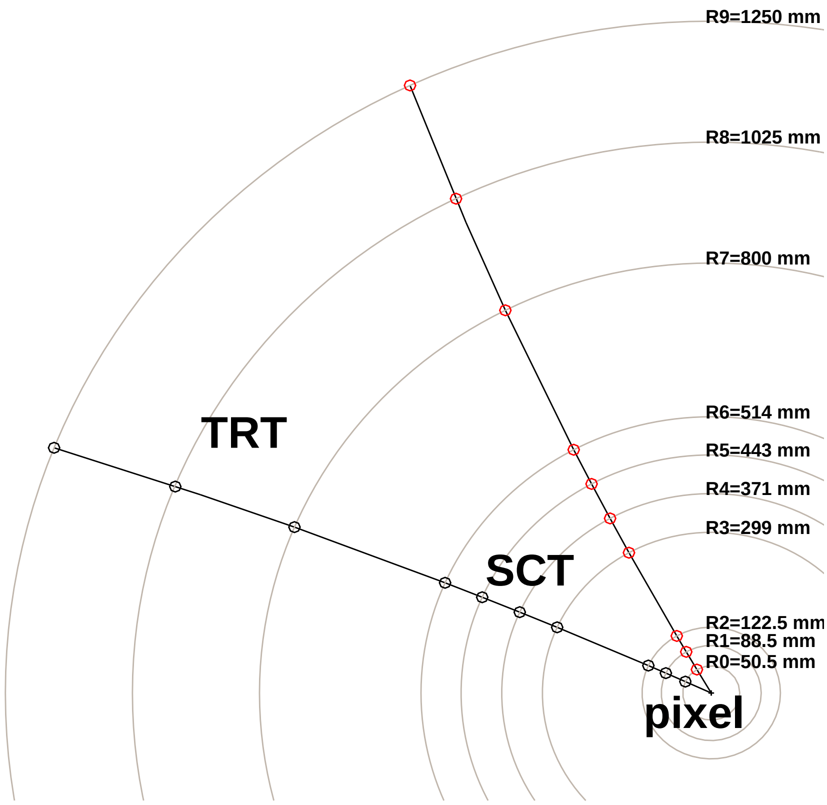

Figure 7.5: XY-display of a $J/\psi \to \mu^+\mu^-$ event simulated by the toy model. The circles indicate the intersection points of the generated track with the 10 cylinders that are used as a simplified representation of the inner detector.

magnetic field of 2 T, so that the simulated track represents a helix curving in the XY-plane. The toy model uses the intersection points as measurements from which the muon track parameters are reconstructed. Without misalignment the results of model confirmed that the momenta (and invariant di-muon mass) is reconstructed correctly. In this configuration the toy model represents a 'perfect' detector.

Systematic shifts are applied in the toy model, for example $\Delta\phi = c \cdot R$ to simulate a 'curl' misalignment, after which the shifted hit positions are used to reconstruct the muon track parameters. Each shift is multiplied by a scale-factor so that the shift ΔM of the reconstructed J/ψ mass can be studied as function of the amount of misalignment that is applied to the system. A scale-factor of 1.0 corresponds to a 'reasonable' misalignment of the detector where the maximum shift of an SCT module is 200 μm[3].

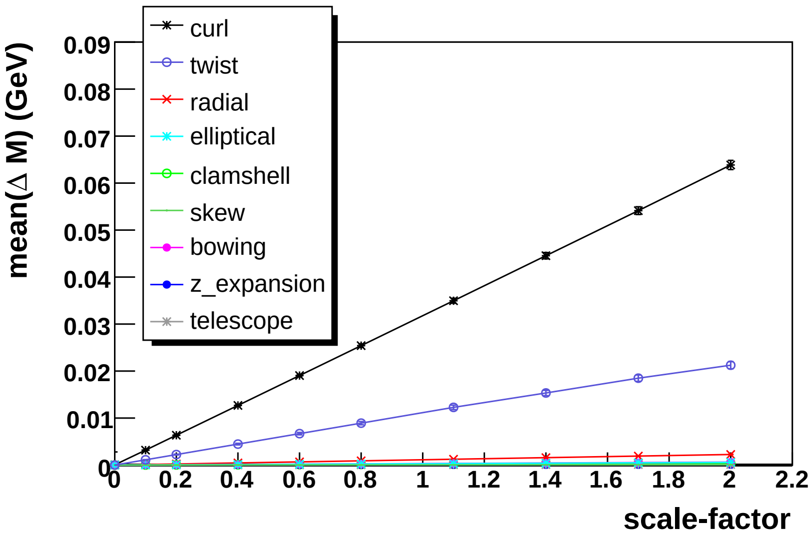

Figure 7.6: Average shift in mass as a function of scale-factor in the nine different weak modes as predicted by the toy model simulating $J/\psi \to \mu^+\mu^-$ events. Scale-factor = 1 corresponds to a maximum shift of 200 μm of the outermost SCT modules.

Figure 7.6 shows the average shift in the reconstructed J/ψ mass as a function of scale-factor in the nine different weak modes as predicted by the toy model. The figure shows that 'curl' and 'twist' are weak modes that affect the reconstructed J/ψ mass the most, with an average mass shift of 5-10 MeV at scale-factor=1.

Curl and twist are both weak modes that shift the hit positions in ϕ, so that an effect on the reconstructed curvature of the tracks was to be expected. Other types of weak modes may introduce measurable biases in other reconstructed

[3] The "as-built" precision was seen to be of the order 200 μm, so weak modes where shifts of the detector elements are greater than this are unlikely to occur.

track parameters (such as the impact parameter, d_0) but these can not be corrected using a mass constrained vertex fit. For this reason the rest of this chapter will focus on studying $J/\psi \to \mu^+\mu^-$ events reconstructed with a 'curl' or 'twist' misalignments in the ATLAS inner detector.

7.2.2 Simulation of weak modes in ATLAS

The remainder of this chapter shows results obtained with Monte Carlo samples produced using a full simulation of the ATLAS detector response with generated $J/\psi \to \mu^+\mu^-$ as input. The generated events were required to have both muons in the region $|\eta| < 2.5$ and one muon with p_T >9 GeV, to simulate events that will be selected by the single muon trigger in ATLAS.

Sets of alignment parameters are available to introduce specific weak modes in the detector [69] during the event reconstruction. In these sets, the alignment parameters that simulate the curl and twist weak mode were chosen such that the maximum shift of an outermost SCT barrel module is 200 μm, similar to what was used in the toy model[4]. The realistic detector simulation can not create a perfect weak mode misalignment in the detector as the alignment parameters provide limited degrees of freedom for shifting the hit positions [69]. For example one TRT module contains multiple hit positions and the alignment parameters allow only the TRT module as a whole to be shifted/rotated. Nevertheless, the weak mode geometry in the full simulation samples are expected to produce approximately the same effects as observed with the toy model.

7.3 Curl misalignment

The curl misalignment is expected to result in a reconstruction bias in q/p_T of the tracks which subsequently leads to an effect in the reconstruction of the invariant mass. The reconstruction bias introduced by the curl misalignment will first be quantified, after which the results using a mass constrained vertex fit will be discussed.

7.3.1 Reconstruction bias

Figure 7.7 shows the difference between the reconstructed and true value of q/p_T of the tracks reconstructed with and without the curl misalignment in the simulated ATLAS samples. The resolution of q/p_T decreases with increasing value of p_T, so a cut on minimum p_T of 9 GeV was applied to make the reconstruction bias more clearly visible. The curl misalignment is observed to

[4]The toy model was in fact based on the proposed maximum shift of the alignment group.

introduce a shift in the reconstructed value of q/p_T that is equal to $(-2.24 \pm 0.05) \cdot 10^{-3}$ GeV^{-1}.

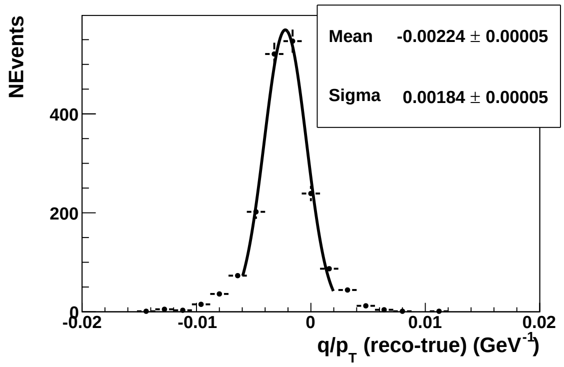

Figure 7.7: Difference between the reconstructed and true value of q/p_T of the inner detector tracks in $J/\psi \to \mu^+\mu^-$ events with a curl misalignment in the detector, result shown for all tracks with $p_T > 9$ GeV.

A bias in the reconstructed value of q/p_T of the tracks will affect the reconstructed invariant mass. However, if the negative and positively charged muons have the same transverse momentum they each get an equal but opposite shift in their transverse momentum so that the reconstructed mass is practically unchanged. For this reason the effect of the curl misalignment on the reconstructed mass was studied as a function of the p_T difference of the muons from the J/ψ decay.

Figure 7.8 shows the reconstructed di-muon mass as a function of the p_T difference between the positively and the negatively charged muon for events reconstructed with and without the curl misalignment. It can be seen that the introduction of curl misalignment in the detector geometry results in an approximately linear dependency of the reconstructed mass versus the muon p_T difference. The results of the curl misalignment obtained with the realistic detector simulation show an excellent agreement with the prediction from the toy-model. Figure 7.8 also shows the χ^2 distribution for fitted tracks with and without curl misalignment. The χ^2 distribution is not greatly changed by using the curl geometry, indicating that a true weak mode was introduced in the detector geometry.

7.3.2 Mass constrained fit results

The use of the mass constrained vertex fit to remove the q/p_T shift introduced by the curl misalignment was studied using $J/\psi \to \mu^+\mu^-$ events. The resolution of the reconstructed value of q/p_T depends on the transverse momentum p_T of the muon tracks. For this reason the difference between the reconstructed

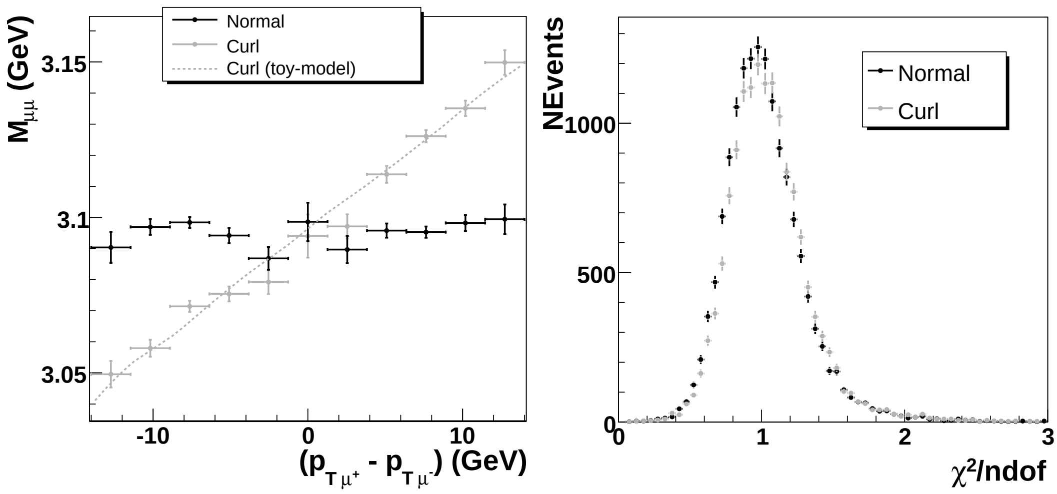

Figure 7.8: Effects of curl misalignment: (left) Reconstructed di-muon mass as a function of the p_T difference between the positive and the negative muon and (right) χ^2 per degree of freedom, for tracks reconstructed in the inner detector.

and the true value of q/p_T was studied at various intervals of p_T. The resolution of q/p_T is defined as the width of a Gaussian fit to these distributions and the average shift in q/p_T is quantified by the mean of the fits.

Figure 7.9 shows the resolution and average q/p_T shift as a function of the transverse momentum of tracks reconstructed with the curl misalignment. The first plot shows that the resolution of both fitters decreases for tracks with lower p_T values. The result of the default vertex fitter in the right-hand plot shows that the shift in q/p_T is more or less constant as function of the transverse momentum of the track, while after the mass constrained vertex fit the average shift in q/p_T of the reconstructed tracks depends strongly on the transverse momentum of the tracks.

This difference in behavior can be explained as follows: Since the fit is required to minimize a χ^2-function that includes the errors of the original track fit, the fit attempts to satisfy the mass constraint by applying a bigger correction on the q/p_T of the lower p_T track, as it has the largest error. For tracks with $p_T > 9$ GeV, figure 7.9 shows that the shift in q/p_T is closer to zero when using the mass constrained fit, indicating that for these tracks the q/p_T shift introduced by the curl misalignment is partially recovered.

In order to improve the results obtained with the mass constrained vertex fit, the fit is repeated after increasing the error of the curvature of the tracks with an additional value of $0.03{\cdot}10^{-3}$ GeV^{-1}. This error is huge in comparison to the actual error of the momentum fit, as can be seen from the resolution-plot in figure 7.9, so it essentially gives the mass constrained vertex fit a much larger freedom to alter the curvature of both tracks. Figure 7.10 shows the

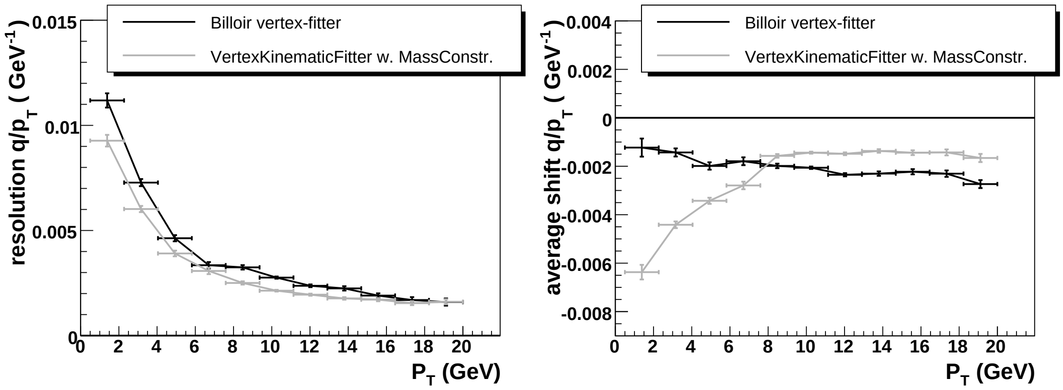

Figure 7.9: Resolution (left) and average shift (right) of q/p_T of the track parameters at vertex versus the transverse momentum, obtained with the two vertex fitting methods.

results in resolution and average shift of q/p_T as a function of the transverse momentum when using this error-scaling in the mass constrained vertex fit. The addition of the error-scaling allows most of the q/p_T shift to be recovered for tracks with $p_T > 9$ GeV, while for tracks with lower p_T the average shift in q/p_T remains close to its original value.

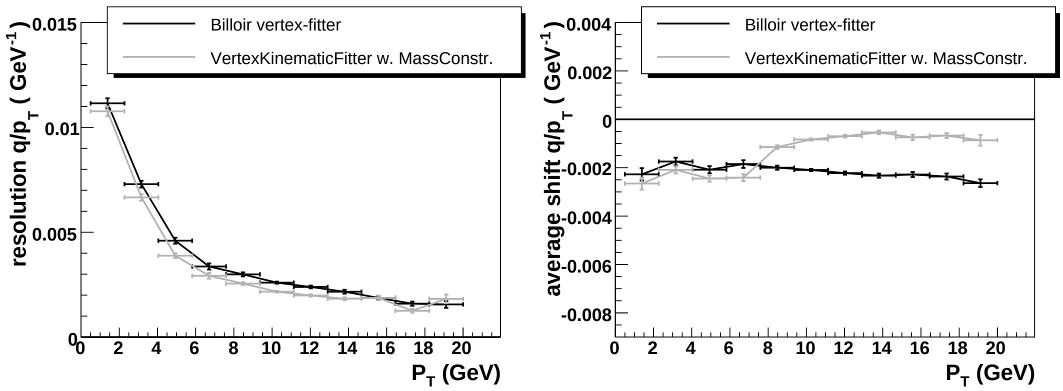

Figure 7.10: Resolution (left) and average shift (right) of q/p_T of the track parameters at vertex versus the transverse momentum obtained with the two vertex fitting methods, using very large errors for q/p of the input track parameters in the mass constrained vertex fit.

7.4 Twist misalignment

The 'twist' weak mode shifts the measured position in $\Delta\phi$ as a function of z. This results in a bias of the curvature of tracks, with the value of the bias depending on the angle θ of the tracks. For tracks coming from the interaction point, the Z-position of a measurement along the track can be related to the radial position R by: $\frac{R}{Z} = \frac{\sin\theta}{\cos\theta} = \tan\theta$. Shifts of the detector elements in $\Delta\phi$ versus R (curl) were demonstrated to create a bias in the reconstructed value of q/p_T, so for twist misalignment the expected effect is a shift in $\frac{q}{p_T} \times \tan\theta$. Since $p_T/p_Z = \tan\theta$, the twist misalignment creates a bias in the reconstructed value of q/p_Z.

7.4.1 Reconstruction bias

Figure 7.11 shows the difference between the reconstructed and true value of q/p_Z of the tracks reconstructed with and without the twist misalignment for tracks with a minimum p_Z of 15 GeV. The twist misalignment is observed to introduce a bias in the reconstructed value of q/p_Z of (-0.97±0.03)·10^{-3} GeV^{-1}.

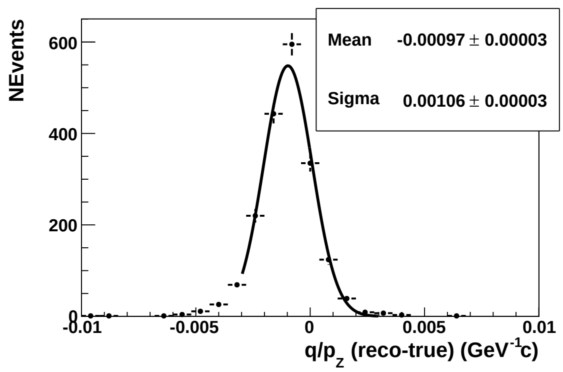

Figure 7.11: Difference between the reconstructed and true value of q/p_Z of the inner detector tracks in $J/\psi \to \mu^+\mu^-$ events with a twist misalignment in the detector, result shown for all tracks with $p_Z > 15$ GeV.

In the same way as the curl misalignment leads to a mass dependency on the muon p_T difference, the twist misalignment leads to a mass dependency on the p_Z difference of the two muons from the J/ψ decay. Figure 7.12 shows the effects of the twist misalignment on the reconstructed invariant mass as function of the p_Z difference of the muons and also shows the χ^2 per degree of freedom of the reconstructed tracks. The effect on the reconstructed J/ψ mass obtained with the realistic ATLAS simulation shows an excellent agreement with the linear dependence predicted by the toy model. It can be seen that the χ^2 of the fitted tracks is not significantly changed by the twist geometry, indicating that a true weak mode was introduced to the detector geometry.

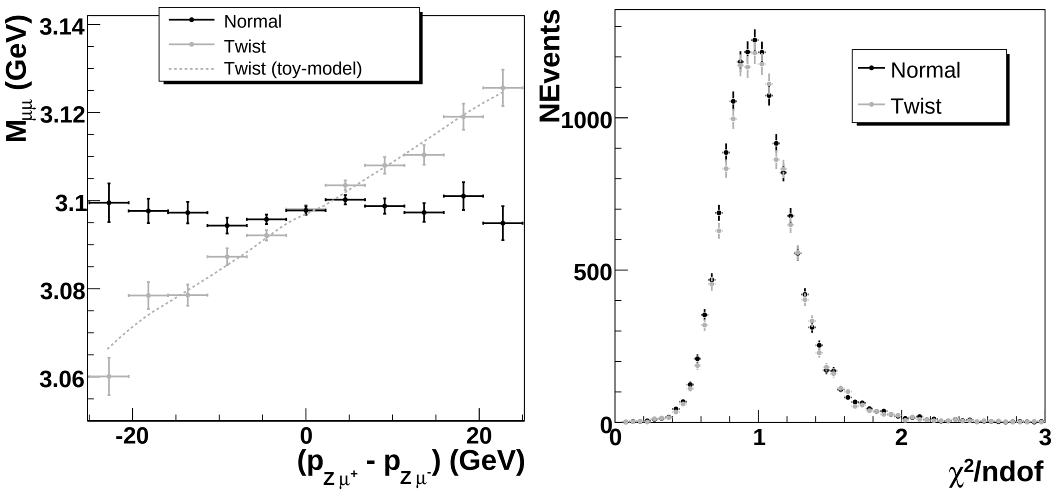

Figure 7.12: Effects of twist misalignment: (left) Reconstructed di-muon mass as a function of the p_Z difference between the positive and the negative muon and (right) χ^2 per degree of freedom, for tracks reconstructed in the inner detector.

7.4.2 Mass constrained fit results

The use of the mass constrained vertex fit for removing the q/p_Z shift induced by the twist misalignment was studied. Figure 7.13 shows the resolution and average q/p_Z as a function of p_Z of the reconstructed tracks with and without using a mass constraint, as obtained using $J/\psi \to \mu^+\mu^-$ events with the twist misalignment. The left-hand plots shows that the uncertainty of the reconstructed value of q/p_Z is much higher for tracks with low p_Z values. The right-hand plot in figure 7.13 shows that, similar as was seen in the results for the curl misalignment, the fit 'prefers' to satisfy the mass constraint by only altering the q/p_Z of the track with the highest error.

As for the curl misalignment, the results can be improved by performing the mass constrained fit after increasing the error of the curvature of the tracks with an additional 0.03 GeV^{-1}. Figure 7.14 shows the results in resolution and average shift of q/p_Z as a function of the transverse momentum when using this error-scaling in the mass constrained vertex fit. The mass constrained fit with error-scaling is observed to partially remove the q/p_Z shift over the whole range of p_Z of the muon tracks. A significant amount of q/p_Z shift remains even with the mass constrained fit with error-scaling. This is mostly due to events where the muons had a small p_Z difference, where the J/ψ mass was not significantly effected and the mass constraint fit was unable to correct the curvature bias.

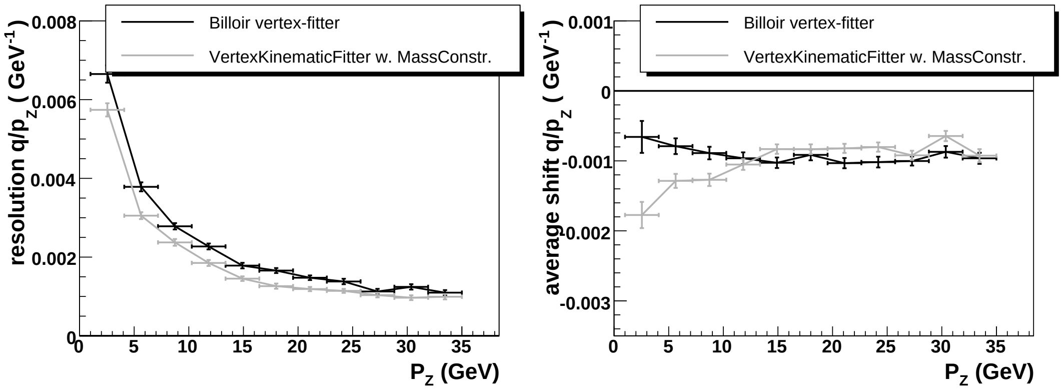

Figure 7.13: Resolution (left) and average shift (right) of q/p_Z of the track parameters at vertex versus the z-component of the track momentum, obtained with the two vertex fitting methods.

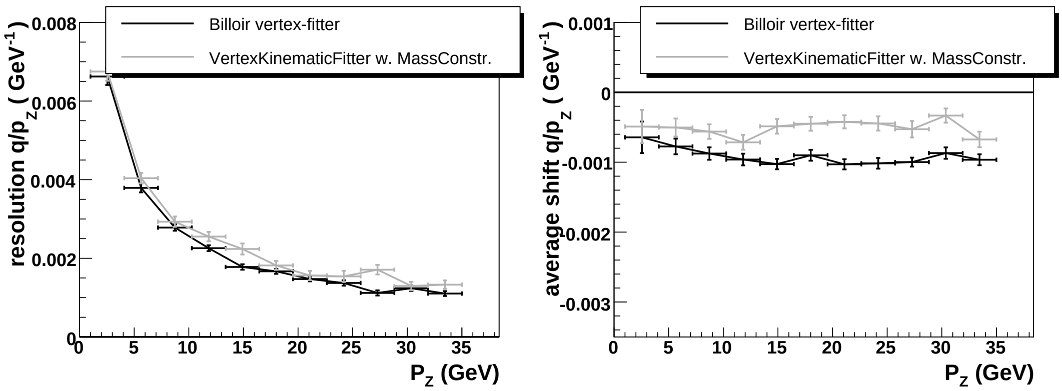

Figure 7.14: Resolution (left) and average shift (right) of q/p_Z of the track parameters at vertex versus the z component of the momentum obtained with the two vertex fitting methods, using very large errors for q/p of the input track parameters in the mass constrained vertex fit.

7.5 Measuring weak mode effects

Based on the result in the previous section, the mass constrained vertex fit appears capable of (partially) correcting the reconstructed bias in q/p_T and q/p_Z induced by the weak mode misalignments. This facilitates the measurement of a possible reconstruction bias by looking at the difference between the reconstructed q/p_T and q/p_Z obtained with and without a mass constraint in $J/\psi \to \mu^+\mu^-$ events.

Figure 7.15 shows the difference in the value of q/p_T shift obtained with unconstrained and mass constrained vertex fits in simulated $J/\psi \to \mu^+\mu^-$ events reconstructed with the curl misalignment. Both the results using the standard mass constrained vertex fit and the mass constrained vertex fit with increased errors on q/p are shown. By using increased errors on q/p during the vertex-fit some of the information obtained by the original track-fit is discarded, which would explain the increased width observed in the right-hand plot of figure 7.15.

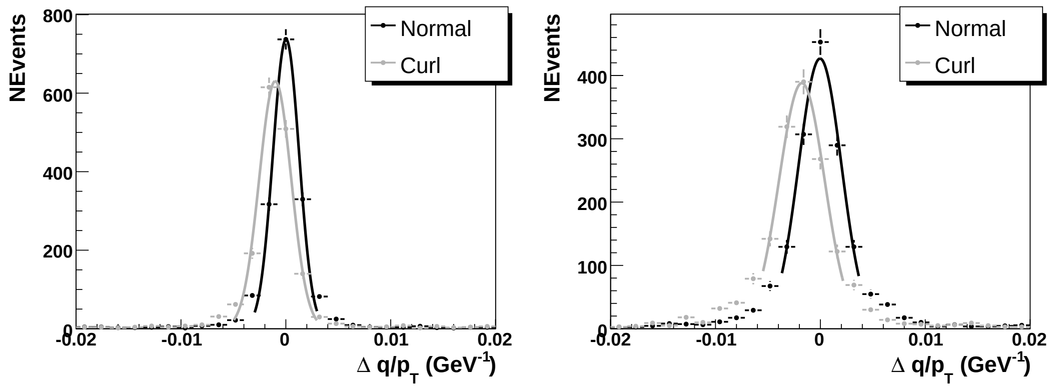

Figure 7.15: Difference between q/p_T obtained with the unconstrained and mass constrained vertex fit in $J/\psi \to \mu^+\mu^-$ events reconstructed with curl misalignment. Plots were obtained without error-scaling (left) and with error-scaling (right). Values of the Gaussian fit parameters are given in tables 7.2 and 7.3.

The mean of the Gaussian fitted in figure 7.15 depends on the selection cuts on the p_T of the plotted tracks as well as on the p_T difference between the two muon tracks in the $J/\psi \to \mu^+\mu^-$ event. The mass dependency on the muon p_T difference, induced by the curl misalignment (demonstrated in figure 7.8), means that the mass constrained fit works better for increasing values of the p_T difference. To optimize the measurement of the curvature bias the minimum p_T of the plotted track was 9 GeV while the minimum p_T difference between the two muons was 8 GeV.

Similarly, figure 7.16 shows the measurement of the q/p_Z-shift in $J/\psi \to \mu^+\mu^-$ events reconstructed with twist misalignment. To optimize the measurement of the bias in q/p_Z, the minimum p_Z of the plotted tracks was 10 GeV and the minimum p_Z difference between the muons was 10 GeV.

The reconstruction bias in q/p_T and q/p_Z can be determined from the mean of the Gaussian fit of the distributions in figures 7.15 and 7.16. The mean and width of the fitted distributions obtained using $J/\psi \to \mu^+\mu^-$ events reconstructed with the normal, curl and twist geometry are shown in table 7.2 (for the standard mass constrained fit) and in table 7.3 (for the mass constrained fit using with error-scaling in q/p).

An interesting observation is that the twist misalignment does not introduce a measurable bias in q/p_T and, similarly, the curl misalignment does not introduce a measurable bias in q/p_Z. This shows that the two types of weak

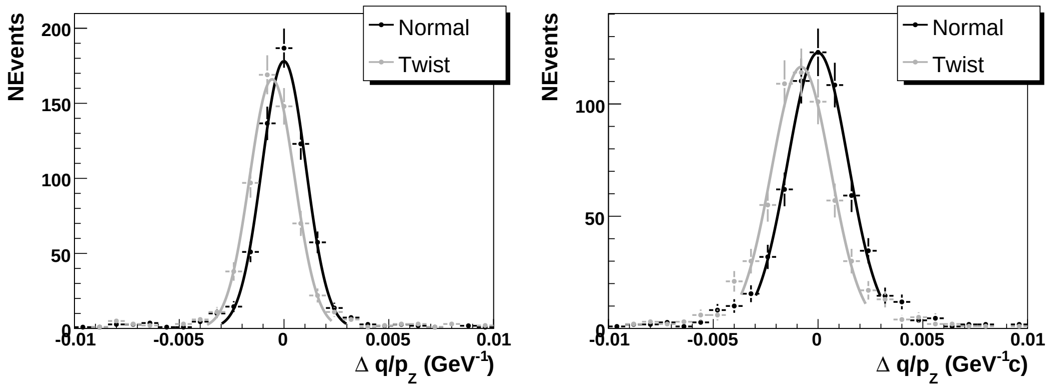

Figure 7.16: Difference between q/p_Z obtained with the unconstrained and mass constrained vertex fit in $J/\psi \to \mu^+\mu^-$ events reconstructed with twist misalignment. Plots were obtained without error-scaling (left) and with error-scaling (right). Values of the Gaussian fit parameters are given in tables 7.2 and 7.3.

Geometry	$\Delta q/p_T$ (10^{-3} GeV^{-1})		$\Delta q/p_Z$ (10^{-3} GeV^{-1})	
	mean	σ	mean	σ
Normal	-0.02±0.04	1.24±0.04	-0.00±0.05	1.05±0.04
Curl	-1.01±0.04	1.53±0.04	-0.04±0.06	1.31±0.06
Twist	-0.01±0.04	1.31±0.06	-0.57±0.05	1.07±0.04

Table 7.2: Mean and σ from a Gaussian fit to the distribution of the difference of q/p_T and q/p_Z obtained with the unconstrained and mass constrained vertex fit (using the cuts described in the text).

Geometry	$\Delta q/p_T$ (10^{-3} GeV^{-1})		$\Delta q/p_Z$ (10^{-3} GeV^{-1})	
	mean	σ	mean	σ
Normal	-0.03±0.06	2.04±0.06	-0.00±0.07	1.44±0.07
Curl	-1.76±0.07	2.17±0.08	-0.01±0.11	1.84±0.15
Twist	-0.03±0.06	2.15±0.07	-0.80±0.07	1.42±0.08

Table 7.3: Mean and σ from a Gaussian fit to the distribution of the difference of q/p_T and q/p_Z obtained with the unconstrained and mass constrained vertex fit with increased error on q/p of the input track parameters (using the cuts described in the text).

modes can be treated independently.

The real reconstruction bias in q/p_T induced by the curl misalignment was shown (see section 7.3.1) to be equal to (-2.24±0.05)·10^{-3} GeV^{-1}. The percentage of the q/p_T shift that was measured is equal to (-1.01±0.04)·10^{-3} GeV^{-1} without using error-scaling and (-1.76±0.07)·10^{-3} GeV^{-1} with error-scaling. This means that the percentage of the real q/p_T shift that was measured is equal to (45±3)% without using error-scaling and (79±4)% with error-scaling.

For the twist misalignment, the true reconstruction bias in q/p_Z was observed (see section 7.4.1) to be equal to (-0.97±0.03)·10^{-3} GeV^{-1}. The measured q/p_Z shift is equal to (-0.57±0.05)·10^{-3} GeV^{-1} without using error-scaling and (-0.80±0.07)·10^{-3} GeV^{-1} with error-scaling. This means that the percentage of the real q/p_Z shift that was measured is equal to (59±6)% without using error-scaling and (82±8)% with error-scaling.

The measured value of the reconstruction bias is closer to the true value with the error-scaling, but the results in tables 7.2 and 7.3 also show that the errors on the mean $\Delta q/p_T$ and $\Delta q/p_Z$ are larger when using error-scaling. Without error-scaling the amount of curvature recovered by the mass constrained fit depends more strongly on the momenta of the tracks (see figures 7.15 and 7.16). Therefore it is recommended to use error-scaling on q/p in studying these types of misalignments, as the results will be less strongly influenced by the momentum distribution of the selected events.

7.6 Curvature correction in $Z \to \mu^+\mu^-$ events

The presence of the curl or twist weak mode misalignment in the ATLAS inner detector was shown to create a bias on the reconstructed value of q/p_T or q/p_Z. The presence of these curvature biases will affect the resolution of any invariant mass measurement that uses the inner detector tracks.

Figure 7.17 shows the invariant mass of muons from simulated $Z \to \mu^+\mu^-$ events reconstructed with and without the weak mode misalignments[5]. It can be seen that the presence of curl or twist misalignment results in a significant decrease of the mass resolution.

The effect of the reconstruction bias in q/p_T and q/p_Z induced by the curl and twist misalignment can be removed by applying a curvature correction:

$$\begin{aligned} \frac{q}{p_{T\,new}} &= \left(\frac{q}{p_T}\right)_{old} - \Delta_{q/p_T} \\ \frac{q}{p_{Z\,new}} &= \tan\theta \left(\frac{q}{p_T}\right)_{new} - \Delta_{q/p_Z} \end{aligned} \tag{7.1}$$

where Δ_{q/p_T} and Δ_{q/p_Z} are the estimated values of the reconstruction bias.

[5]The results for the reconstructed Z peaks were obtained using information from the inner detector tracks only.

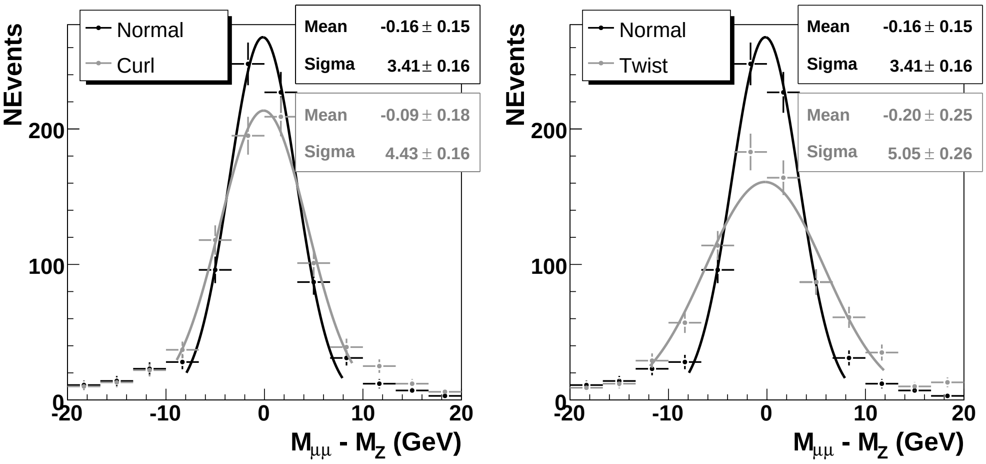

Figure 7.17: Difference between the reconstructed and true invariant mass for simulated $Z \to \mu^+\mu^-$ events reconstructed with curl misalignment (left) and the twist misalignment (right) compared to the result without misalignment (normal).

Figure 7.18 shows the result on the reconstructed Z peak for simulated events reconstructed with the curl and twist misalignment, before and after applying a curvature correction. The curvature correction uses the measured values of Δ_{q/p_T} and Δ_{q/p_Z} (with error-scaling) as given in table 7.3. This way effectively ~80% of the true reconstruction bias is removed. It can be seen that in both cases the width of the Z peak is significantly improved after applying a correction for the reconstruction bias.

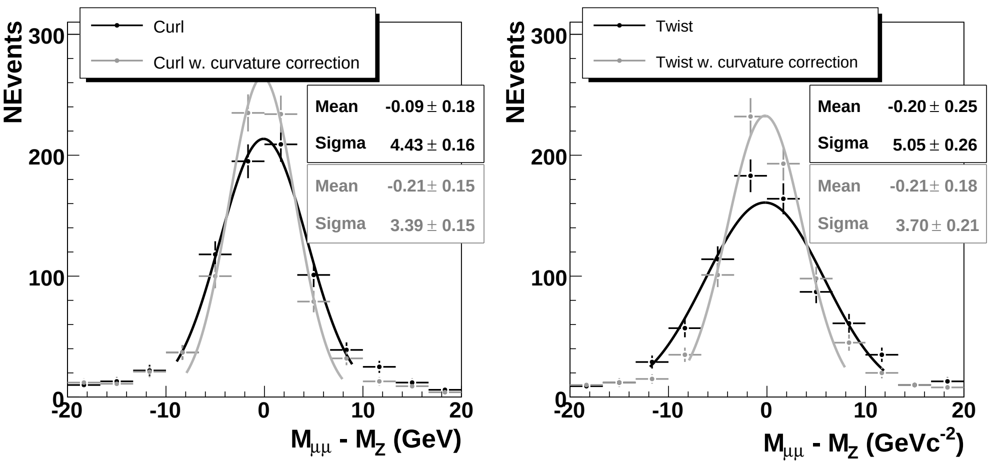

Figure 7.18: Difference between the reconstructed and true invariant mass for simulated $Z \to \mu^+\mu^-$ events reconstructed with curl misalignment (left) and twist misalignment (right) with and without curvature corrections.

7.7 Conclusion and discussion

The standard alignment algorithms are based on minimizing the hit residuals so that residual systematic detector deformations (weak modes) can be left in the ATLAS detector geometry after alignment. The effect of the *curl* and *twist* weak modes was studied in detail. The curl weak mode moves detector elements in $\Delta\phi$ as a function of R and was observed to create a bias in q/p_T of the reconstructed tracks. The twist weak mode moves detector elements in $\Delta\phi$ as a function of z and was observed to create a bias in q/p_Z of the reconstructed tracks.

The curl and twist weak modes were studied using detector shifts where an outermost SCT barrel module can have a maximum position shift of 200 μm. For this scale of the systematic shifts, the curl misalignment was observed to result in a reconstruction bias of $(2.24\pm0.05)\cdot10^{-3}$ GeV^{-1} in q/p_T and the twist misalignment was observed to result in a reconstruction bias of $(-0.97\pm0.03)\cdot10^{-3}$ GeV^{-1} in q/p_Z.

The amount of curl or twist misalignment present in the detector can be partially measured using $J/\psi \rightarrow \mu^+\mu^-$ events and looking at the difference in the values of q/p_T and q/p_Z obtained from an unconstrained vertex fit and a mass constrained vertex fit, which gives a handle on detecting the amount of 'curl' or 'twist' misalignment present in the detector. The measured curvature bias can be used to correct reconstruction bias in q/p_T and q/p_Z, which was shown to help improve the width of the reconstructed mass in $Z \rightarrow \mu^+\mu^-$ events in the presence of a curl or twist misalignment.

When selecting $J/\psi \rightarrow \mu^+\mu^-$ events with the muon triggers available in the ATLAS experiment a continuum background of di-muon events is added to the signal. A detailed study of the effect of background on the measurement of the reconstruction bias in q/p_T and q/p_Z induced by the weak mode misalignment was beyond the scope of thesis. A first look at the effect of the presence of the di-muon continuum when determining the reconstructed biases indicates that the reconstruction bias seen in $J/\psi \rightarrow \mu^+\mu^-$ events can be distinguished from the background contribution.

The study done in this thesis used events reconstructed with a weak mode misalignments in the detector geometry, under the assumption that weak modes would not be corrected by the standard alignment algorithms. However the rigidity of the detector modules and structures plus the availability of cosmic tracks provide additional means of reducing weak modes with the standard alignment algorithms. Even if weak modes can partially be recovered by the alignment algorithms, it will be important to study the presence of a possible bias on the reconstructed track parameters by using kinematic constraints. Alignment algorithms can only find a possible minimum for the track residuals, while constraints based on physics properties provide an unbiased judgment of the alignment quality.

Appendix A

Problematic links in SCT endcap A

Table A.1: *Optical communication problems for ATLAS SCT end-cap A modules*

Module ID	link	Problem	Usable?
1A-BR-M4	RX0	slow turn-on + noisy	no, read-out through link0
1A-BR-O3	RX0	critical slow turn-on	no, read-out through link1
1A-BR-O13	RX1	slow turn-on	yes, but sensitive to threshold setting
1A-BL-O8	RX0	slow turn-on	yes, but sensitive to threshold setting
1A-BL-M5	RX1	slow turn-on	yes, but sensitive to threshold setting
1A-BL-M7	RX0	slow turn-on + noisy	no, read-out through link1
1A-TR-O13	RX1	slow turn-on	yes, but sensitive to threshold setting
1A-TR-M5	RX1	low light	yes, but sensitive to threshold setting
1A-TL-M5	RX1	low light	yes, but sensitive to threshold setting
2A-TL-O11	RX0	critical slow turn-on	no, read-out through link1
2A-TR-I1	RX1	dead VCSEL (RAL)	no, read-out through link0
2A-TR-O12	RX1	dead VCSEL	no, read-out through link0
2A-BR-M2	RX0	dead VCSEL (CERN)	no, read-out through link1
2A-BR-O9	RX0	critical slow turn-on	no, read-out through link1
3A-TR-I9	RX0	low light	yes, but sensitive to threshold setting
3A-TR-O8	RX1	critical slow turn-on	no, read-out through link0
4A-TR-O10	RX1	critical slow turn-on	no, read-out through link0
4A-TR-O12	RX 0	low light	yes, but sensitive to threshold setting

Table A.2: *Optical communication problems for ATLAS SCT end-cap A modules (continued)*

Module ID	**link**	**Problem**	**Usable?**
4A-TR-O13	RX 0	dead VCSEL	no, read-out through link1
4A-BR-O11	RX1	critical slow turn-on	no, read-out through link0
5A-TR-O8	TX	broken p-i-n-diode	no, use redundant clock from 5A-TR-O9
5A-TR-O10	RX0	dead VCSEL	no, read-out through link1
5A-TL-M6	RX1	dead VCSEL	no, read-out through link0
5A-BL-M5	RX1	dead VCSEL	no, read-out through link0
5A-BR-M4	RX1	critical slow turn-on	no, read-out through link0
5A-TL-M2	RX1	noisy	no, read-out through link0
6A-TL-M2	RX1	critical slow turn-on	no, read-out through link0
6A-TL-M6	RX0	dead VCSEL	no, read-out through link1
6A-BL-M9	RX0	dead VCSEL	no, read-out through link1
6A-BR-M1	RX1	dead VCSEL	no, read-out through link0
9A-TL-O10	RX0	dead VCSEL	no, read-out through link1
9A-TL-O11	RX1	very low light	no, read-out through link0
9A-BL-O8	RX0	dead VCSEL	no, read-out through link1
9A-BR-O11	RX1	low light	yes, but sensitive to threshold setting

Appendix B

Converting between perigee and cartesian track representation

The seven cartesian track parameters at the point of closest approach to the z-axis can be calculated in terms of the five perigee-parameters, $\vec{\eta} = (d_0, z_0, \phi_0, \theta, \frac{q}{p})$, as shown below:

$$p_x = |\frac{q}{p}| \cos\phi \sin\theta \quad \text{(B.1)}$$

$$p_y = |\frac{q}{p}| \sin\phi \sin\theta \quad \text{(B.2)}$$

$$p_z = |\frac{q}{p}| \cos\theta \quad \text{(B.3)}$$

$$E = \sqrt{(\frac{q}{p})^2 + m^2} \quad \text{(B.4)}$$

$$x = x_{\text{ref}} - d_0 \sin\phi \quad \text{(B.5)}$$

$$y = y_{\text{ref}} + d_0 \cos\phi \quad \text{(B.6)}$$

$$z = z_{\text{ref}} + z_0 \quad \text{(B.7)}$$

The 7×7 covariance matrix for the cartesian parameters can be computed by taking the differentials of the above equations, with respect to the perigee parameters. For example:

$$\begin{aligned} cov(p_x, p_x) \equiv (V_\alpha)_{11} = \; & \frac{\delta p_x}{\delta \phi_0}\frac{\delta p_x}{\delta \phi_0}(V_\eta)_{33} + 2\frac{\delta p_x}{\delta \phi_0}\frac{\delta p_x}{\delta \theta}(V_\eta)_{34} + 2\frac{\delta p_x}{\delta \phi_0}\frac{\delta p_x}{\delta \frac{q}{p}}(V_\eta)_{35} \\ & + \frac{\delta p_x}{\delta \theta}\frac{\delta p_x}{\delta \theta}(V_\eta)_{44} + 2\frac{\delta p_x}{\delta \theta}\frac{\delta p_x}{\delta \frac{q}{p}}(V_\eta)_{45} + \frac{\delta p_x}{\delta \frac{q}{p}}\frac{\delta p_x}{\delta \frac{q}{p}}(V_\eta)_{55} \end{aligned} \quad \text{(B.8)}$$

This follows from the definition $cov(p_x, p_x) = \langle \delta p_x \delta p_x \rangle$. The set of differentials can be represented by the *Jacobian matrix*, **J**:

$$\mathbf{J} = \begin{pmatrix} \frac{\partial H_1(\vec{\alpha}_A)}{\partial \alpha_1} & \cdots & \frac{\partial H_1(\vec{\alpha}_A)}{\partial \alpha_n} \\ \frac{\partial H_2(\vec{\alpha}_A)}{\partial \alpha_1} & \cdots & \frac{\partial H_2(\vec{\alpha}_A)}{\partial \alpha_n} \\ \vdots & \ddots & \vdots \\ \frac{\partial H_r(\vec{\alpha}_A)}{\partial \alpha_1} & \cdots & \frac{\partial H_r(\vec{\alpha}_A)}{\partial \alpha_n} \end{pmatrix} \tag{B.9}$$

The Jacobian matrix can then be used to transform the covariance matrix in the perigee frame to the covariance matrix in cartesian frame:

$$V_\alpha = \mathbf{J}_{\eta\to\alpha} V_\eta \mathbf{J}_{\eta\to\alpha}{}^{-1} \tag{B.10}$$

The transformation-matrix $\mathbf{J}_{\eta\to\alpha}$, for transformation from the perigee to the cartesian representation, can be calculated to be equal to:

$$\mathbf{J}_{\eta\to\alpha} = \begin{pmatrix} 0. & 0. & -p_y & p_z\cos\phi & \frac{-qp_x}{|\frac{q}{p}|} \\ 0. & 0. & p_x & p_z\sin\phi & \frac{-qp_y}{|\frac{q}{p}|} \\ 0. & 0. & 0. & \frac{-\sin\theta}{|\frac{q}{p}|} & \frac{-qp_z}{|\frac{q}{p}|} \\ 0. & 0. & 0. & 0. & \frac{-q}{E\cdot|\frac{q}{p}|^3} \\ -\sin\phi & -d_0\cos\phi & 0. & 0. & 0. \\ \cos\phi & -d0*\sin\phi & 0. & 0. & 0. \\ 0. & 1. & 0. & 0. & 0. \end{pmatrix} \tag{B.11}$$

Similarly the transformation-matrix $\mathbf{J}_{\alpha\to\eta}$, for transformation from the cartesian to the perigee representation, can be calculated to be equal to:

$$\mathbf{J}_{\alpha\to\eta} = \begin{pmatrix} 0. & 0. & 0. & 0. & -\sin\phi & \cos\phi & 0. \\ 0. & 0. & 0. & 0. & 0. & 0. & 1. \\ -\frac{py}{p_x^2+p_y^2} & \frac{px}{p_x^2+p_y^2} & 0. & 0. & 0. & 0. & 0. \\ \frac{\cos\phi}{p_z(1+\tan\theta^2)} & \frac{\sin\phi}{p_z(1+\tan\theta^2)} & \frac{-\tan\theta}{p_z(1+\tan\theta^2)} & 0. & 0. & 0. & 0. \\ -\frac{q\cdot E}{p^3} & 0. & 0. & 0. & 0. & 0. & 0. \end{pmatrix} \tag{B.12}$$

It should be noted that the cartesian represenation is used to represent the trajectory at a specific point along the track. This can be any point the track while the perigee parameters are by definition defined at the point of closest approach to the global z-axis. This means that before $J_{\alpha\to\eta}$ is used to obtain the perigee representation, the cartesian coordinates and their corresponding error-matrix should be transported to the perigee position.

Bibliography

[1] LEP Electroweak Group for Higgs boson searches, *Search for the standard model Higgs Boson at LEP*, Phys. Rev. D **72** (2005) .

[2] J.J. Aubert et al., *Experimental Observation of a Heavy Particle J*, Phys. Rev. Lett **33**(23) (1974) 1404.

[3] J.E. Augustin et al., *Discovery of a Narrow Resonance in e^+e^- Annihilation*, Phys. Rev. Lett **33**(23) (1974) 1406.

[4] C. Amsler et al., *Review of Particle Physics*, Phys. Lett. B **667** (2008) .

[5] T. Sjöstrand et al., *High-Energy-Physics Event Generation with Pythia 6.1*, Comput. Phys. Comm. **238** (2001) .

[6] B. Andersson, G. Gustafson, G. Ingelman and T. Sjöstrand, *Parton fragmentation and string dynamics*, Physics Reports **97** (1983) 31.

[7] F. Halzen and A.D. Martin, *Quarks and leptons: An introductory course in modern particle physics*, John Wiley & Sons Inc, 1984.

[8] W.E. Caswell and G.P. Lepage, *Effective lagrangians for bound state problems in QED, QCD, and other field theories*, Phys. Rev. B **167** (1986) 437.

[9] M. Krämer, *Quarkonium Production at High-Energy Colliders*, Prog. Part. Nucl. Phys. **47** (2001) 141.

[10] E.L. Berger and D. Jones, *Inelastic photoproduction of J/ψ and Υ by gluons*, Phys. Rev. D **23** (1981) 1520.

[11] F. Abe et al., *Inclusive J/ψ, $\psi(2S)$ and b-quark production in p anti-p collisions at $\sqrt{s}$ = 1.8 TeV*, Phys. Rev. Lett. **69** (1992) .

[12] E. Braaten, G.T. Bodwin, and G.P. Lepage, *Rigorous QCD Analysis of Inclusive Annihilation and Production of Heavy Quarkonium*, Phys. Rev. D **51** (1995) 1125.

[13] H.L. Lai et al., *Global QCD Analysis of Parton Structure of the Nucleaon: CTEQ5 Parton Distributions*, Eur. Phys. Journal C **12** (2000) 375.

[14] P. Nason et al., *Bottom Production*, Report of the 1999 CERN Workshop on SM physics (and more) at the LHC. (2000) .

[15] The ATLAS collaboration, *Expected Performance of the ATLAS Experiment, Detector, Trigger and Physics*, CERN public note, CERN-OPEN-2008-020.

[16] G. Aad et al., *The ATLAS Experiment at the CERN Large Hadron Colllider*, JINST **3** (2008) , S08003.

[17] S.D. Drell and T.M. Yan, *Massive Lepton-Pair Production in Hadron-Hadron Collisions at High Energies*, Phys. Rev. Lett. **25** (1970) 316.

[18] The LHC Study Group, *The Large Hadron Collider Conceptual Design*, CERN-AC/95-05, 1995.

[19] CERN Director General, *Summary of the analysis of the 19 September 2008 incident at LHC*, CERN Preprint 1135729, 2008.

[20] S. Hassani et al., *A muon identification and combined reconstruction procedure for the atlas detector at the lhc using the (muonboy, staco, mutag) reconstruction packages*, Nucl. Instrum. Meth. **A572** (2007) .

[21] A. Abdesselam et al., *The ATLAS SemiConductor tracker end-cap module*, Nucl. Instrum. Meth. **A575** (2007) 353.

[22] A. Abdesselam et al., *The barrel modules of the ATLAS semiconductor tracker*, Nucl. Instrum. Meth. **A568** (2006) 642.

[23] G. Ambrosi et al., *Proceedings of the 15th International Workshop on Vertex Detectors, Perugia, Italy*, Nucl. Instrum. Meth. **A582** (2007) 701.

[24] ATLAS collaboration, *ATLAS Inner Detector Technical Design Report*, CERN-LHCC/97-16, 1997.

[25] V. Highland, *Some practical remarks on multiple scattering*, Nucl. Instrum. Meth. **125** (1975) 497.

[26] D.J. White et al., *Radiation hardness studies of the front end ASICs for the optical links of the ATLAS SemiConductor Tracker*, Nucl. Instrum. Meth. **A457** (2001) 369.

[27] International Commission of Radiation Units, *Stopping powers and ranges for protons and alpha particles*, ICRU Report **No. 49** (1993) .

[28] M. Marucho, H. Fanchiotti, and C. Garcia Canal, *The Landau distribution*, Int. J. Mod. Phys. **C17** (2006) 1461.

[29] S. Sze, *Semiconductor Devices*, John Wiley & Sons, 1985.

[30] A. Ahmad et al., *The silicon microstrip sensors of the ATLAS semiconductor tracker*, Nucl. Instrum. Meth. **A578** (2007) 99.

[31] M. Vos, *The ATLAS inner tracker and the detection of light Super-Symmetric Higgs bosons*, Phd thesis, University of Twente, 2003.

[32] M. Moll, *Radiation Damage in Silicon Particle Detectors*, Phd thesis, University of Hamburg, 1999.

[33] C. Lacasta et. al., *Electrical Results from Prototype Modules*, ATLAS public note, ATL-IS-TN-0002, 2002.

[34] Z.Li, E. Verbiskaya C.J.Li, and V. Eremin, *Temperature stimulated abnormal annealing of neutron induced damage in high resistivitiy silicon detectors*, Nucl. Instrum. Meth. **A385** (1997) 321.

[35] F. Campabadal et al., *Design and performance of the ABCD3TA ASIC for readout of silicon strip detectors in the ATLAS semiconductor tracker*, Nucl. Instrum. Meth. **A552** (2005) 292.

[36] A. Abdesselam et al., *Engineering for the ATLAS SemiConductor Tracker (SCT) End-cap*, JINST **3** (2008) , P05002.

[37] P. Ford, *SCT End-cap Thermal Enclosures*, ATLAS public note, ATL-IS-EA-0006, 2004.

[38] D. Atree et al., *The evaporative cooling system for the ATLAS Inner Detector*, JINST **3** (2008) , P07003.

[39] E. v.d. Kraaij, *First Top Quark Physics with ATLAS - A Prospect*, Nikhef PhD thesis, 2009.

[40] A. Abdesselam et al., *The optical links of the ATLAS SemiConductor Tracker*, JINST 2 **P09003** (2007) .

[41] G. Mahout et al., *Irradiation studies of multimode optical fibres for us in ATLAS front-end links*, Nucl. Instrum. Meth. **A446** (2000) 426.

[42] A. Yariv, *Optical Electronics in Modern Communications*, Oxford Univerisity Press (OUP), 1997, Oxford Series in Electrical and Computing Engineering.

[43] H. Spieler, *Semiconductor Detector Systems*, Oxford Univerisity Press (OUP), 2005.

[44] J.D. Dowell et al., *Single event upset studies with the optical links of the ATLAS SemiConductor Tracker*, Nucl. Instrum. Meth. **A481** (2002) 575.

[45] M.L. Chu et al., *The off-detector opto-electronics for the optical links of the ATLAS Semiconductor Tracker and Pixel detector*, Nucl. Instrum. Meth. **A530** (2004) 293.

[46] D.G. Charlton et. al., *Radiation hardness and lifetime studies of photodiodes for the Optical Readout of the ATLAS SCT*, Nucl. Instrum. Meth. **A456** (2001) 300.

[47] A. Abdesselam et al., *The data acquisition and calibration system for the ATLAS Semiconductor Tracker*, JINST **3** (2008) , P01003.

[48] E. Koffeman, *A luminosity measurement at LEP using the L3 detector*, Phd thesis, Katholieke Universiteit Nijmegen, 1996.

[49] C. Magrath, *The Heart of ATLAS - Commissioning and Performance of the ATLAS Silicon Tracker*, Nikhef PhD thesis, 2009.

[50] S. Peeters, *The ATLAS SemiConductor Tracker Endcap*, Phd thesis, University of Amsterdam, 2003.

[51] G. Duckeck et. al., *ATLAS computing: Technical Design Report*, CERN public note, CERN-LHCC-2005-022.

[52] GEANT4 Collaboration, S. Agostinelli et al., *Geant4: A simulation toolkit*, Nucl. Instrum. Meth. **A506** (2003) .

[53] A. Salzburger et al., *The new ATLAS Track Reconstruction (NEWT)*, ATLAS public note, ATL-SOFT-PUB-2007-007, 2007.

[54] R. Clifft and A. Poppleton, *Ipatrec: inner detector pattern-recognition and track-fitting*, ATLAS public note, ATL-SOFT-94-009, 1994.

[55] I. Gavrilenko, *Description of Global Pattern Recognition Program (XKALMAN)*, ATLAS public note, ATL-INDET-97-165, 1997.

[56] R. Frühwirth et al., *Application of Kalman Filtering to Track and Vertex Fitting*, Nucl. Instrum. Meth. **A262** (1987) 444.

[57] S. Todorova, A. Salzburger, and M. Wolter, *The ATLAS Tracking Geometry Description*, ATLAS public note, ATL-SOFT-PUB-2007-004, 2007.

[58] E. Lund, L. Bugge, I. Gavrilenko, and A. Strandlie, *Track parameter propagation through the application of a new adaptive Runge-Kutta-Nystrom method in the ATLAS experiment*, ATLAS public note, ATL-SOFT-PUB-2009-001, 2009.

[59] P. Avery, *Fitting Theory I: General Least Squares Fitting Theory*, CBX 91-72, 1991.

[60] T.G. Cornelissen et al., *The global χ^2 track fitter in ATLAS*, J. Phys. Conf. Ser. 119 (2007) , proceedings CHEP 2007.

[61] E. Bouhova-Thacker et al., *Vertex Reconstruction in the ATLAS Experiment at the LHC*, ATLAS public note, ATL-INDET-PROC-2008-003, 2008.

[62] P. Billoir and S. Quian, *Fast vertex fitting with a local parametrization of tracks*, Nucl. Instrum. Meth. **A319** (1992) 139.

[63] M. Limper, *A new tool for constrained vertex fitting in ATLAS*, Proceedings for ACAT 2008 , ATLAS public note, ATL-INDET-PROC-2009-003.

[64] P. Avery, *Applied Fitting Theory VI: Formulas for Kinematic Fitting*, CBX 98-37, 1999(rev.).

[65] T. Golling, *Alignment strategy for the ATLAS tracker*, Proceedings of the 16th International Workshop on Vertex Detectors (2007) .

[66] S. Gibson et al, *ATLAS SCT End-cap Alignment System Layout*, ATLAS public note, ATL-IS-ES-0081, 2005.

[67] A. Hicheur, P. Bruckman, and S. Haywood, *Global χ^2 approach to the Alignment of the ATLAS Silicon Tracking Detectors*, ATLAS public note, ATL-INDET-PUB-2005-002, 2005.

[68] J. Alison, *Alignment of the ATLAS Inner Detector Tracking System*, ATLAS public note, ATL-INDET-PROC-2009-004, 2009.

[69] J. Alison, B.D. Cooper, and T. Goettfert, *Production of Residual Systematically Misaligned Geometries for the ATLAS Inner Detector*, ATLAS internal note, ATL-COM-INDET-2009-003, 2009.

Summary

The Standard Model of particle physics has had great success in describing the different types of elementary particles and their interactions. The only particle predicted by the Standard Model that has not yet been observed in a particle physics experiment is the Higgs boson. If the Higgs boson is not discovered within a mass range of 114.4-185 GeV, electroweak symmetry breaking within the Standard Model can not be explained.

Identifying the mechanism of electroweak symmetry breaking will be one of the main goals of the Large Hadron Collider. The LHC is designed to create proton-proton collisions with an unprecedented luminosity of $10^{34}\text{cm}^{-2}\text{s}^{-1}$ and a center of mass energy of 14 TeV, which will allow the discovery of new particles with masses up to the TeV scale. ATLAS is one of four experiments built to study the proton-proton collisions of the LHC and was designed to exploit the full physics potential of the LHC.

This thesis focuses on two main subjects: the construction and commissioning of the ATLAS silicon strip detector and the measurement of $J/\psi \rightarrow \mu^+\mu^-$ events in ATLAS, focusing on the use of these events to correct certain types of misalignment in the detector. At the time of writing this thesis, no LHC proton collisions had yet taken place, so a simulation of the events as they would be measured in ATLAS was used.

One of the sub-detectors of the ATLAS inner detector is the SCT, a silicon strip detector with an intrinsic resolution of 23 μm per strip hit. One of the SCT end-caps was constructed and tested at Nikhef in Amsterdam. The SCT end-cap holds 988 detector modules that are each composed of two layers of silicon strips placed under a small stereo-angle. The on-detector electronics provide the read-out, amplification and discrimination of the signals of the 1536 strips on each module. The SCT uses a binary read-out system which only record a hit-or-no-hit signal on each strip. The binary output is stored in a digital pipeline in the on-detector electronics while awaiting the trigger decision.

The SCT uses an optical read-out system that sends and receives signal from an to the detector modules. Vertical Cavity Surface Emitting Lasers (VCSELs) are used to transform the electronic signal to an optical signal, while p-intrinsic-n diodes are used to receive the optical signal and convert it to an electric signal. Extensive tests of the optical read-out system demonstrated

that all modules can receive and send data. A total of 34 SCT modules have to rely on their redundancy options in order to ensure correct read-out of the module over time. This is mostly due to problems in the optical lines returning data from the modules.

The SCT module performance was tested during all assembly stages of the SCT end-cap including the commissioning of the detector in its final position within the ATLAS experiment. Tests of the front-end read-out electronics showed that 99.7% of all silicon strips can be correctly read-out which is well within the required 99% efficiency for the detector. The measurement of the input noise during several test stages shows that the input noise on the modules did not change between the test stages, indicating that no common mode noise was added to the system during assembly.

The first data from LHC collisions allows the calibration of the detector using benchmark physics channel such as $J/\psi \rightarrow \mu^+\mu^-$. This thesis studied how $J/\psi \rightarrow \mu^+\mu^-$ events measured in ATLAS might be used to correct some of the effects weak mode misalignments in the detector when using a mass constrained vertex fit. Non-perturbative QCD models predict that the cross-section for prompt J/ψ production when requiring one muon with $p_T > 6$ GeV and a second muon with with $p_T > 4$ GeV and $|\eta| < 2.5$ for both muons is approximately 23 nb.

Measurements of the position of passage of charged particles in the ATLAS inner detector are used to reconstruct precise particle trajectories. Reconstructing the intersection point of a set of trajectories helps to identify the decay vertex of particles produced in the LHC collisions. A tool for kinematically constraining a vertex fit in ATLAS was developed. This tool is based on minimization of the χ^2 with Lagrange multipliers. In a sample of simulated $b\bar{b} \rightarrow X + (J/\psi \rightarrow \mu^+\mu^-)$ events the addition of a mass constraint to the vertex fit was shown to improve the resolution of q/p_T of the muon track by 20-25% over the whole momentum range.

To fully profit from the performance of the ATLAS inner detector, the possible knowledge of the position of the detector elements is essential. One of the main alignment strategies in ATLAS is based on minimizing the hit residuals of a large set of reconstructed tracks. Residual systematic detector deformations (weak modes) that minimize the hit residuals without representing the true detector geometry, can be present in the ATLAS detector geometry after alignment. The presence of weak modes in the detector geometry can lead to a bias on the reconstructed track parameters, so eliminating weak modes is of vital importance for achieving the full physics potential of ATLAS. For misalignments where an outermost SCT barrel module has a maximum position shift of 200 μm, shifts in the detector position in $\Delta\phi$ as function of R give a reconstruction bias of $(2.24\pm0.05)\cdot10^{-3}$ GeV^{-1} in q/p_T, and shifts in the detector position in $\Delta\phi$ as function of Z give a reconstruction bias of $(-0.97\pm0.03)\cdot10^{-3}$ GeV^{-1} in q/p_Z. The level of deformation present in the detector can be partially measured using $J/\psi \rightarrow \mu^+\mu^-$ events and looking at the difference in the values of q/p_T and q/p_Z obtained from an unconstrained vertex fit and a mass constrained vertex fit.

Samenvatting

Dit proefschrift beschrijft twee onderwerpen: de constructie en het testen van de ATLAS silicium strip detector en de meting van $J/\psi \rightarrow \mu^+\mu^-$ gebeurtenissen in de ATLAS detector met als het doel het bepalen van de exacte locatie van de detector-elementen. Tijdens het schrijven van dit proefschrift hadden nog geen proton-proton botsingen plaats gevonden in de 'Large Hadron Collider' (LHC), dus is gebruik gemaakt van een simulatie van gebeurtenissen in het ATLAS experiment.

Eén van de types detectoren in ATLAS is de 'SemiConductor Tracker' (SCT), een silicium strip detector met een intrinsieke resolutie van 23 μm per strip. Eén van de voorwaartse SCT detectoren was gebouwd en getest op het Nikhef instituut te Amsterdam. De voorwaartse SCT detector bevat 988 detector modules die elk bestaan uit twee lagen met silicium strips geplaatst onder een stereo-hoek van 40 mrad. De elektronica op de SCT modules zorgt voor de versterking, discriminatie en uitlezing van de signalen van de 1536 strips op elke module. De SCT maakt gebruik van een binair uitlees systeem dewelke alleen registeert of het signaal boven of onder een gegeven drempelwaarde was. De binaire signalen worden opgeslagen in een digitale geheugen op de SCT modules, totdat het ATLAS trigger-systeem kan bepalen of gemeten signalen wel of niet interressant zijn om te bewaren.

De SCT maakt gebruik van een optisch uitlees systeem dat signalen van en naar de detector modules stuurt. 'Vertical Cavity Surface Emitting Lasers' (VCSELs) worden gebruikt om de elektronische signalen in licht om te zetten, en 'p-intrinsic-n' diodes worden gebruikt om de optische signalen te converteren naar een electronisch signaal. Tests van het optische uitlees systeem hebben gedemonstreerd dat alle SCT modules commando's kunnen ontvangen en data kunnen terugsturen en naar het centraal data-acquisitie systeem. In totaal zijn er 34 SCT modules die gebruik moeten maken van hun redundantie mogelijkheden om correcte communicatie met de module te bewerkstelligen.

De prestaties van de SCT modules zijn getest gedurende de verschillende constructie fases van de voorwaartse SCT detector. De tests van de elektronica op de detector modules laten zien dat 99.7% van alle silicium strips correct uitgelezen kunnen worden. Dit resultaat is ruimschoots beter dan de vereiste 99% efficiëntie van de detector. De metingen van de ruis op de strips gedurende de verschillende constructie fases hebben laten zien dat geen 'common mode'-

ruis is toegevoegd in het systeem tijdens de constructie.

De eerste data van de LHC botsingen maken het mogelijk om de detector te kalibreren met een referentie kanaal zoals $J/\psi \rightarrow \mu^+\mu^-$. Dit proefschrift beschrijft hoe $J/\psi \rightarrow \mu^+\mu^-$ gebeurtenissen zoals gemeten in ATLAS gebruikt kunnen worden voor het corrigeren van de effecten van 'weak mode misalignments'. Niet-pertubatieve QCD modellen voorspellen dat voor proton-proton interacties met $\sqrt{s}$=14 TeV de werkzame doorsnede voor de directe productie van J/ψ's ongeveer 23 nb is, wanneer vereist wordt dat de gebeurtenissen tenminste *één* muon met $p_T > 6$ GeV en een tweede muon met $p_T > 4$ GeV met bevatten en beide muonen zich binnen het detectorbereik van $|\eta| < 2.5$ bevinden.

Metingen van de posities van geladen deeltjes gemaakt in de ATLAS detectoren worden gebruikt om de banen van de deeltjes te reconstrueren. Vertex fit algortimes kunnen de vervals positie van deeltje bepalen aan de hand van de intersectie van de banen van de vervalsproducten. Voor dit proefschrift is een software-algoritme ontwikkelt dat een vertex fit uitvoert met de toevoeging van kinematische randvoorwaardes behorende bij specifieke deeltjes vervallen. In gesimuleerde ATLAS data van $b\bar{b} \rightarrow X + (J/\psi \rightarrow \mu^+\mu^-)$ gebeurtenissen kan dit algoritme de resolutie op q/p_T van de muon banen verbeteren met 20-25%, door te vereisen dat de invariante massa van de muonen gelijk moet zijn aan de J/ψ massa.

Om volledig gebruik te maken van de intrinsieke resolutie van de ATLAS detector moet de positie van de verschillende detector elementen zo precies mogelijk bepaald worden. Een strategie om dit te bereiken is het minimali-zeren van de hit residuals van een grote hoeveelheid gereconstrueerde deeltjes banen. Er bestaan echter deformaties van de detector geometrie waarbij de hit residuals geminimalizeerd worden, zonder dat de daadwerkelijke detector geometrie wordt bereikt. De aanwezigheid van deze zogenaamde 'weak mode misalignments' kan leiden tot een verkeerde reconstructie van de baan parameters en moet daarom voorkomen worden. Een detector deformatie waarbij detector posities verschoven worden in $\Delta\phi$ als functie van R, overeenkomend met een maximum verschuiving van 200 μm in positie van een SCT module, geeft een bias op q/p_T van de gereconstrueerde baan van $(2.24\pm0.05)\cdot10^{-3}$ GeV^{-1}. Een vergelijkbare detector deformatie waarbij detector posities verschoven worden in $\Delta\phi$ als functie van de Z-coordinaat, geeft een bias op q/p_Z van de gereconstrueerde baan van $(-0.97\pm0.03)\cdot10^{-3}$ GeV^{-1}. De deformatie van de detector geometrie kan gedeeltelijk gemeten en gecorrigeerd worden wanneer gebruik gemaakt wordt van $J/\psi \rightarrow \mu^+\mu^-$ gebeurtenissen en het verschil gemeten wordt tussen de waarde van q/p_T en q/p_Z verkregen met een vertex fit -zonder- en -met- een kinematische randvoorwaarde voor de invariante massa.

Acknowledgements

Thanks Stan for coming up with a new thesis-topic whenever our expectation for data had to be adjusted! I don't mean this in a negative way, Stan's enthusiasm seems immune to LHC delays and I learned a lot of different physics topics before arriving at the inevitable conclusion that this thesis would contain no data. Inspired by Stan, my enthusiasm has become unstoppable as well, I will continue in ATLAS hoping one day to see what "real data" looks like!

Some of the best time of my PhD was spent building the Nikhef SCT end-cap, ATLAS is a big experiment, but in the relatively small SCT-group at Nikhef we had our own little project to focus on. All my SCT-buddies were great to work with, but Auke was also my supervisor and always tried to make everything fun! For example: at his suggestion we handed out stroopwafels after my talk on the SCT at CERN, and we certainly cheered up everyone in the meeting as well!

Writing the thesis was difficult for me, Stan and Auke managed to pull me through, but they couldn't have done it without my "third supervisor": Wolfgang. Thank you so much for all the help you gave me both for my software work and the correction of my thesis!

Before starting my PhD, I visited silicon-alley in Nikhef and saw a girl dressed in a lab-coat working on very complicated looking hi-tech stuff. "That could be me!" I thought as I was just asked which of the sub-detector groups at Nikhef I would like to join. So Caroline, you inspired my choice for the Nikhef SCT-group and I had a great time working with you! SCT-chicks forever!

Of course before I even started my PhD, when I was still a naive young woman aspiring to become a crazy scientist, I was studying physics at the UvA. Jan Amoraal showed our little group of first-year rookies around, making sure that no pub was missed! Jan joined me in doing a PhD at Nikhef so we could continue drinking beers and playing play-station together! Zdenko was yet another friend both during my studies at the UvA and our PhD at Nikhef. Together we did our first-year project at Nikhef, where we met Stan and both got tricked into doing our PhD with him!

Outside (and sometimes during) my classes at the UvA I could usually be found in 'de kelder' where I enjoyed time with the WEIS-people: Hippie, Giel, Paal, Dewi, Sarah, Ella, Sjaak, Knoedel, Vlabaard, Arnie, Kaatje, Jap, Jimmy, Peter, Karim, Worst, Ullie, Frank1, Frank4 enzovoorts! There were three people especially I kept in touch with after my studies: Dwerg, de Lompe Mo en Maurits, aka het dappere dis-gezelschap! Dankzij ons is Turmish eindelijk gered van de Zwarte Macht!

There's a lot of people that I had the pleasure of meeting and spending time with during the last 4 1/2 years. As soon as my PhD began I moved with Claudine and Antonello into a wonderful house in Amsterdam. This house became a basis for many social events, especially the epic halloween parties! We often shared the house and many dinners with our friends Hernan, Angelo, Giampiero, Cosimo, Marianne and Jacopo!

At this moment I'd like to dedicate a paragraph to coffee-breaks at Nikhef... Procrastination at its best! Bad jokes and bad coffee were enough to make anyone forget about LHC-delays... Nikhef buddies, you know who you are!

I moved up and down between Geneva and Amsterdam a few times, enough to finally want to settle in the Geneva area. Here at CERN I found in Carol a most wonderful friend, and together with Nicola, Wolfgang, Shirit, Nigel, Eduard, Alessandro, Barbara, Samuele, Nicola S. and Alessandra I spent great times in/around CERN and hope to spend many more nice years!

Voor mijn ouders: de laatste maanden van promotie was ik weer thuis bij jullie in Eemnes en dit heeft mij enorm geholpen om het proefschrift af te krijgen, bedankt voor dit en alle steun die jullie mij altijd hebben gegeven tijdens mijn studie! Dorine, natuurkunde studeren heeft mij niet slimmer gemaakt dan de tijd die ik met jou heb doorgebracht, je bent een fantastische zus en mijn beste vriendin.

Jacopo, mio marito, so much has happened since starting my PhD and meeting you. Together we continue our journey of life, love and the pursuit of happiness!